

Analytical Chemistry Investigations Toward Understanding
the Mechanism of Nitrogenase from *Azotobacter vinelandii*
and the Role of the 4Fe-4S Cluster of Dna2 from
Saccharomyces cerevisiae

Thesis by
Siobhán Gaustad MacArdle

In Partial Fulfillment of the Requirements for the
Degree of
Doctor of Philosophy

CALIFORNIA INSTITUTE OF TECHNOLOGY
Pasadena, California

2022
Defended May 12th 2022

© 2022

Siobhán Gaustad MacArdle
ORCID: [0000-0001-7843-5977]

All rights reserved

ACKNOWLEDGEMENTS

By far the greatest value of my graduate school experience has come from the people that I've been lucky to work with and become friends with. I feel overwhelming gratitude for the people in my life that love and support me regardless of my scientific achievements.

First, I would like to thank the Barnard Chemistry Department for sparking my love of chemistry, which has only grown since my first chemistry class taught by Prof. Sally Chapman in my freshman year. Especially, I would like to thank Professor Marisa Buzzeo for supporting my thesis research at Barnard and continuing to support me after I graduated, even when it meant making long distance calls to Dublin. If it weren't for Professor Buzzeo, I would not have applied to Caltech and I am immensely grateful for her encouragement.

At Caltech, I would like to thank my advisor, Professor Doug Rees, for giving me a second chance at graduate school and being an invaluable support in my hardest moments toward my degree. I am so grateful for the opportunity to join your group and work on this project. Through this project, I discovered my interests in analytical chemistry and designing enzymatic activity assays, which I hope to continue in my future career. Thank you for supporting and guiding me scientifically and also for fostering a community in your lab where all identities are welcome and celebrated.

Thank you to all the members of the Rees group: Trixia Buscagan, Jeff Lai, Ailiena Maggiolo, Stephanie Threatt, and Beccah Warmack. I could not have asked for better lab mates! Thank you so much for always answering my questions, teaching me how to work with nitrogenase, and for being my friend. Thank you Trixia for teaching me how to do activity assays, always giving me helpful feedback, and for all of our coffee chats. Thank you Beccah for doing one of my first preps with me, teaching me how to use the fermentor, and for your DEI commitments that have made such a great addition to my graduate school experience. Thank you so much Ailiena for giving me the opportunity to work on your project with you and for making delicious cocktails! Thank you Stephanie for being such a great lab mate in both of my labs at Caltech; your calm and grounded presence has always made me feel comfortable. And thank you Jeff for being so generous with your time, being such a great problem solver which has allowed us to focus on our research.

I feel incredible grateful for the opportunity to meet and spend time with Professor Jim Howard. When I first joined the Rees group, he took the time to take me to coffee and talk to me about science and life, telling me about his adventures biking around Europe

and our shared past experiences living in Berkeley. As a new member of the group, this was very influential in making me feel welcome and seen. He continued to support me throughout my time in the Rees group, always sending thorough emails after my group meetings that were supportive and contained great insight and ideas for future work. His enthusiasm in my work made me feel important at a time when I was questioning whether I would produce any real results in graduate school. Jim's emails and presence brought me so much joy; thank you Jim. I will try to engage with other scientists the way you engaged with me, seeing me as a whole person and making me feel special and valued.

My project in the Rees group could not have been achieved without many instruments in shared-user facilities around Caltech and I am so grateful for the scientists in those facilities for their time and support in helping me accomplish my experiments. I would like to thank Dr. Nathan Dalleska for teaching me how to use the GC-MS and for spending countless hours trying to optimize the instrument for quantification of hydrogen isotopologues. Thank you Nathan for answering my many emails and slack messages, teaching me how to troubleshoot when instruments aren't working as they should, and for teaching me how to be rigorous when collecting and analyzing data. My favorite thing about research has been learning how to use new instruments and without your support I wouldn't have discovered my love of analytical chemistry. Thank you David Vander Velde for teaching me how to use the NMR Spectrometer, helping me optimize the instrument for my experiments, and teaching me how to process and analyze the spectra. Thank you Jay Winkler for not only teaching me how to do FTIR Spectroscopy, but also for your support when I was switching labs. Thank you Sam Xiong for helping me with the quantitative ethylene transfer!

Thank you to my thesis committee, Harry Gray, Judy Campbell, and Theo Agapie, for your guidance and insight on my research throughout my time at Caltech. Harry, I would not have finished my PhD if it wasn't for you. I was panicking about what to do at the end of my fourth year and you helped me focus on the science, which turned an emotionally painful experience into an interesting scientific investigation. Being able to separate the data and experimental results from my emotional well-being has been a challenge during graduate school and your positive demeanor and scientific curiosity helped me toward this growth. Judy, thank you for teaching me so much about the fascinating enzyme Dna2 and for supporting me even when I had to transition away from working on the enzyme. Theo, when I had results from my solvent isotope effect experiments, but felt lost on how to interpret them, meeting with you was extremely helpful. Thank you for your investment in my research and for taking the time to offer thoughtful questions and suggestions. Thank you Jackie Barton for sharing the wonder of 4Fe-4S cluster proteins with me, for teaching

me how to be a professional scientist, and for inspiring me to be myself in academia.

Thank you to Bil Clemons and the members of the Clemons group for your kindness, curiosity, and fun times! I was so excited when I found out we were merging groups with you and it's been lovely getting to know you all. Looking forward to more fun and science with you in the future!

Switching labs at the end of my fourth year was a great challenge and I was very close to leaving graduate school altogether. A few members of the Barton group were my rocks during this time, keeping me tethered and helping me through the experience day by day. Dr. Rebekah Silva, you were my first mentor in graduate school and you taught me everything I know about cloning, protein expression, and enzyme handling. You taught me how to be a graduate student. You are so intelligent and kind and I loved how you would always say that every protein is its own "special snowflake." Dr. Nirit Kantor-Uriel, I feel so lucky to have been able to meet you and your family. You are such a strong woman and a talented chemist and I admire you so much. Thank you both for being so generous with your time when I was switching labs, getting coffee with me to help me figure out my options. Dr. Levi Ekanger, I am so grateful for your kindness and insight and I will never forget our conversations. Bekah, Nirit, and Levi, without you I would not have had the strength to switch labs, which was one of the most influential decisions of my life thus far, and I'm so glad that I did. Thank you! Thank you Elizabeth Garcia for being so caring during my time in the Barton group; I could talk to you about anything and I am grateful for all of your insight about mental health and self care.

When I was going to leave graduate school at the end of my fourth year, I felt like I should feel upset that the last four years of my life had been "wasted". But I didn't feel that way, solely because of all the beautiful friends that I've made here. During that time, I realized that my friends wouldn't care if I had a PhD or not and an overwhelming feeling of gratitude came over me. For my Caltech friends: although I've met all of you in the context of graduate school, I feel like my connection with you and our friendship is on a level much deeper than our work or studies. I feel so grateful to have been able to find friends that appreciate and inspire me! I have had so much fun in graduate school, laughed so much, ate so much, played so much, and I am wholly indebted to my friends for these experiences.

Thank you Peter Mezey for being my best friend, being my companion in NYC, being a great listener, and always sending me the slaps. Thank you Elise Tookmanian for being such a close and important friend for me throughout graduate school; although we shared many of the same activities (chemistry, RAing, soccer) I feel like our connection has little

to do with what we do and is a deeper function of who we are. Izzy Langone, having you in LA was so important to my sanity and well-being during graduate school; thank you so much for being my friend and for being so easy to talk to and spend time with. Thank you Dominique Haskell for letting me play with you at recess in 6th grade, the start of our beautiful and invaluable friendship; I am so grateful to have you to turn to when I'm going through it or want to have a good time. Thank you Namita Sarraf for making friendship familial; you are a powerful force of community and everyone in your orbit benefits from the work you do to bring people together. Samuel Bostick, thank you for being enthusiastic and cheering me on in all my pursuits; I am so grateful for all of our conversations about fermentation and the trigonometry of life. Thank you Alex Tudor for being my friend when I was new to Dublin, for showing me around Romania (I still think about langós and the salt mine all the time), and for our many conversations throughout my time here. Thank you Thom Bohdanowicz, Kat Rinaldi, Sam Williams, William Poole, Aabha Morey, Stefan Turkowski, Peishi Cheng, Luke Metzler, Lori Dajose, Vatsal Jhalani, Micki Hanewich-Hollatz, Malaney Young, Laney Camenga, Yingxin Deng, Rachel Banks, Liz O'Brien, Fiona Brodie, Tai Vogel, Amber Haskell, Marina Hunt. Thank you to my friends at the Hermsillo, Sam, Scotty, John Paul, and Devon, for making me feel like a part of a community in LA!

I am so lucky to have the best family that there is. Thank you mom and dad for making my life so easy and fun. Thank you for being proud of me and for getting excited about the things that I get excited about. Maria, I am literally the luckiest person in the world to get to be your sister. I love the way you see the world, I look up to the values with which you live your life, and I admire the care and kindness you take with everyone that you encounter. Anthony, thank you for inspiring me to pursue science. When I was a kid (and still now) I wanted to be just like you; your curiosity about phenomena in our universe is contagious and made me want to be a scientist from an early age. Thank you! Gó raibh míle maith agat!

ABSTRACT

Iron sulfur clusters are ubiquitous metal cofactors that play a variety of roles in many enzymes important for health and the climate. The bacterial nitrogenase enzyme, which supports the growth of all organisms by converting atmospheric dinitrogen into ammonia, contains three different redox-active iron sulfur clusters that are central to its function. Dna2, found in all eukaryotes, is integral to genome maintenance and coordinates an iron sulfur cluster of unknown function. Many details of the nitrogenase mechanism are yet to be revealed and pursuits toward this goal will support human efforts to develop more sustainable solutions to nitrogen fixation, which is required for maintaining our food supply. Thorough characterization of the DNA-maintenance enzyme Dna2 will allow us to develop better technologies for cancer prevention and treatment. Development and optimization, as well as technical critique, of a variety of analytical chemistry techniques were performed toward the goal of increasing our understanding of these two important enzymes. Yeast Dna2 was successfully overexpressed and purified from *E. coli* and spectroscopic features of the 4Fe-4S cluster were characterized. Toward measuring the redox potential of the 4Fe-4S cluster of Dna2, the DNA-modified electrochemistry technique was evaluated leading to the discovery that the source of electrochemical signals proposed to be due to redox activity of 4Fe-4S clusters in DNA-binding proteins are actually due to the redox activity of Fe-EDTA complexes that form in the buffers of these proteins. These results will support future scientists in accurately interpreting the electrochemical signals from DNA-modified electrochemistry. The solvent isotope effect of nitrogenase reduction was investigated by measuring deuterium incorporation into nitrogenase products by GC-MS, FTIR and NMR, revealing that the enzyme exhibits modest preference for H vs. D in acetylene reduction to ethylene, but significant preference for H in the reduction of protons to H₂. These results indicate that there are distinct mechanisms of H atom transfer in the reduction of these two substrates and the experimental design that we developed opens the door for a new avenue of nitrogenase research to reveal the solvent isotope effects of reduction of a variety of different substrates under different experimental conditions. Finally, a new ATPase assay using ion chromatography was developed to measure ATPase activity of the Fe protein, which provides a tool for future pursuits toward quantifying P_i release by ATPases and led to our surprising result that the apo-form of the Fe protein is active in ATP hydrolysis.

TABLE OF CONTENTS

Acknowledgements	iii
Abstract	vii
Table of Contents	viii
List of Figures	x
List of Tables	xiii
Chapter I: Introduction	1
Chapter II: Isolation of active yeast Dna2 with 4Fe-4S Cluster from <i>E. coli</i>	4
2.1 Introduction	4
2.2 Methods	6
2.3 Results	8
2.4 Conclusions and Future Outlook	10
Chapter III: Critical investigation of the electrochemical signal observed from 4Fe-4S cluster proteins on DNA-modified gold electrodes using a series of control experiments	14
3.1 Introduction	14
3.2 Methods	17
3.3 Results	20
3.4 Conclusions and Future Outlook	44
Chapter IV: Investigating the Mechanism of Nitrogenase Reduction with Proton Inventory Studies	49
4.1 Introduction	49
4.2 Methods	54
4.3 Results	58
4.4 Conclusions and Future Outlook	71
Chapter V: Characterization of Metal Content and ATPase Activity of Holo- and Apo-Av2 Proteins of Nitrogenase (in collaboration with Ailiena Maggiolo)	78
5.1 Introduction	78
5.2 Methods	81
5.3 Results	82
5.4 Conclusions and Future Outlook	87
Appendix A: Supporting Information for Critical Investigations of the Electrochemistry of Dna2	90
A.1 Cyclic Voltammetry of premixed solution of Fe ²⁺ and EDTA on DNA-modified electrodes in HEPES Buffer	90
A.2 Cyclic Voltammetry of premixed solution of Fe ²⁺ and EDTA on DNA-modified electrodes in Tris Buffer	91
Appendix B: Supporting Information for Isotope Effect Studies of Nitrogenase	92
B.1 Nitrogenase Purification	92
B.2 Gas Chromatographs of Headspace of Acetylene Reduction Assays	93

B.3	Mass Spectra of Ethylene Peak of Headspace of Acetylene Reduction Assays	94
B.4	Deconvolution of Overlapping Mass Spectra of Ethylene Isotopologues . . .	95
B.5	FTIR Standard Curves of Deuterated Ethylenes	98
B.6	FTIR Spectra of Headspace of Acetylene Reduction Assays	100
B.7	¹ H NMR Spectra of Headspace of Proton Reduction Assays	102
B.8	Attempt to quantify H ₂ , HD, and D ₂ by GC-MS	105
B.9	Derivation of Isotope Effect Model Curves	112
B.10	Least Square Fit of Acetylene and Proton Reduction Assay Results	114
B.11	Estimation of Fractionation Factor of H ₂ Production by Nitrogenase	117
B.12	Mass Spectra of Methane Peak of Headspace of NaCN Reduction Assays .	119
B.13	Possible Pathways for Formation of Methane Isotopologues from Cyanide by Nitrogenase	120

LIST OF FIGURES

<i>Number</i>	<i>Page</i>
2.1 Crystal structure of mouse Dna2 (2.3 Å, PDB = 5EAX) in complex with a 21 nt single stranded DNA substrate (ssDNA)	5
2.2 UV Vis Spectrum of representative sample of purified recombinant Dna2 (15 µM 4Fe-4S cluster, 21 µM, 72% cluster loaded)	9
2.3 EPR spectra at 10K of 15 µM recombinant yeast Dna2 as purified (red) or after treatment with 5X potassium ferricyanide (orange) for 1 min	10
2.4 Nuclease assay time trial of recombinant yeast Dna2	11
2.5 Quantification of nuclease activity of Dna2 from nuclease assay show in Figure 2.4. Percent substrate cleaved = (short products/(short prod. + long prod.)) x 100%. Quantified using ImageQuantTL software. Error bars are standard deviation of two trials.	12
3.1 Overview of DNA-modified and protein film electrochemistry on DNA-binding 4Fe-4S cluster proteins	21
3.2 Cyclic Voltammograms of 6 µM Dna2 on putative DNA-modified gold electrode before and after addition of 5 mM ATP	22
3.3 Characterization of putative DNA-monolayer with ferricyanide and ruthenium hexamine	23
3.4 Cyclic voltammogram of EndoIII (17 µM) on putative DNA-modified gold electrode	25
3.5 Cyclic Voltammograms of 6 µM Dna2 on multiplexed gold electrodes with beta-mercaptohexanol monolayer	27
3.6 Cyclic Voltammograms of 6 µM Dna2 on multiplexed gold electrodes with β-mercaptohexanol monolayer before and after addition of 5 mM ATP	28
3.7 Addition of ATP to buffer on multiplexed gold electrode with β-mercaptohexanol monolayer	29
3.8 CVs of Dna2 on gold electrode with β-mercaptohexanol monolayer and on bare gold electrodes	30
3.9 UV Vis Spectra of Dna2 before and after putative DNA-modified Electrochemistry	31
3.10 Cyclic Voltammetry of Fe ²⁺ and EDTA mixed on putative DNA-modified electrode	33

3.11	Cyclic Voltammetry of premixed solution of Fe ²⁺ and EDTA on putative DNA-modified electrodes in HEPES buffer	35
3.12	Cyclic Voltammetry of premixed solution of Fe ²⁺ and EDTA on putative DNA-modified electrodes in Tris buffer	36
3.13	Square wave voltammetry of FeEDTA and EndoIII on putative DNA-modified electrodes	37
3.14	Cyclic Voltammetry of 13 μ M EndoIII without EDTA	39
3.15	Addition of 0.5 mM EDTA to EndoIII on gold electrode with β -mercaptohexanol monolayer	40
3.16	Addition of 0.5 mM EDTA to EndoIII on gold electrode with putative DNA monolayer	41
3.17	Addition of 0.4 mM EDTA to Dna2 on gold electrode with and without putative DNA monolayer	43
4.1	Scheme of isotope effect experiments of acetylene and proton reduction assays by nitrogenase from <i>A. vinelandii</i>	53
4.2	Total acetylene and proton reduction activity of nitrogenase in mixed isotope buffers	59
4.3	Quantification of isotopologue products of nitrogenase acetylene (ARA) and proton reduction assays (PRA) in 51% D ₂ O	61
4.4	Proton inventory analysis of acetylene and proton reduction by nitrogenase	64
4.5	Time course of NaCN reduction assays in H ₂ O and 72% D ₂ O	66
4.6	Distribution of methane isotopologue products from nitrogenase NaCN reduction assays in 51% D ₂ O and 72% D ₂ O	69
4.7	Models for the mole fraction of methane isotopologue product as a function of isotope effect in assays at 51% D ₂ O	70
4.8	Models for the mole fraction of methane isotopologue product as a function of isotope effect in assays at 72% D ₂ O	71
5.1	Schematic of crystallization kinetics to demonstrate apoFeP crystals form by co-crystallization of holoFeP with nucleotide	80
5.2	ATPase time trial of holo- and apo-Av2 with Av1 and ATP regeneration system	84
5.3	ATPase time trial of holo- and apo-Av2 with Av1 and ATP regeneration system at low component ratio (Av2 saturated by Av1, CR = 0.05)	85
5.4	ATPase time trial of holo- and apo-Av2 with Av1 and ATP regeneration system at component ratio = 0.25	86

5.5	ATPase time trial of control samples from ATPase assay reported in Figures 5.2 and 5.3	87
A.1	Cyclic voltammetry of 2.5 μ M FeEDTA on DNA-modified electrodes . . .	90
A.2	Cyclic voltammetry of 2.5 μ M FeEDTA on DNA-modified electrodes . . .	91
B.1	Representative FPLC traces and denaturing gels from purification of nitrogenase enzyme from <i>Azotobacter vinelandii</i>	92
B.2	Representative gas chromatogram of headspace of acetylene reduction assay of nitrogenase in 100% H ₂ or 51% D ₂ O	93
B.3	Mass spectra of ethylene peaks of headspace of acetylene reduction assays in 100% H ₂ O, 25% D ₂ O, 51% D ₂ O, and 73% D ₂ O	94
B.4	FTIR standard curves of ethylene isotopologues C ₂ H ₄ and C ₂ H ₃ D	99
B.5	FTIR spectra of the headspace of acetylene reduction assays performed in varying mole fraction of deuterium in the solvent	100
B.6	H ₂ /HD region of ¹ H NMR spectra from headspace of proton reduction assay	102
B.7	Full ¹ H NMR spectra from headspace of proton reduction assay	103
B.8	H ₂ /HD region of ¹ H NMR spectra from headspace of proton reduction assays in 100% H ₂ O, 25% D ₂ O, 51% D ₂ O, and 73% D ₂ O without deuterium decoupling	104
B.9	Mass Spectra of H ₂ , HD, and D ₂ standards	106
B.10	Standard Curve of H ₂ , HD, and D ₂ quantified by GC-MS	107
B.11	Least squares fits of Equations 4.1-4.3 to experimental acetylene reduction assay results to calculate isotope effect of acetylene reduction	114
B.12	Least squares fit of Equation 4.6 to mole fraction of deuterium added during acetylene reduction assays	115
B.13	Least squares fit of experimental proton reduction assay results to Equation 4.7	116
B.14	Mass spectra of methane peaks of headspace of NaCN reduction assays in 100% H ₂ O, 51% D ₂ O, and 73% D ₂ O	119
B.15	Schematic of formation of methane isotopologues by nitrogenase in mixed H ₂ O/D ₂ O buffers	120

LIST OF TABLES

<i>Number</i>		<i>Page</i>
2.1	Sequences of DNA Substrates used for Dna2 Nuclease Assays	8
3.1	Sequences of DNA Substrates used for DNA-modified electrochemistry . .	18
4.1	Isotope Effects of Acetylene and Proton Reduction by Nitrogenase	65
4.2	Distribution of Methane Isotopologue Products from Nitrogenase Cyanide Reduction Assays in 51% and 72% D ₂ O	67
5.1	Concentration of Av2 Samples Determined by Amino Acid Analysis	81
5.2	Ratio of Fe atoms to Av2 Dimers in Holo- and Apo-Av2 samples	82
B.1	Relative Amounts of Ethylene Isotopologue Products of Acetylene Reduc- tion Assays Quantified by GC-MS	97
B.2	Relative Amounts of Ethylene Isotopologue Products of Acetylene Reduc- tion Assays Quantified by FTIR	101
B.3	GC-MS Quantification of Hydrogen Isotopologues Produced in Proton Reduction Assays of Nitrogenase	110
B.4	Calculating Fractionation Factor of Proton Reduction	118

Chapter 1

INTRODUCTION

Iron Sulfur Cluster Proteins

Metalloenzymes, ubiquitous in biology with important roles for health and the climate, require specialized handling procedures and can be studied with many physical and spectroscopic techniques that aren't applicable to enzymes that don't host metal centers. Iron-sulfur clusters, a particular class of enzyme metallocofactors, fulfill many different functions and can exist in a variety of forms. The cubane 4Fe-4S cluster is particularly common and can play structural, redox, and/or catalytic roles in enzymes [1–3].

Recently, many DNA-processing enzymes, such as the DNA-repair enzyme Dna2, have been found to coordinate 4Fe-4S clusters [4–6]. The presence of metallocofactors in many DNA-processing enzymes evaded discovery for many years after first characterization of the enzyme because the clusters are sensitive to oxidative degradation and many of these enzymes are stable without their 4Fe-4S cluster [7]. The presence of redox active 4Fe-4S clusters in these proteins is intriguing because the clusters themselves are not required for enzymatic activity and the 4Fe-4S cluster biogenesis pathway is energetically expensive. Furthermore, it is surprising that nature would engineer a possible source of reactive oxygen species', known to cause damage to DNA, in an enzyme that binds DNA [8, 9]. Understanding the role of 4Fe-4S clusters in DNA-binding enzymes will reveal this evolutionary mystery and be valuable in developing strategies to support the integrity of our genomes.

The nitrogenase enzyme complex also coordinates a 4Fe-4S cluster, as well as two other iron sulfur clusters of unique form. The iron sulfur clusters of nitrogenase have been well studied and are understood to play electron transfer and catalytic roles. The most unique of the clusters, a 7Fe-8S-Mo cluster, is the active site of the enzyme where nitrogenase performs electron and proton transfers leading to the multi-electron reduction of a variety of substrates [10, 11]. Despite much focus on the mechanism at this iron sulfur cluster, there are still many unanswered questions about how substrates bind to the cluster and are reduced.

A common feature of these two iron sulfur cluster enzymes is their sensitivity to oxygen and thus, anaerobic techniques are required to uphold the integrity of their structure and function. Although Dna2 can be overexpressed and purified aerobically (although with

attempts to minimize oxygen exposure), nitrogenase must be strictly kept under atmosphere without oxygen [10]. For both of these enzymes, the atmosphere under which samples are prepared is extremely important and must be kept in mind when designing experiments and evaluating literature results. There is a rich history of literature on Dna2 due to its relevance for preventing and treating cancer; however, many of these results were obtained from experiments performed aerobically because the authors were unfamiliar with the oxygen sensitivity of the 4Fe-4S cluster [12, 13]. Although we observed that the 4Fe-4S cluster of Dna2 is stable for a few hours in air, it is important that the oxidation state and possible oxidative degradation of the 4Fe-4S cluster be considered in future experiments to develop a better understanding of the role of the 4Fe-4S cluster in Dna2.

The presence of iron sulfur clusters in Dna2 and nitrogenase bestows them with the ability to occupy multiple oxidation states. The iron sulfur cluster of Dna2 is thought to transition between the 2+ and 3+ states; however, other than the the EPR-silent $[4\text{Fe-4S}]^{2+}$ "signal" that we report in this work, these states have not been isolated and observed spectroscopically and the redox potential of the cluster is unknown. The 4Fe-4S cluster of nitrogenase occupies the 1+/2+ couple during turnover [14], and there is growing evidence that the apo-form of the enzyme without the 4Fe-4S cluster also has a physiologically relevant role [15]. The intermediate cluster in the electron transfer pathway of nitrogenase, the P-cluster, is a 8Fe-7S cluster that transitions between the $[8\text{Fe-7S}]^{2+}$ and $[8\text{Fe-7S}]^{3+}$ oxidation states during turnover [16]. Finally, the 7Fe-8S-Mo active site cluster of nitrogenase can build up many reducing equivalents, although it is thought that these electrons are stored as hydrides on the cofactor and the metallocofactor itself only transitions between two redox states [17]. The oxidation states of the iron sulfur clusters of nitrogenase are central to the function of the enzyme and the role of the oxidation state of the 4Fe-4S cluster in Dna2 is still an exciting open question that warrants further study.

In the Dna2 chapters of this work, the 4Fe-4S cluster is the focus, revealing spectroscopic features of the cluster and characterizing its stability. DNA-modified electrochemistry was pursued to measure the redox potential of the iron sulfur cluster as has been performed previously for iron sulfur cluster proteins that bind DNA [18]; however, our work uncovers that DNA-modified electrochemical signals can be due to artifacts of the redox active Fe-EDTA complex that can form in buffers of iron sulfur cluster proteins. The nitrogenase chapters of this work focus on revealing details of the reduction mechanism. We have observed a significant difference in the solvent isotope effect of proton reduction and acetylene reduction by nitrogenase, revealing that the pathway of H atoms toward the products in these two reactions are distinct. Additionally, we have discovered that a

novel form of the apo-Fe protein of nitrogenase is an active ATPase. Overall, this work contributes to our growing understanding of the properties and functions of iron sulfur clusters in biological systems.

References

- (1) Beinert, H.; Holm, R. H.; Münck, E. *Science* **1997**, *277*, 653–659.
- (2) Fontecave, M. *Nat. Chem. Biol.* **2006**, *2*, 171–174.
- (3) Rees, D. C.; Howard, J. B. *Science* **2003**, *300*, 929–931.
- (4) Fuss, J. O.; Tsai, C. L.; Ishida, J. P.; Tainer, J. A. *Biochim Biophys Acta* **2015**, 1253–1271.
- (5) Mettert, E. L.; Kiley, P. J. *Biochim Biophys Acta* **2015**, 1284–1293.
- (6) White, M. F.; Dillingham, M. S.; Phillips, S.; Luger, K. *Curr. Opin. Struct. Biol.* **2012**, *22*, 94–100.
- (7) Silva, R. M. B.; Grodick, M. A.; Barton, J. K. *J. Am. Chem. Soc* **2020**, *142*, 10964–10977.
- (8) Désirée Paul, V.; Lill, R. *Biochim Biophys Acta* **2015**, 1528–1539.
- (9) Pogozelski, W. K.; Tullius, T. D. *Chem. Rev.* **1998**, *98*, 1089–1107.
- (10) Einsle, O.; Rees, D. C. *Chem. Rev.* **2020**, *120*, 4969–5004.
- (11) Spatzal, T.; Aksoyoglu, M.; Zhang, L.; Andrade, S. L.; Schleicher, E.; Weber, S.; Rees, D. C.; Einsle, O. *Science* **2011**, *334*, 940.
- (12) Levikova, M.; Cejka, P. *Nucleic Acids Res.* **2015**, *43*, 7888–7897.
- (13) Pokharel, S.; Campbell, J. L. *Nucleic Acids Res.* **2012**, *40*, 7821–7830.
- (14) Wenke, B. B.; Spatzal, T.; Rees, D. C. *Angew. Chem. Int. Ed.* **2019**, *58*, 3894–3897.
- (15) Hu, Y.; Corbett, M. C.; Fay, A. W.; Webber, J. A.; Hodgson, K. O.; Hedman, B.; Ribbe, M. W. *PNAS* **2006**, *103*, 17125–17130.
- (16) Danyal, K.; Dean, D. R.; Hoffman, B. M.; Seefeldt, L. C. *Biochemistry* **2011**, *50*, 9255–9263.
- (17) Lukoyanov, D.; Khadka, N.; Yang, Z.-Y.; Dean, D. R.; Seefeldt, L. C.; Hoffman, B. M. *J. Am. Chem. Soc.* **2016**, *138*, 10674–10683.
- (18) Barton, J. K.; Bartels, P. L.; Deng, Y.; O'Brien, E. *Meth. Enzymol.* **2017**, *591*, 355–414.

*Chapter 2*ISOLATION OF ACTIVE YEAST DNA2 WITH 4FE-4S CLUSTER
FROM *E. COLI***2.1 Introduction**

Dna2 is a nuclease-helicase found in all eukaryotic organisms with an impressive repertoire of DNA maintenance activity. Essential in yeast [1] and required for embryonic development in mice [2], Dna2 is a major player in Okazaki fragment processing during DNA replication, double strand break repair, telomere maintenance, and mitochondrial DNA maintenance [3–6]. Due to its major contributions to genome stability, it is not surprising that both Dna2 upregulation and mutation have been observed in various types of cancer [7, 8]. The replication stress associated with hyperproliferation of cancer cells is alleviated by the overexpression of Dna2, providing these cells with a survival advantage that promotes tumorigenesis [9]. On the other hand, due to the role of Dna2 in maintaining genome stability, disabling mutations in the enzyme can cause cells to be more susceptible to cancer-causing mutations [10]. Dna2, as well as other DNA nuclease-helicases involved in alleviating oncogene-activated replication stress, is an active target for anti-cancer inhibitors. The prevalence of Dna2 overexpression in the early stages of many cancers, most notably basal-like breast cancer, suggests that Dna2 is a promising biomarker for early detection of the disease [9].

Dna2 contains an N-terminal nuclease domain and a C-terminal helicase domain, both of which are highly conserved from yeast to humans (Figure 2.1). The overall shape of the protein is cylindrical with an internal tunnel that contains the nuclease active site. The nuclease activity of Dna2 requires a single-stranded DNA (ssDNA) flap, consistent with the fact that ssDNA, and not double-stranded DNA (dsDNA), fits within the tunnel. The nuclease domain resides at the base of the cylinder in a doughnut-like shape and the helicase domain is positioned 5' - to the nuclease domain. A 4Fe-4S cluster is coordinated by four cysteine residues (C136, C394, C397, and C402 in mouse Dna2) of the nuclease domain and is located 9 Å from the entry point of the tunnel, which is the expected location of the ssDNA-dsDNA junction [11].

Despite the fact that both the helicase and nuclease domains are equally conserved in evolution, the nuclease function of Dna2 dominates on most substrates and only the nuclease-deficient mutant causes cellular lethality in yeast. One explanation for the

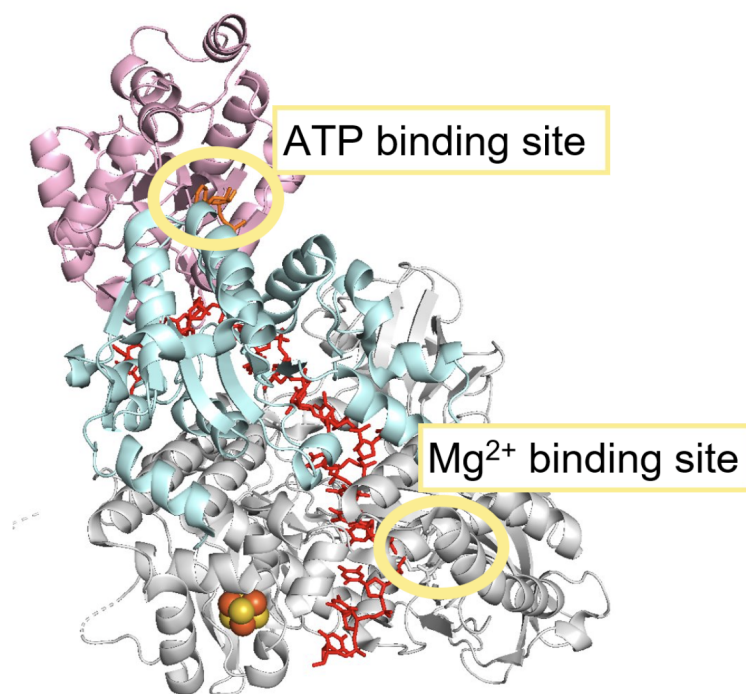


Figure 2.1: Crystal structure of mouse Dna2 (2.3 Å, PDB = 5EAX) in complex with a 21 nt single stranded DNA substrate (ssDNA) [11]. Nuclease domain shown in gray, helicase domains shown in blue and pink. ATP binds in cleft the two helicase domains. 4Fe-4S cluster (shown as spheres) located about 9 Å from the end of the ssDNA substrate.

relatively weak helicase function is the fact that the helicase domain resides 5'- to the nuclease domain making helicase function dependent on nuclease inactivation. The mechanism through which Dna2 modulates the nuclease domain to allow for helicase activity is not well understood. Post-translational modification and protein partners have been suggested as possible regulators of this functional switch [12]. The redox state of the 4Fe-4S cluster was also proposed to be involved in this switch; however, the redox behavior of the cluster has not been investigated.

Although Dna2 has been extensively studied biochemically, there is need for a more thorough characterization of the 4Fe-4S cluster, not only to understand its role for the function of the enzyme, but also to establish proper enzyme-handling guidelines to maintain the integrity of the cluster. This report includes the first heterologous isolation of wild-type yeast Dna2 and the nuclease-dead mutant Dna2 E675A from *E. coli* resulting in robust 4Fe-4S cluster loading during expression and stability during purification. The 4Fe-4S cluster of recombinant Dna2 is characterized by UV-Vis and EPR Spectroscopy. The nuclease and DNA-binding activity of Dna2 under anaerobic conditions has been studied using

radiolabeled oligonucleotide substrates. This study begins to illuminate the biochemical role played by the 4Fe-4S cluster and provides insight into the mechanism through which Dna2 promotes genome stability. Focus on the 4Fe-4S cluster is an unexplored avenue of inquiry for this well-studied enzyme and will greatly improve our understanding of how Dna2 supports the stability of the genome. A richer understanding of the role of the 4Fe-4S of Dna2 in DNA replication processes will help to reveal the pathway of cancer evolution and will aid in the development of Dna2 inhibitors for cancer therapy.

2.2 Methods

Overexpression of yeast Dna2 and Dna2 E675A in E. coli

The full length wild-type yeast *dna2* gene or the nuclease-dead mutant *dna2 E675A* was cloned into a pQTEV vector with a cleavable N-terminal 6xHis tag by a former Barton group member, Helen Segal (gift from the Campbell lab). The vector contains the Ampicillin resistance marker and a lactose promoter. This plasmid was sequenced showing no mutations and was harbored in Rosetta (DE3) pLysS E. Coli cells. The pLysS plasmid suppresses basal expression at the T7 promoter and is retained by a Chloramphenicol resistance marker. After streaking the Rosetta pLys full length yDna2 cell stocks on LB/Agar plates with the appropriate antibiotics, an overnight culture with the appropriate antibiotics (25 mg/L Chloramphenicol, 100 mg/L Ampicillin) was inoculated. The next morning the overnight culture was cloudy and six flasks containing 1.5 L autoclaved Terrific Broth (Sigma) with the appropriate antibiotics were inoculated with 11 mL of the overnight culture each. The culture was grown at 37 °C and 225 RPM until they reached an O.D. of 0.68 to 0.84, at which point they were transferred to the 16 °C incubator and expression was induced with 200 µM IPTG. For the Dna2 E675A over expression in Jan 2019, the cells were supplemented with 100 mg/mL ammonium iron(III) citrate, 100 mg/mL iron(II) sulfate heptahydrate, and 2mM cysteine. The cells were harvested after expressing at 16 °C and 150 RPM for 21 hours.

Purification of yeast Dna2 with anaerobic cell lysis

The day before the purification, 1 L of HisTrap A buffer was degassed using the vacuum manifold in the Rees lab. To purify yeast Dna2, cells (46 g pellet) were homogenized in HisTrap Buffer A (20 mM Tris, 0.5 M NaCl, 5% glycerol, pH 7.75, 2 mM DTT, 500 mL) with 10 protease inhibitor tablets and 2 vials (20,000 KU) of DNase in the glove bag. The homogenized cells were transferred to a 0.5 L round bottom flask that was capped with a septum and sealed with parafilm. The flask was removed from the glove bag and brought to the Rees lab for anaerobic lysis. The cells were lysed with two passes through

the Emulsiflex, collecting the lysed cells on ice. The solution was slightly warm as it came out of the Emulsiflex. The lysed cells were spun at 13,000 RPM for 30 minutes and the supernatant (~500 mL) was filtered before loading onto double stacked nickel columns (GE Healthcare) equilibrated in HisTrap Buffer A. The column was washed in three steps: an initial phase of 4 column volumes of 97% HisTrap Buffer A/3% HisTrap Buffer B (20 mM Tris, 0.5 M NaCl, 0.5 M imidazole, 5% glycerol, pH 7.75, 0.5 mM DTT), followed by a gradient of 3-10% His Trap Buffer B over 6 column volumes, and a final wash with a gradient of 10-11% His Trap Buffer B until the absorbance at 280 nm decreased completely. Recombinant Dna2 was then eluted with a gradient of 11-100% His Trap Buffer B with the center of the eluted peak at 50% His Trap Buffer B (fractions 8-17). This peak was buffer exchanged into 20% Anion Exchange Buffer A (20 mM Tris, 0.1 mM EDTA, 5% glycerol, pH 7.75, 1 mM DTT)/80% Anion Exchange Buffer B (20 mM Tris, 0.1 mM EDTA, 1 M NaCl, 5% glycerol, pH 7.75, 1 mM DTT) using a desalting column (GE Healthcare). All of the eluant from the desalting column was loaded onto the HiTrap Q anion exchange column (GE Healthcare) and eluted with a gradient of 11-100% Anion Exchange Buffer B over five column volumes. The peak with 410nm absorbance (Fractions 5-10) from the anion exchange column were collected, combined and concentrated to 4.5 mL using Amicon centrifugal filter devices at 6500 RPM. This sample was loaded onto a size exclusion column (GE Healthcare) equilibrated with SEC Buffer (20 mM Tris, 0.5 M NaCl, 0.1 mM EDTA, 5% glycerol, pH 7.75, 1 mM DTT) and eluted after 130 mL of elution with SEC Buffer. This peak containing purified yeast Dna2 was concentrated and analyzed with UV Vis. The concentration of Dna2 was calculated with the 280 nm absorbance and the Expasy Dna2 extinction coefficient (94550 M⁻¹ cm⁻¹) and the concentration of 4Fe-4S cluster was calculated with the 410 nm absorbance and the iron sulfur cluster extinction coefficient (17000 M⁻¹ cm⁻¹). The percent cluster loading was the concentration of 4Fe-4S cluster divided by the concentration of protein multiplied by 100%. Aliquots were taken of the final purified protein and of fractions throughout the purification and were analyzed with denaturing gel electrophoresis.

Nuclease Assay of Dna2

The procedure for the nuclease assay was slightly adapted from that used by Professor Judy Campbell to study Dna2 nuclease activity [13]. Indicated amounts of recombinant Dna2 (0.05 nM, 0.125 nM, 0.5 nM, 1.25 nM, or 7.5 nM) were incubated at 37 °C with 600 fmol of radiolabeled oligonucleotide (sequences E, F, G in Appendix Table1) in 30 μ L of reaction volume containing 50 mM Tris-HCl (pH 8.0), 2mM dithiothreitol (DTT), 0.1 mg/mL BSA, 30 mM NaCl, 2 mM MgCl₂, and 5% glycerol. To stop the reaction,

Table 2.1: Sequences of DNA Substrates used for Dna2 Nuclease Assays

DNA Strand	Sequence (5' – 3')
HS Hairpin (nuclease assay)	TTC ACG AGA TTT ACT TAT TTC ACT GCG GCT ACA TGA TGC ATC GTT AGG GCA TTC CGC CTA ACG ATG CAT CAT GT
18ntover comp	TTC ACT AGA TTT AGC TCT GGA ACT GAA CCC GTC CTG CGT CAA CTA CAT GAA CAC CTC
MST temp	GAG GTG TTC ATG TAG TTG ACG CAG GAC GGG TTC AGT

20 μ L of the reaction mixture was added to a 10 μ L solution of SDS and EDTA so that the final concentrations were 0.1 % SDS and 10 mM EDTA. The samples were then heat denatured with incubation at 90 °C for 10 minutes. The samples were dried on the speed vac and their radioactivity was measured using the scintillation counter. The samples were dissolved in the appropriate volume of blue loading dye to normalize their radioactivity. They were loaded onto a 20% sequencing gel and the gel was run for 3 hours at 90W. The gel was exposed for (300,000/radioactivity per well) hours and visualized using the Typhoon 9400 phosphorimager with ImageQuantTL software.

2.3 Results

Overexpression and purification of yeast Dna2 in *E. coli*

Recombinant *S. cerevisiae* Dna2 was successfully overexpressed and purified from *E. coli* with 72% 4Fe-4S cluster loading (Figure 2.2). Special overexpression techniques were employed to facilitate this high 4Fe-4S cluster-loading including filling the expression flasks with 1.5 L of culture (instead of the standard 1 L) to limit aeration during shaking, and decreasing the incubation temperature to 16 °C upon induction of expression to slow the overexpression, allowing time for sufficient 4Fe-4S cluster biogenesis. The purification process was made as anaerobic as possible to limit oxidative degradation of the 4Fe-4S cluster. The cells were homogenized in an anaerobic chamber and lysed using an Emulsiflex under Argon. Although the FPLC system was not anaerobic, it was kept at 4 °C and the rest of the purification was performed quickly in one day (without any freeze-thaw cycles) to limit degradation of the 4Fe-4S cluster.

Spectroscopy of native and oxidized recombinant yeast Dna2

The UV-Vis of the recombinant Dna2 purified from *E. coli* showed the characteristic shoulder at 410 nm corresponding to the 4Fe-4S cluster (Figure 2.2). EPR spectroscopy of the Dna2 sample as purified was mostly EPR silent, which is consistent the 4Fe-4S

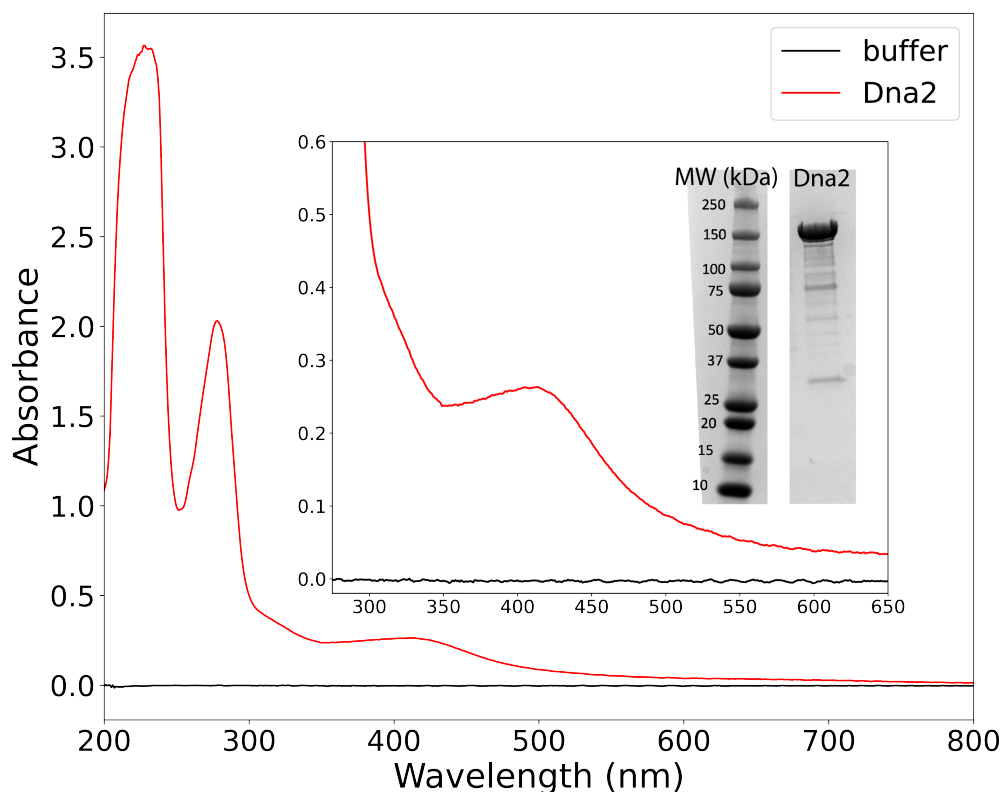


Figure 2.2: UV Vis Spectrum of representative sample of purified recombinant Dna2 (15 μM 4Fe-4S cluster, 21 μM , 72% cluster loaded). The concentration of Dna2 was calculated with the 280 nm absorbance and the Expasy Dna2 extinction coefficient ($94550 \text{ M}^{-1} \text{ cm}^{-1}$) and the concentration of 4Fe-4S cluster was calculated with the 410 nm absorbance and the iron sulfur cluster extinction coefficient ($17000 \text{ M}^{-1} \text{ cm}^{-1}$). Inset: denaturing protein gel electrophoresis of concentrated purified fractions after elution from the SEC column. Band around 150 kDa contains recombinant Dna2 (MW=172 kDa). Band around 75 kDa likely contains mostly truncated Dna2 and chaperone protein dnaK.

cluster being in the 2+ state (Figure 2.3). There was a small signal at $g = 2.008$, which increased significantly with treatment with the strong oxidant potassium ferricyanide. The strong signal at $g = 2.008$ is indicative of the $[\text{3Fe-4S}]^+$ cluster, indicating that potassium ferricyanide caused oxidative degradation of the $[\text{4Fe-4S}]^{2+}$ cluster of yeast Dna2 to the $[\text{3Fe-4S}]^+$ cluster, likely through a $[\text{4Fe-4S}]^{3+}$ cluster intermediate [14].

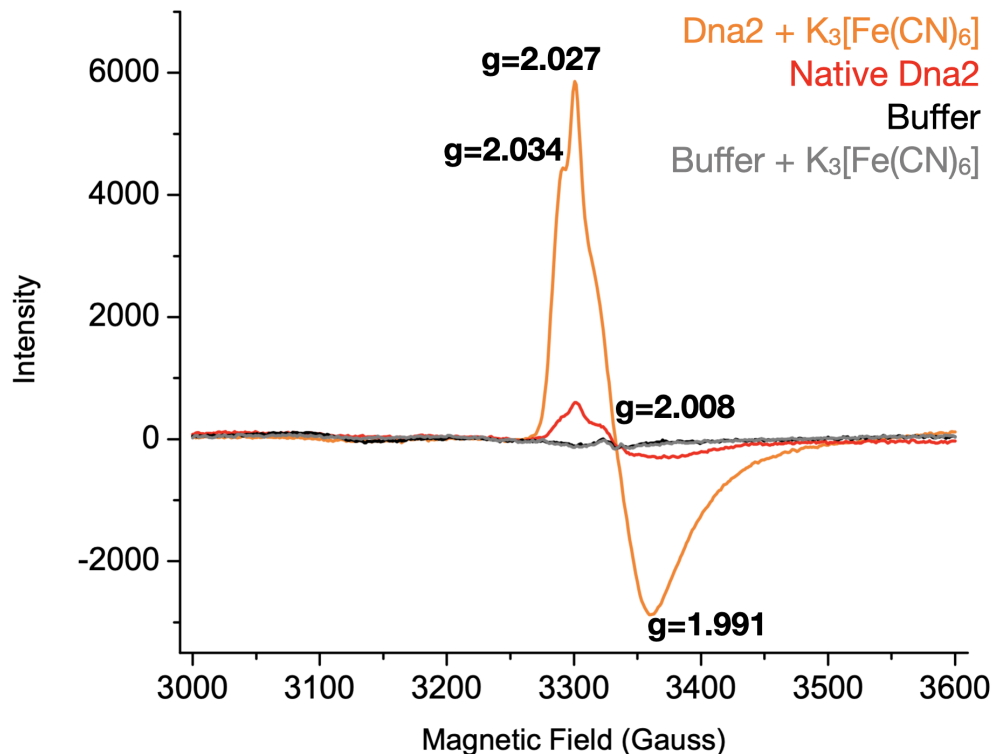


Figure 2.3: EPR spectra at 10K of 15 μ M recombinant yeast Dna2 as purified (red) or after treatment with 5X potassium ferricyanide (orange) for 1 min. Signal at $g = 2.01$ is representative of the $[3\text{Fe-4S}]^+$ cluster. Buffer = 20 mM Tris, 0.5 M NaCl, 0.1 mM EDTA, 5% glycerol, pH 7.74.

Anaerobic nuclease activity of recombinant Dna2

Recombinant yeast Dna2 showed robust nuclease activity (Figure 2.4 and 2.5), evidenced by the formation of short oligonucleotide products after 30 second incubation under nuclease assay conditions. Nuclease products were not observed in assays performed without magnesium chloride, consistent with previous reports indicating that Mg^{2+} is required for Dna2 nuclease activity [11]. At time points up to 5 min, the majority of products were of lengths 5–10 nucleotides (nt) and after 5 minutes, the majority of products were less than 5 nt.

2.4 Conclusions and Future Outlook

Dna2 from *S. cerevisiae* was successfully overexpressed and purified from *E. coli* with significant 4Fe-4S cluster loading and nuclease activity. EPR spectroscopy revealed that the majority of the 4Fe-4S clusters were in the EPR-silent 2+ state; however, the cluster was susceptible to oxidative degradation to the $[3\text{Fe-4S}]^+$ cluster with treatment with a

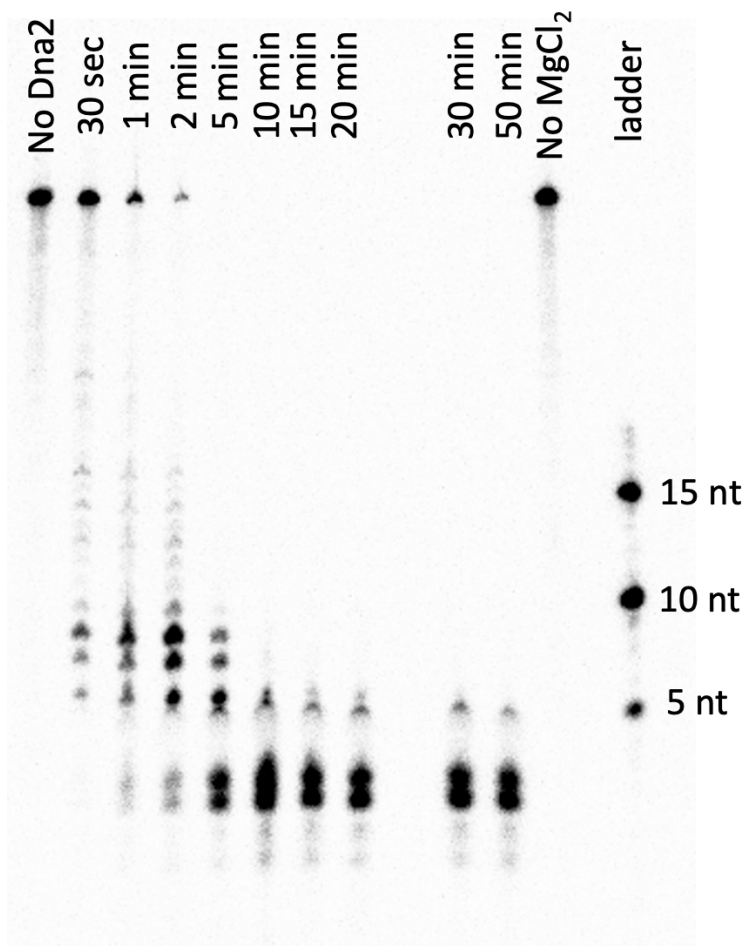


Figure 2.4: Nuclease assay time trial of recombinant yeast Dna2. Recombinant yeast Dna2 (3 nM) was incubated at 37 °C with 600 fmol of 5'- radiolabeled oligonucleotide in 30 μ L reaction volume containing 50 mM Tris-HCl (pH 8.0), 2 mM dithiothreitol (DTT), 0.1 mg/mL BSA, 30 mM NaCl, 2 mM MgCl₂, and 5% glycerol. Reactions quenched with 0.1 % SDS, 10 mM EDTA and incubation at 90 °C for 10 min. Samples loaded onto 20% sequencing gel. Gel was run for 3 hours at 90 W, exposed to a phosphor screen, and imaged using a Typhoon 9400 with ImageQuantTL software.

strong oxidant.

To our knowledge, this is the first report of heterologous expression of yeast Dna2 in *E. coli* with characterization of the integrity of the 4Fe-4S cluster. These reports will be valuable for future studies of Dna2, both by providing a route for heterologous expression of the enzyme and also for establishing protocols for protection and characterization of the 4Fe-4S cluster of Dna2.

Future studies should include a more complete characterization of the redox properties of

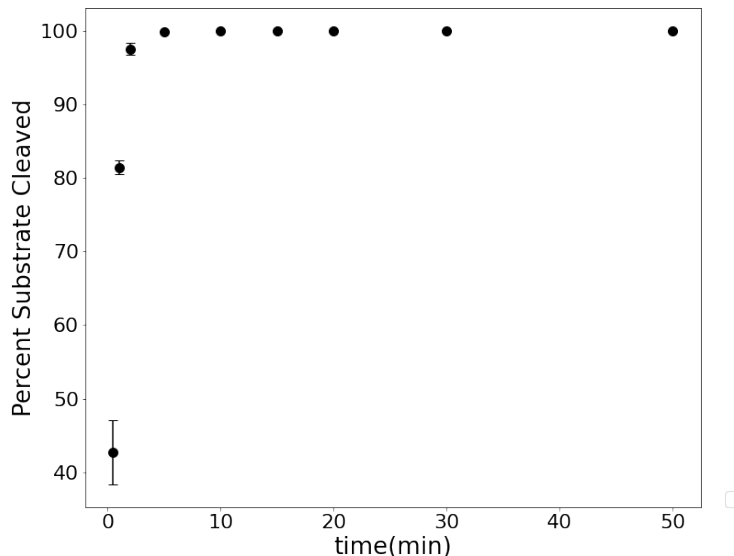


Figure 2.5: Quantification of nuclease activity of Dna2 from nuclease assay show in Figure 2.4. Percent substrate cleaved = (short products/(short prod. + long prod.)) \times 100%. Quantified using ImageQuantTL software. Error bars are standard deviation of two trials.

the 4Fe-4S cluster of yeast Dna2. By EPR, we were able to observe a signal representing the $[3\text{Fe-4S}]^+$ cluster, which is likely the product of oxidative degradation of the EPR-silent $[4\text{Fe-4S}]^{2+}$ cluster of native Dna2. This oxidative degradation pathway likely passes through the $[4\text{Fe-4S}]^{3+}$ intermediate; however, an EPR signal representative of this 3+ cluster was not observed. Future work should include treatment of Dna2 with milder oxidative conditions (possibly simply exposure to air) followed by analysis by EPR to observe the putative $[4\text{Fe-4S}]^{3+}$ signal. This would confirm that the 4Fe-4S cluster of Dna2 is a HiPiP cluster, exercising the $[4\text{Fe-4S}]^{2+}/[4\text{Fe-4S}]^{3+}$ redox couple, as expected [15, 16]. Furthermore, the redox potential of the cluster should be determined. DNA-modified electrochemistry was attempted toward this goal; however, no signal was observed from yeast Dna2 on DNA-modified electrodes over the background Fe-EDTA signal (see chapter III). Other methods for determining the redox potential are possible including performing a redox titration with an oxidant whose redox potential is close to the expected redox potential of Dna2 (100 mV vs. NHE) and that undergoes a color change upon reduction. These results would determine whether or not the 4Fe-4S cluster of Dna2 is redox active under physiological conditions and thus, whether it is possible that the 4Fe-4S cluster plays a redox role in the enzyme. In conclusion, the results reported here

lay the groundwork for performing a thorough characterization of the redox properties of the 4Fe-4S cluster of Dna2, an unexplored avenue of research for this important enzyme, which could provide valuable insight for designing cancer therapeutics.

References

- (1) Budd, M. E.; Campbell, J. L. *PNAS* **1995**, *92*, 7642–7646.
- (2) Lin, W.; Sampathi, S.; Dai, H.; Liu, C.; Zhou, M.; Hu, J.; Huang, Q.; Campbell, J.; Shin-Ya, K.; Zheng, L.; Chai, W.; Shen, B. *EMBO J.* **2013**, *32*, 1425–1439.
- (3) Levikova, M.; Cejka, P. *Nucleic Acids Res.* **2015**, *43*, 7888–7897.
- (4) Nanbu, T.; Nguyen, L. C.; Habib, A. G.; Hirata, N.; Ukimori, S.; Tanaka, D.; Masuda, K.; Takahashi, K.; Yukawa, M.; Tsuchiya, E.; Ueno, M. *PLoS One* **2015**, *10*, e0140456.
- (5) Ronchi, D. et al. *Am. J. Hum. Genet.* **2013**, *92*, 293–300.
- (6) Tamaro, M.; Liao, S.; Beeharry, N.; Yan, H. *Nucleic Acids Res.* **2016**, *44*, 221–231.
- (7) Lee, S. H.; Kim, Y. R.; Yoo, N. J.; Lee, S. H. *Korean J. Pathol.* **2010**, *44*, 354–359.
- (8) Strauss, C. et al. *Oncotarget* **2014**, *5*, 9396–9409.
- (9) Peng, G.; Dai, H.; Zhang, W.; Hsieh, H. J.; Pan, M. R.; Park, Y. Y.; Tsai, R. Y. L.; Bedrosian, I.; Lee, J. S.; Ira, G.; Lin, S. Y. *Cancer Res.* **2012**, *72*, 2802–2813.
- (10) Ölmezer, G.; Levikova, M.; Klein, D.; Falquet, B.; Fontana, G. A.; Cejka, P.; Rass, U. *Nat. Commun.* **2016**, *7*, 1–13.
- (11) Zhou, C.; Pourmal, S.; Pavletich, N. P. *eLife* **2015**, *4*, e09832.
- (12) Pinto, C.; Kasaciunaite, K.; Seidel, R.; Cejka, P. *eLife* **2016**, *5*, e18574.
- (13) Pokharel, S.; Campbell, J. L. *Nucleic Acids Res.* **2012**, *40*, 7821–7830.
- (14) Boal, A. K.; Yavin, E.; Lukianova, O. A.; O’Shea, V. L.; David, S. S.; Barton, J. K. *Biochemistry* **2005**, *44*, 8397–8407.
- (15) Fuss, J. O.; Tsai, C. L.; Ishida, J. P.; Tainer, J. A. *Biochim Biophys Acta* **2015**, 1253–1271.
- (16) Yeeles, J. T.; Cammack, R.; Dillingham, M. S. *J. Biol. Chem.* **2009**, *284*, 7746–7755.

*Chapter 3***CRITICAL INVESTIGATION OF THE ELECTROCHEMICAL SIGNAL OBSERVED FROM 4FE-4S CLUSTER PROTEINS ON DNA-MODIFIED GOLD ELECTRODES USING A SERIES OF CONTROL EXPERIMENTS****3.1 Introduction**

The phenomenon of DNA-mediated charge transfer (DNA CT) was discovered in the 1980s by Prof. Jacqueline Barton [1, 2]. Her work established that electrons/holes can pass through a strand of DNA through the overlapping π -orbitals of the DNA bases. The first investigation into whether this process could be studied on an electrode surface was published in 1997 in *Bioconjugate Chemistry* [3]. In this work, a self-assembled DNA monolayer was formed on a gold electrode surface and the surface was treated with the redox-active DNA-intercalator methylene blue. Cyclic voltammetry (CV) was performed on this surface and a reversible signal was observed, which the authors attributed to the DNA-mediated reduction and oxidation of methylene blue intercalated into the base stack of the DNA monolayer.

Further progress was made in the development of DNA-modified electrochemistry with two papers published in 1999 out of the Barton group [4, 5]. These reports used daunomycin (DA) as the redox active DNA intercalator, either covalently bound to the DNA at known positions or free in solution similar to the methylene blue in the previous reports. The results of this work showed that the distance from the electrode surface to the redox active species bound to the DNA did not affect the rate of charge transfer, suggesting that the rate limiting step of charge transfer in DNA-modified electrochemistry is tunneling through the alkane-thiol linker. This work also included control experiments in which a mismatched DNA base pair, known to attenuate DNA CT, was engineered in the DNA strand between the electrode and the DA, causing a complete abrogation of the signal in CV. These observations supported the conclusion that the electrochemical signal from DA arose from DNA CT.

In a 2003 contributed paper in *PNAS*, the Barton group reported the first use of DNA-modified electrodes to observe the redox activity of a DNA-binding protein, MutY, that contains a 4Fe-4S cluster [6]. MutY (800 μ M) was deposited onto a DNA-modified gold electrode and a reversible signal was observed by CV with a midpoint potential of 275

mV vs. NHE.¹ This signal was assigned to the 2+/3+ oxidation states of the 4Fe-4S cluster in MutY. As controls, the same protein solution was analyzed on a monolayer of β -mercaptohexanol (MCH) and on a DNA monolayer in which the DNA contained a mismatch to disrupt the π -stacking of bases, which attenuates DNA CT. In both control experiments, no signal was observed by CV. The 1990's saw a variety of publications from the Barton group investigating the electrochemistry of DNA repair enzymes MutY and EndoIII. In a 2006 article published in JACS, it was observed that the midpoint potential of EndoIII shifted negatively upon binding to DNA, leading to the conclusion that DNA binding primed the 4Fe-4S cluster of DNA repair enzymes for redox chemistry [8]. This observation was made by comparing the cyclic voltammogram of EndoIII on bare HOPG electrodes ($E_m = 250 \pm 30$ mV vs. NHE) with that of EndoIII on HOPG electrodes modified with DNA ($E_m = 20 \pm 10$ mV vs. NHE). The observation that the redox activity of these 4Fe-4S cluster DNA binding enzymes was accessible by DNA CT and that binding to DNA could modulate their midpoint potentials led to the development of a model for how these repair enzymes locate their substrate lesions in the genome [9]. In this model, DNA repair enzymes with 4Fe-4S clusters signal to each other using DNA CT, concentrating on strands with lesions where DNA CT is abrogated (see reference [9] for more detail).

In 2010, an important advancement was made in the field of DNA-modified electrochemistry with the development of multiplexed gold electrode chips. These silicon chips were fabricated with 16 gold working electrodes and fashioned with a plastic clamp and gasket that split the 16 gold electrodes into 4 quadrants. Now, different DNA monolayers could be deposited on the four separate quadrants and electrochemical measurements could be made in which the 4 quadrants share a common analyte/protein solution and a common reference and counter electrode. These multiplexed chips became the standard method for examining the redox activity of DNA binding enzymes with 4Fe-4S clusters in the Barton group. The Barton group continued their study of the redox activity of DNA repair enzymes, observing that two helicases with 4Fe-4S clusters, XPD and DinG, were redox active on DNA-modified electrodes and both had a midpoint potential of about 80 mV vs. NHE [6, 10–12]. Strikingly, this midpoint potential is in the range of that observed from EndoIII and MutY on DNA-modified gold electrodes under similar buffer conditions, further supporting the model that DNA repair enzymes can reduce and oxidize each other through DNA-mediated CT. Addition of ATP to the helicases caused an increase in the

¹This PNAS paper reports a potential of 275 mV, but a later publication [7] reports a midpoint potential of 90 mV for MutY on DNA-modified electrodes. This later report states that the 90 mV signal is similar to the 275 mV signal, however, this difference is as large as the stated difference in potential between DNA-bound and DNA-free protein and corresponds to a change in binding factor of 1000

intensity of the signal in CV, which was attributed to an increase in the coupling of the 4Fe-4S cluster of the protein to the DNA facilitated by a conformational change associated with ATP hydrolysis.

The Barton group expanded their scope of study to DNA replication enzymes in 2017, with a paper published in *Science* reporting the redox activity of the 4Fe-4S cluster of DNA primase on DNA-modified electrodes [13]. DNA primase and one of its cofactors, ATP, showed a midpoint potential of about 100 mV vs .NHE on DNA-modified gold electrodes. Without ATP, no signal was observed from DNA primase. However, a signal could be observed from DNA primase alone after bulk oxidation. After holding the potential at an oxidizing potential for 30 minutes, CV was performed on DNA primase and a cathodic peak around -135 mV vs NHE was observed in the first scan. The signal was not apparent after sweeping to reducing potentials. These results lead to the conclusion that DNA primase in its resting $[4\text{Fe-4S}]^{2+}$ state does not bind to DNA (and therefore a signal can't be observed in DNA-modified electrochemistry) and after oxidation to the 3+ state, it binds to DNA and can be observed by CV on DNA-modified electrodes. The authors further concluded that ATP increases the binding affinity of primase to DNA, allowing a reversible signal to be observed without bulk oxidation.

Another protein of interest to the Barton group, due to its integral role in genome maintenance and coordination of a 4Fe-4S cluster of unknown function, was *S. cerevisiae* Dna2. Dna2 is a nuclease-helicase found in all eukaryotic organisms with an impressive repertoire of DNA maintenance activity. Essential in yeast and required for embryonic development in mice, Dna2 is a major player in Okazaki fragment processing during DNA replication, double strand break repair, telomere maintenance, and mitochondrial DNA maintenance [14–19]. Due to its major contributions to genome stability, it is not surprising that both Dna2 upregulation and mutation have been observed in various types of cancer [20, 21]. A 4Fe-4S cluster is coordinated by four cysteine residues (C136, C394, C397, and C402 in mouse Dna2) of the nuclease domain of Dna2 and is located 9 Å away from the expected location of the double stranded region of the DNA substrate [22]. The mechanism through which Dna2 modulates nuclease and helicase activities is not well understood. Post-translational modification and protein partners have been suggested as possible regulators of this functional switch. The redox state of the 4Fe-4S cluster was also proposed to be involved in this switch; however, the redox behavior of the cluster has not been investigated [23].

The goal of this work was to elucidate the effect of the redox properties of the 4Fe-4S cluster on the regulation of helicase and nuclease activity in *S. cerevisiae* Dna2. Toward

this end, yeast Dna2 was overexpressed and purified from *E. coli* and DNA-modified electrochemistry experiments on purified yeast Dna2 were performed. A reversible signal was observed from Dna2 on DNA-modified electrodes with a midpoint potential of about 90 mV vs. NHE, similar to that of all other DNA-binding 4Fe-4S cluster proteins studied in the Barton group. This signal was assigned to the reduction and oxidation of the $[4\text{Fe-4S}]^{2+/3+}$ cluster of Dna2 through DNA-mediated charge transfer, as was concluded from previous work on other DNA-binding enzymes with 4Fe-4S clusters. Additionally, ATP was added to Dna2 on DNA-modified electrodes and an increase in signal was observed. Like the work with DinG and XPD, this increase was attributed to a conformational change associated with ATP hydrolysis that increased the coupling of the 4Fe4S cluster to the DNA.

These results from Dna2 were exciting and we wanted to confirm the integrity of our DNA-modified electrodes before moving forward with the investigation. The following report describes the discovery that the electrodes prepared for experiments with Dna2 did not contain adequate DNA monolayers, possibly due to the use of commercial DNA. Characterization of the putative DNA-modified electrodes revealed that there was very little DNA on the electrode. Further experiments revealed that the electrochemical signal from Dna2 and EndoIII on these electrodes is not due to 4Fe-4S cluster redox activity and the signal is not mediated by DNA CT. These control experiments reveal a DNA-independent interpretation of the redox activity observed from 4Fe-4S cluster proteins on gold electrodes arising from Fe-EDTA complexes formed from 4Fe-4S cluster degradation.

3.2 Methods

Preparation of DNA substrates for DNA-modified Electrochemistry of yeast Dna2 and Dna2 E675A [14]

All standard or modified phosphoramidites and DNA synthesis reagents were purchased from Glen Research. DNA substrates were either purchased from Integrated DNA Technologies Inc. or synthesized on an Applied Biosystems 3400 DNA synthesizer. DNA sequences for electrochemistry experiments of Dna2 and EndoIII are shown in Table 3.1 below. Single-stranded DNA was purified using standard procedures: high pressure liquid chromatography (HPLC) using a reverse-phase PLRP-S column (Agilent) was used and oligonucleotide mass was confirmed using MALDI-TOF mass spectrometry. Thiol-modified strands were reduced after initial HPLC purification with 100 mM dithiothreitol (Sigma) for 2 hours and purified by size exclusion chromatography (Nap5 Sephadex G-25, GE Healthcare) followed by reverse-phase HPLC. The solvent was removed in vacuo and the strands were purified with HPLC. All single-stranded oligonucleotides were desalted

using ethanol precipitation and stored in a low salt buffer (5 mM phosphate, 50 mM NaCl, pH 7). Quantification of single-stranded oligonucleotides was performed by UV Vis and solutions of equimolar concentration of complementary strands were prepared. The well matched duplex solution contains the 36mer thiol strand with the 45mer complement strand with 9mer 5' overhang and the abasic site duplex solution contains the 36mer thiol strand and the 45mer strand with an abasic site and a 9mer 5' overhang. These solutions were deoxygenated by bubbling argon gas through the solution for 90 sec and duplex DNA was annealed on a thermocycler (Beckman Instruments) by initial heating to 90 °C, followed by slow cooling to 4 °C over 90 minutes. DNA was quantified using absorbance at 260 nm with extinction coefficients provided by Integrated DNA Technologies' online OligoAnalyzer tool.

Table 3.1: Sequences of DNA Substrates used for DNA-modified electrochemistry

DNA strand	Sequence (5' – 3')
A. 36mer thiol	SH – GAG GTG TTC ATG TAG TTG ACG CAG GAC GGG TTC AGT
B. Well matched complement with 9 nt overhang	AGC TCT GGA ACT GAA CCC GTC CTG CGT CAA CTA CAT GAA CAC CTC
C. 45mer complement with abasic site (9nt overhang)	AGC TCT GGA ACT GAA CCC GTC CTG CGT CAA CTA CAa bAA CAC CTC

DNA-modified Electrochemistry of yeast Dna2 and Dna2 E675A [12]

A multiplex chip was cleaned using sonication in acetone and isopropyl alcohol. The chip was then dried using argon gas and ozone cleaned for 20 min at 20 mW using an Uvo brand ozone cleaner. The clean chip was assembled onto a polycarbonate holder with an acrylic clamp and Buna-N rubber gasket (also cleaned using sonication in isopropyl alcohol and milliQ water), with the four quadrants of the chip separated by the fastened gasket and clamp. The aforementioned duplex solutions (25 μM) were deposited in 20 μL volumes onto each quadrant of the multiplex chip. For experiments without a DNA monolayer, 20 μL of DNA storage buffer was deposited onto the chip. The chip was incubated in a humid chamber for 20 hours to allow for formation of a self-assembled DNA monolayer. DNA monolayers were washed with phosphate buffer (5 mM P_i, 50 mM NaCl, 5% glycerol, pH 7.0) and then backfilled with 1 mM 6-mercaptohexanol (Sigma) in phosphate buffer for 45 min. Monolayers were then washed 10 times per quadrant with phosphate buffer and then 5 times with the indicated protein buffer. For anaerobic studies, the chip was then transferred to the anaerobic chamber. Here, it was washed 5 times with degassed Dna2 SEC buffer that had been stored in the anaerobic chamber

overnight. Initial CV scans of the monolayers in Dna2 SEC buffer were performed to ensure monolayer formation on each electrode. Dna2 (purification described in chapter II) or EndoIII (purified as described in [24]) was thawed on ice in the cold room and buffer exchanged into the appropriate buffer (see text). The buffer was removed from the chip and 20 μL of the Dna2 or EndoIII sample was deposited onto each quadrant and the rest of the sample was deposited on the chip as bulk solution. For experiments where the quadrants are kept separate, no bulk Dna2/EndoIII sample is placed above the quadrants. The chip was connected to the multiplexer and the Ag/AgCl reference and Pt counter electrodes were placed in the solution. CV and Square Wave Voltammetry were performed.

Adding cofactors ATP and Mg^{2+} to Dna2 on DNA-modified electrodes

A 300 mM solution of premixed ATP (Sigma CAS # 34369-07-8) and MgCl_2 in degassed milliQ water was prepared in the glove bag. This solution was added to the chip to achieve the desired final concentration and CVs and square wave voltammograms were obtained. After the indicated time incubating with ATP, the chip was scanned by CV and Square Wave Voltammetry again. The above procedures were performed in the same way with addition of non-hydrolyzable ATP γ S to different quadrants.

Protein Film Electrochemistry of Dna2 [25]

All electrochemical experiments were performed on an edge-plane pyrolytic graphite electrode (Pine Research Instrumentation) with a geometric surface area of 0.196 cm^2 . To generate a rough surface suitable for protein binding, the electrode was abraded with 400 grit sandpaper and cleaned by sonication for 30 seconds each in ethanol and water. After sonication, the absence of electroactive impurities was verified by scanning in Dna2 SEC buffer (20 mM Tris, 0.5 M NaCl, 0.1 mM EDTA, pH 7.73). Single-walled carbon nanotubes (CNTs) were included in the formation of all thin films unless otherwise noted. Protein thin films were formed by first depositing 10 μL of CNTs (0.25 mg/mL in water) on the cleaned electrode surface. This layer was dried with an Argon stream. Then, 2 or 3 layers of 10 μL Dna2 (29 μM in Dna2 SEC buffer without glycerol) were deposited on the electrode with drying by Argon stream after each later. Finally, 10 μL of 5% Nafion (2X dilution in water) was deposited on the surface and dried by argon stream to prevent dispersal. After thin film formation, 50 μL of Dna2 SEC buffer was pipetted on top of the film and a Ag/AgCl reference in 3 M NaCl and Pt auxiliary electrode were submerged in the resulting droplet (reference and counter rinsed before submersion). Reduction potential, current, and charge measurements were then taken by cyclic voltammetry (CV), square wave voltammetry (SQWV), and differential pulse voltammetry (DPV); all experiments

were taken at ambient temperature (25 °C). Potentials were converted to NHE by adding 0.212 V to the value measured by Ag/AgCl. To prevent leakage of NaCl into the buffer and subsequent wandering of the reference potential, the glass frit of the electrode was immersed in a gel loading pipet tip containing 3 M NaCl with 4% dissolved agarose, and dried in this mix overnight.

3.3 Results

Electrochemical signals of 4Fe-4S cluster proteins on putative DNA-modified gold electrodes: Dna2 and EndoIII as examples

Prior to this investigation, Dna2 had been studied many times in our group using putative DNA-modified electrochemistry (Figure 3.1). A reversible signal was observed from Dna2 with a midpoint potential of about 90 mV vs. NHE. No signal was observed when cyclic voltammetry was performed on buffer solution with the same electrodes before addition of the 4Fe-4S cluster Dna2 sample (Figure 3.1, top box, grey line). As was customary in the Barton group, the signal from the Dna2 sample was attributed to the reduction and oxidation of the 4Fe-4S cluster of Dna2 through DNA-mediated charge transfer. It was concluded that when a sufficient potential was applied to the gold electrode, namely 90 mV vs. NHE, charge would pass from the electrode, through the π -stacked orbitals of DNA, to the DNA-bound 4Fe-4S cluster. As was reported for other DNA-binding proteins, it was concluded that the midpoint potential of Dna2 shifts negatively upon binding to DNA, supported by the fact that the midpoint potential of Dna2 in protein films on graphite electrodes (without DNA) was about 150 mV vs. NHE (Figure 3.1, bottom box).

After the observation that a redox signal could be observed from Dna2 on DNA-modified electrodes, we sought to investigate whether the signal would be affected by the addition of ATP, as is seen with the DNA helicases XPD and DinG [10]. Indeed, addition of ATP to Dna2 on DNA-modified electrode resulted in an increase in the peak intensity that continued over time (Figure 3.2). As was concluded with XPD and DinG, this increase was attributed to an increase in coupling of the 4Fe-4S cluster of Dna2 to the DNA substrate as a result of a conformational change associated with ATPase activity. This interpretation was significant because it would establish that we can observe DNA-helicase activity on a DNA-modified electrode.

Due to the significance of these observations, and the significance of the role of DNA in our interpretation of the results, we wanted to confirm that the electrodes used for these experiments had adequate DNA-monolayers. With the characterization outlined in the next section, we found that there was no DNA-monolayer on these electrodes. Thus, we

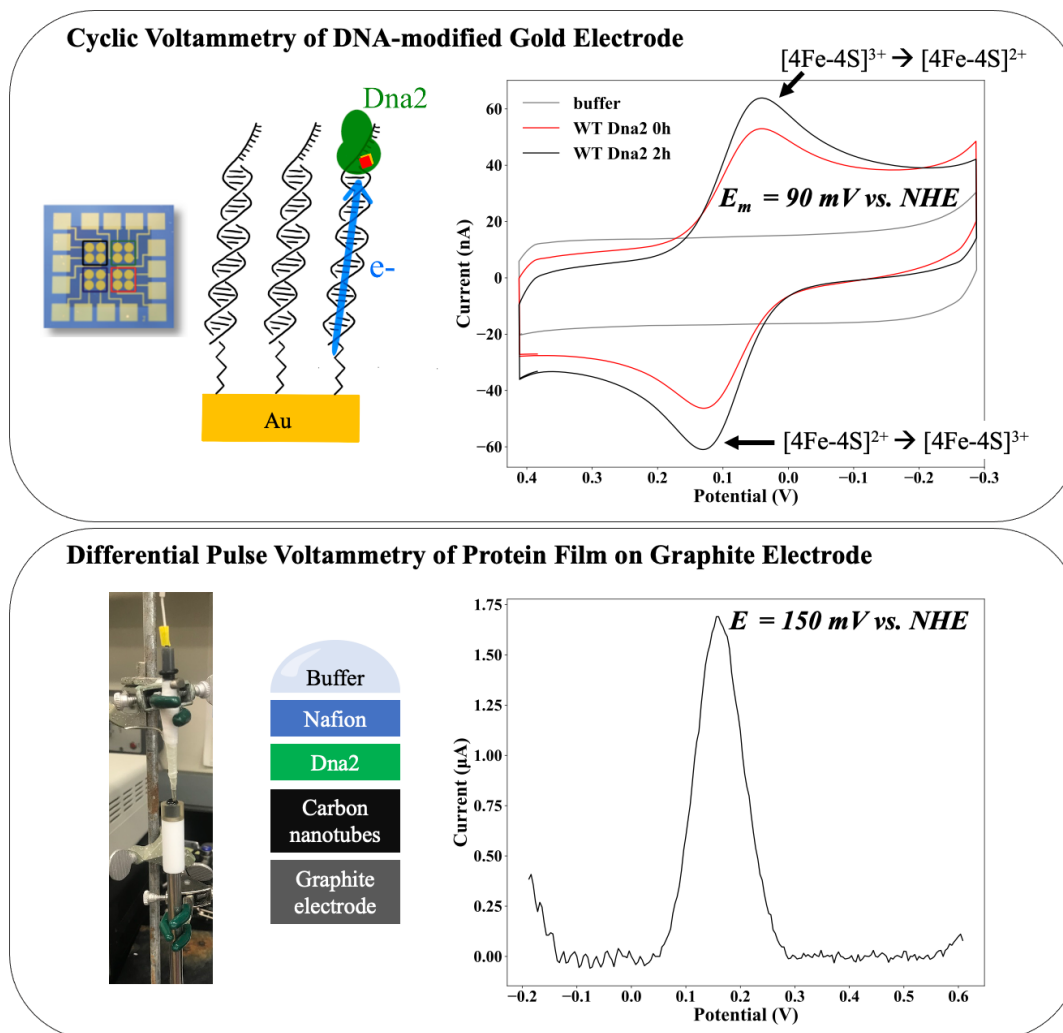


Figure 3.1: Dna2 was analyzed many times with putative DNA-modified electrochemistry on multiplexed gold electrodes (top box) prior to the onset of this work. Picture of multiplexed electrode (left) and cartoon of DNA-modified surface with Dna2 (green) bound to the DNA monolayer. CV of 14 μM Dna2 on putative DNA-modified electrode in Dna2 storage buffer (20 mM Tris, 0.5 M NaCl, 0.1 mM EDTA, 5% glycerol, pH 7.74) in anaerobic chamber shows a midpoint potential of about 90 mV vs. NHE. Scan rate: 100 mV/s, Ag/AgCl gel-tip reference electrode. Differential pulse voltammetry was performed on a protein film of Dna2 (bottom box) and shows a potential of 150 mV vs. NHE (buffer: 20 mM Tris, 0.5 M NaCl, 0.1 mM EDTA, pH 7.73).

sought to further investigate the source of the observed signals from the 4Fe-4S cluster proteins.

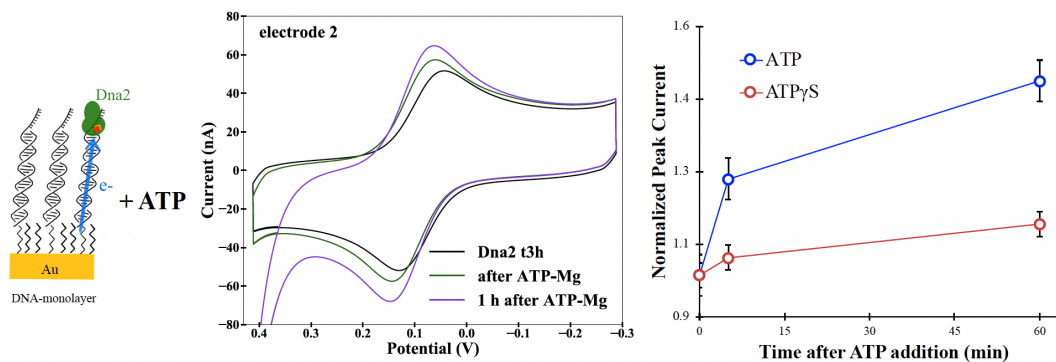


Figure 3.2: Cyclic Voltammograms of 6 μM Dna2 on putative DNA-modified gold electrode before and after addition of 5 mM ATP. Left panel shows quantification of reductive peak current normalized to the peak current before addition of ATP (error bars from four electrodes). All CVs performed anaerobically in Dna2 storage buffer (20 mM Tris, 0.5 M NaCl, 0.1 mM EDTA, 5% glycerol, pH 7.74) at 100 mV/s with Ag/AgCl gel-tip reference electrode.

Electrode characterization: DNA monolayers on gold electrodes contain considerably less DNA than originally reported

With the goal of supporting the interpretation that the electrochemical signal from Dna2 and EndoIII was due to the DNA-modified redox activity of the 4Fe-4S cluster, we sought to characterize the integrity of the DNA-monolayer on our electrodes. Potassium ferricyanide is used to measure the passivation of the electrode surface and ruthenium hexamine can be used to quantify the amount of DNA on the surface [26]. If the electrode surface is well passivated, with a DNA monolayer or β -MCH monolayer, then potassium ferricyanide will not be able to contact the electrode surface and there will be no signal observed in CV. If the surface is not well passivated, potassium ferricyanide will give a reversible signal in CV with a midpoint potential of about 200 mV vs. NHE. Ruthenium hexamine has been used in the Barton group to quantify the amount of DNA on the DNA-modified electrode. The positively-charged $[\text{Ru}(\text{NH}_3)_6]^{3+}$ can associate with the negatively-charged DNA strands and is reduced and oxidized during CV. The intensity of the signal is then used to quantify the number of DNA strands on the electrode.

When putative DNA-modified electrodes were treated with 150 μM $\text{K}_3\text{Fe}(\text{CN})_6$, a small irreversible reductive signal was observed at about 0 mV vs. NHE and the signal did not increase by adding a second aliquot so that the final concentration was 300 μM $\text{K}_3\text{Fe}(\text{CN})_6$ (Figure 3.3, top panel). The presence of a peak in the voltammogram indicates that the electrode surface was not entirely passivated; however, the peak was quite small, indicating that much of the $\text{K}_3\text{Fe}(\text{CN})_6$ was blocked from the electrode surface.

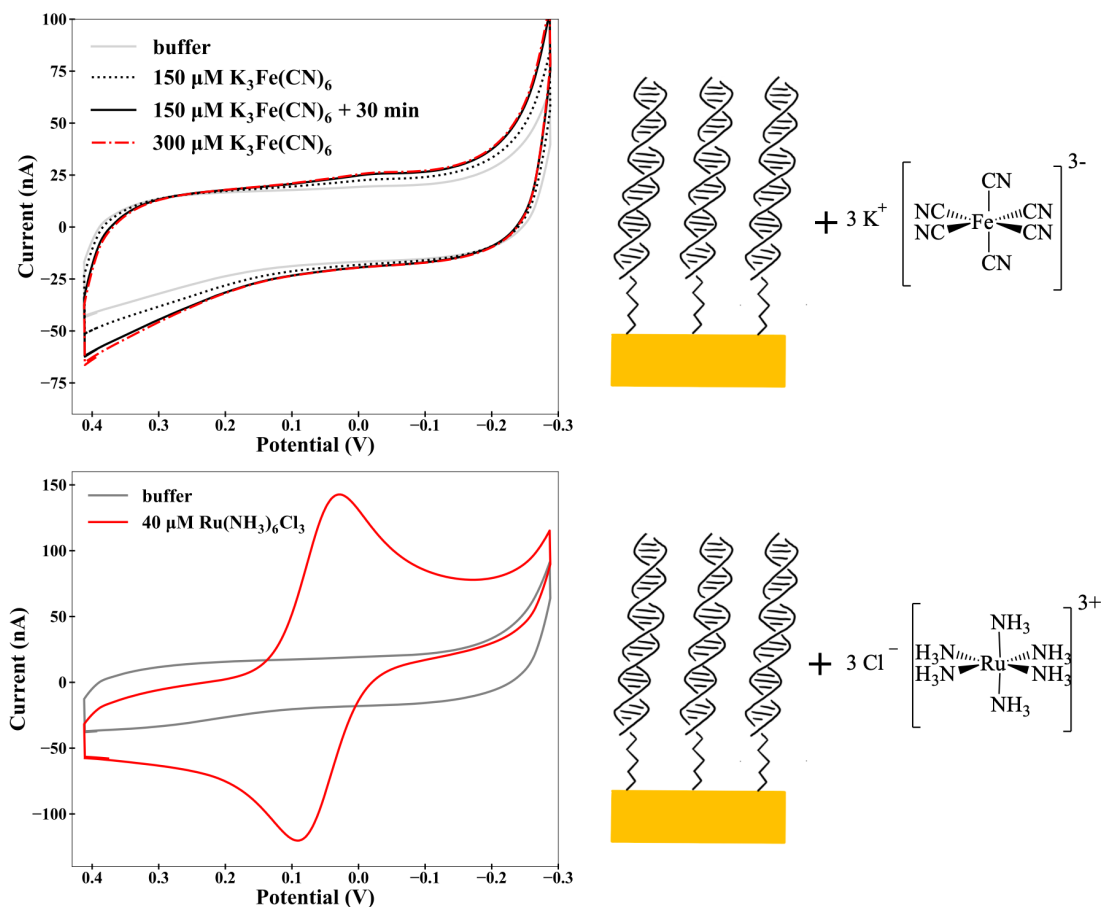


Figure 3.3: Characterization of putative DNA-monolayer with $[\text{Fe}(\text{CN})_6]^{3-}$ (top panel) and $[\text{Ru}(\text{NH}_3)_6]^{3+}$ (bottom panel). Cyclic voltammetry was performed on Tris buffer (20 mM Tris, 75 mM NaCl, pH 7.2) (gray trace, top panel). Then, $\text{K}_3\text{Fe}(\text{CN})_6$ was added directly to the electrode to a final concentration of 150 μM and CV was performed again (black dotted). CV was performed again after 1 hour (black solid) and again after another addition of $\text{K}_3\text{Fe}(\text{CN})_6$ to a final concentration of 300 μM (red dashed-dot). In another quadrant, cyclic voltammetry was performed on Tris buffer (20 mM Tris, 75 mM NaCl, pH 7.2) (gray trace, bottom panel). Then $\text{Cl}_3 \text{Ru}(\text{NH}_3)_6$ was added to a final concentration of 40 μM . A clear reversible signal was observed with a midpoint potential of about 60 mV vs. NHE. All CVs performed anaerobically at 100 mV/s with Ag/AgCl gel-tip reference electrode.

When DNA-modified electrodes were treated with 40 μM $[\text{Ru}(\text{NH}_3)_6]^{3+}$, a clear reversible signal was observed with a midpoint potential of 62 mV vs. NHE (Figure 3.3, bottom panel). Yu et al.[27] report a comparison of the cyclic voltammograms of $[\text{Ru}(\text{NH}_3)_6]^{3+}$ on bare gold electrodes vs. DNA-modified electrodes. On bare gold, $[\text{Ru}(\text{NH}_3)_6]^{3+}$ shows a reversible signal with a midpoint potential of about 40 mV vs. NHE. On DNA-modified

electrodes, there is also a reversible signal; however, the peak separation is smaller and the midpoint is at about -63 mV vs. NHE. The signal that we observed in our experiments is more similar to the bare-gold signal reported by Yu et al. from $[\text{Ru}(\text{NH}_3)_6]^{3+}$. Therefore, our observed signal from $[\text{Ru}(\text{NH}_3)_6]^{3+}$ is likely due to direct electron transfer at the electrode surface and is not DNA-mediated. Scan rate dependence analysis showed that the signal is diffusion-controlled, which agrees with the previous result that the ruthenium is diffusing to the electrode surface and making direct contact to be reduced/oxidized.

On the same multiplexed chip that was used for the previous two experiments with $\text{K}_3\text{Fe}(\text{CN})_6$ and $[\text{Ru}(\text{NH}_3)_6]^{3+}$, 17 μM EndoIII was added. EDTA was suggested to be a possible source of overlapping signals in CV, so EndoIII was buffer exchanged to remove EDTA before deposition on the electrode. No peaks were observed in the cyclic voltammogram initially (Figure 3.4). A small irreversible reductive signal at about -15 mV vs. NHE was observed from 17 μM EndoIII after one hour. No oxidative signal was observed. This signal looks very similar to that which was observed in the quadrant that was treated with $\text{K}_3\text{Fe}(\text{CN})_6$ (Figure 3.3, top panel). It is unclear whether this peak is due to the reduction of the 4Fe-4S cluster of EndoIII or some other contaminant in the solution. Compared to the signal from 13 μM EndoIII with EDTA (see Section VI, Figures 3.13 & 3.14) and the published CVs of EndoIII on DNA-modified electrodes, this signal is extremely small and not reversible. The absence of signal from EndoIII without EDTA supports the possibility that EDTA could be a source of the reversible signal from EndoIII on DNA-modified electrodes.

Because the signal from the CV of $[\text{Ru}(\text{NH}_3)_6]^{3+}$ suggested that $[\text{Ru}(\text{NH}_3)_6]^{3+}$ was being directly reduced and oxidized on the gold electrode surface, this technique could not be used to quantify the amount of DNA in the DNA-monolayer. Therefore, the density of the DNA-monolayer was determined with the use of radiolabeled DNA. A DNA-modified gold electrode was prepared using the established protocol with a ^{32}P label on the 5' end of the non-thiolated DNA strand of the DNA-monolayer substrate. The prepared chip was then analyzed with the scintillation counter revealing that there was 0.87 pmoles of DNA per cm^2 electrode, which would cover about 20% of the electrode surface. This disagrees with previous publications from the Barton group that report 40 pmol/cm^2 DNA-coverage on DNA-modified gold electrodes that were prepared in the same way [25]. Interestingly, the scintillation counter showed 20 times as many counts from the rubber gasket as the electrode itself. Therefore, thiol-modified DNA was absorbed by the rubber gasket during the incubation period causing a very low-density DNA-monolayer. Similar results were observed when the chip was backfilled for 20 minutes or 40 minutes with 0.5 mM MCH.

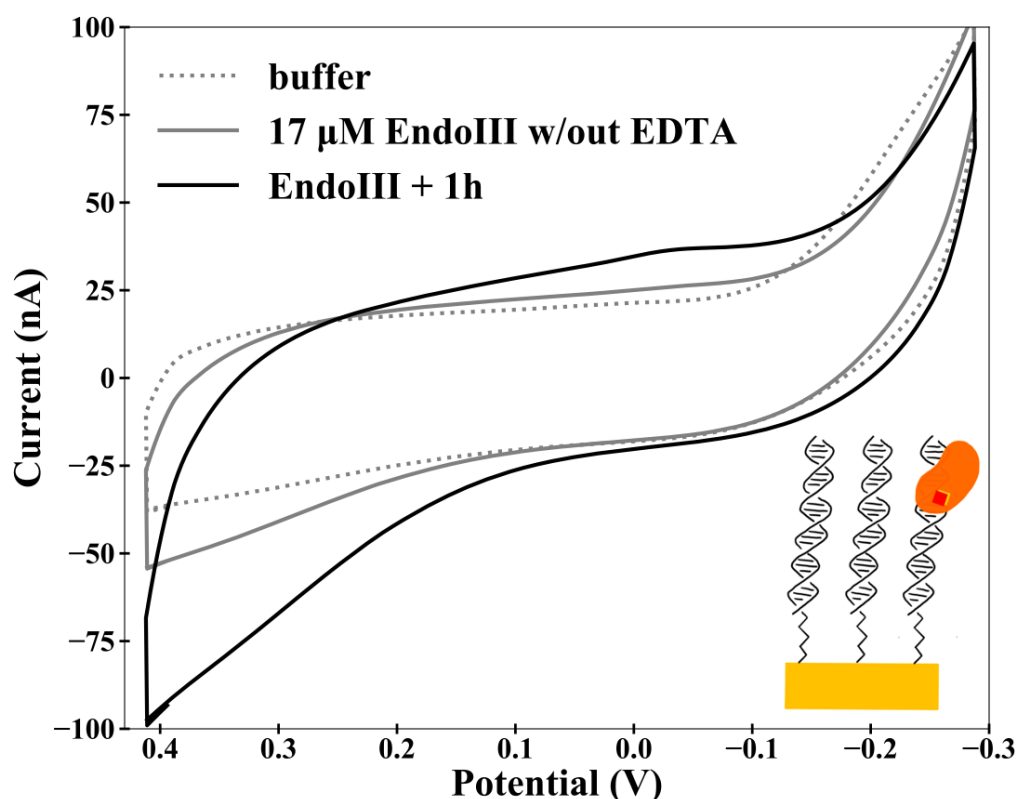


Figure 3.4: Cyclic voltammogram of EndoIII (17 μM) on putative DNA-modified gold electrode. EndoIII was added to the same multiplexed electrode chip used in Figure 14 to a separate quadrant and CV was performed (gray solid). CV was performed one hour later (black solid). Buffer scan performed before addition of EndoIII (grey dotted). Inset: schematic of DNA-modified electrode with EndoIII bound to the DNA-monolayer. No reversible signal observed from EndoIII in cyclic voltammograms. All CVs performed anaerobically at 100 mV/s with Ag/AgCl gel-tip reference electrode.

The scintillation counter could not detect any counts from the chip that was assembled with DNA that was not radiolabeled. The low density of DNA on the putative DNA-monolayer raises the question of the source of the previously observed signals from DNA-binding 4Fe-4S cluster proteins (Dna2 and EndoIII). With very little DNA on the surface, it is unlikely that the signal was due to DNA mediated charge transfer from the electrode to the 4Fe-4S cluster of the DNA-bound protein. Therefore, we sought to investigate possible other sources of this signal. For the rest of this report, the electrodes that were prepared by incubation with thiol modified DNA with the goal of generating a DNA monolayer will be referred to as “putative DNA-modified electrodes” because it is likely that they have a very incomplete or no DNA monolayer.

Electrochemical signals of 4Fe-4S cluster proteins on gold electrodes are not specific to DNA

To start, an electrode was prepared without a DNA monolayer. The multiplexed gold electrode was prepared using the established protocol that had been employed for many previous studies with Dna2 and other 4Fe-4S cluster proteins investigated in the Barton group [13, 26, 28]. However, instead of incubating the gold electrode surface overnight in a thiol-modified DNA duplex solution, the electrode was incubated in DNA-storage buffer. The rest of the electrode preparation was kept exactly the same, including the backfilling with MCH. Therefore, the resulting electrode contained a monolayer of MCH on the multiplexed gold electrode chip.

In cyclic voltammograms of 6 μM Dna2 on the aforementioned MCH-monolayer gold electrode, a clear reversible signal was observed with a midpoint potential of about 90 mV vs. NHE (Figure 3.5). This signal is nearly identical to those observed from Dna2 on the putative DNA-modified electrodes used in Section II. This was unexpected because it was believed that the signal that had been previously observed from Dna2 was due to a DNA-mediated charge transfer between the electrode and the 4Fe-4S cluster. Although a direct reduction and oxidation of the 4Fe-4S cluster was thought to be possible between the gold electrode and the 4Fe-4S cluster, this signal was supposedly avoided by the passivation of the gold surface with MCH. Furthermore, the midpoint potential of 90 mV vs. NHE directly contradicted the proposed shift in oxidation potential upon DNA-binding [29]. This control experiment indicates that the observed Dna2 electrochemical signal is not caused by a DNA-mediated process.

On the putative DNA-modified electrodes described in Section II, an increase in peak intensity was observed following addition of ATP to Dna2 on the electrode surface (Figure 3.2). After observing that Dna2 showed a reversible signal on gold electrodes with a MCH monolayer that was very similar to the signal on the putative DNA-modified electrodes, we next investigated whether the increase in peak intensity upon addition of ATP was also observed on gold electrodes with a MCH monolayer. Indeed, upon addition of ATP to Dna2 on gold electrodes without a DNA monolayer, there was an increase in the peak intensity of the reversible signal (Figure 3.6). This change in signal was comparable to that seen on the putative DNA-modified electrodes. Therefore, the conclusion that the increase in signal with ATP hydrolysis is due to a change in the coupling of the 4Fe-4S cluster to the DNA is not supported. On the same electrode, in a separate quadrant, buffer was added instead of ATP and no significant increase was observed.

In this experiment, Dna2 was not added to two of the quadrants of the MCH-modified

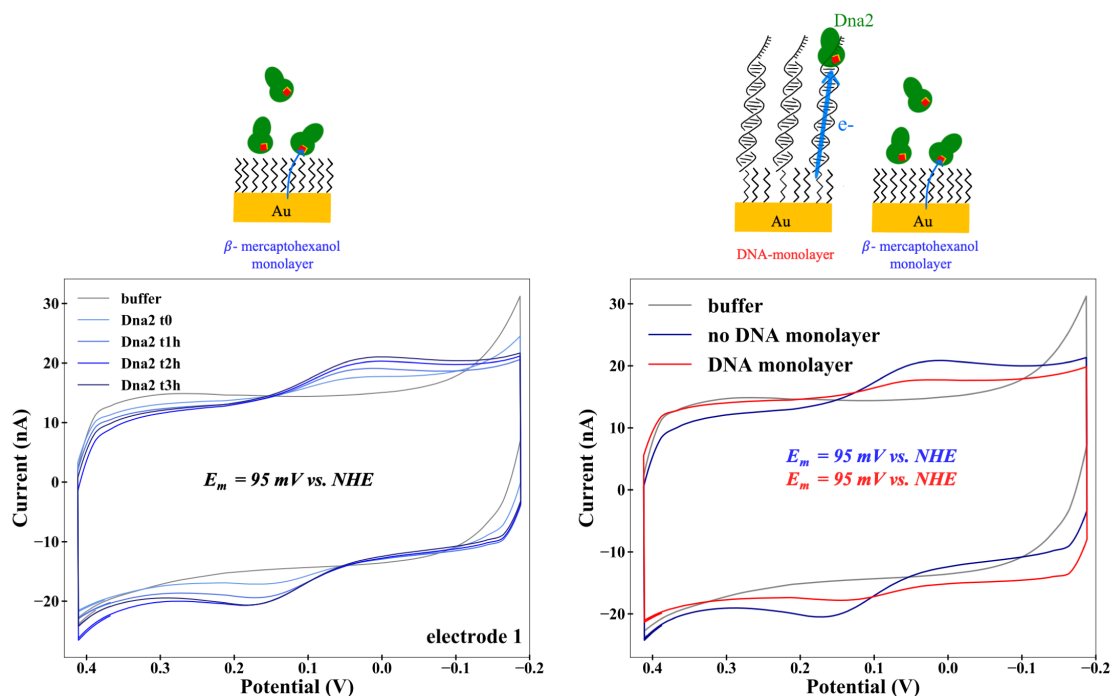


Figure 3.5: Cyclic Voltammograms of 6 μM Dna2 on multiplexed gold electrodes with beta-mercaptohexanol monolayer (left). Signal with midpoint potential of about 95 mV vs. NHE is apparent immediately (light blue) and increases over time. Right panel shows overlay of CV of Dna2 on multiplexed gold electrodes with beta-mercaptohexanol monolayer (blue) with CV of Dna2 on a putative DNA-modified gold electrode surface (red). Both CVs show a reversible signal with a midpoint potential of about 95 mV vs. NHE. All CVs performed anaerobically in Dna2 storage buffer (20 mM Tris, 0.5 M NaCl, 0.1 mM EDTA, 5% glycerol, pH 7.74) at 100 mV/s with Ag/AgCl gel-tip reference electrode.

electrode. Instead, these quadrants were filled with Dna2 storage buffer (30 μL) and CVs of these quadrants showed no observable peaks. ATP was also added to one of the quadrants without Dna2 and a small reversible signal appeared with a midpoint potential of about 110 mV vs. NHE (Figure 3.7). The redox active moiety responsible for this signal is unclear. It is known that ATP binds iron with a formation constant of 10^{29} at pH 7, which could form a possibly redox active Fe-ATP complex [30, 31]. Although there was no 4Fe-4S Dna2 or other iron species deposited into this quadrant, there could be trace iron in the solution or contamination from the electrode surface that forms a redox active complex with interaction with ATP.

Following the observations that a signal could be observed from Dna2 without a DNA-monolayer, we wanted to investigate the effect of the MCH monolayer on the electrochemistry of Dna2. A multiplexed gold electrode was prepared using the established protocol,

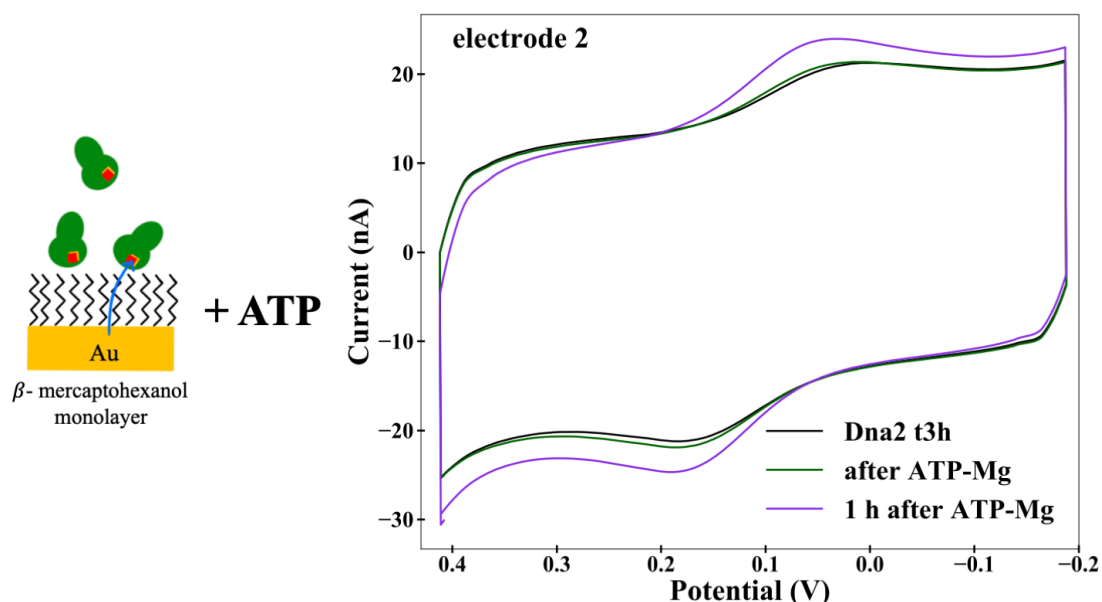


Figure 3.6: Cyclic Voltammograms of 6 μM Dna2 on multiplexed gold electrodes with β -mercaptohexanol monolayer before (black), after (green), and 1 hour after (purple) addition of 5 mM ATP. Black trace is signal from Dna2 after 3 h (same as Figure 2, left, 3h time point). Green trace is CV after 5 mM ATP added. Purple trace is CV performed 1 hour later. An increase in the peak intensity is observed with addition of ATP over time. Compare to Figure 2 on DNA-modified electrodes. All CVs performed anaerobically in Dna2 storage buffer (20 mM Tris, 0.5 M NaCl, 0.1 mM EDTA, 5% glycerol, pH 7.74) at 100 mV/s with Ag/AgCl gel-tip reference electrode.

except that it was incubated with DNA storage buffer overnight instead of thiol-modified DNA. Then, half of the quadrants were back-filled with MCH for 45 minutes to form a monolayer and the other two quadrants were incubated with buffer during that time. This electrode was then thoroughly washed according to the established protocol and used for electrochemistry of Dna2. First, Dna2 buffer was placed on the electrode and CV was performed. The capacitance of all electrodes on the chip were the same, revealing that the presence of the MCH monolayer did not affect the capacitance of the electrodes. Upon treatment with a 2.3 μM solution of Dna2, a reversible signal was observed with a midpoint potential of about 90 mV vs. NHE in all quadrants (Figure 3.8). This signal was very similar to that which was observed from the 6 μM solution of Dna2 on the MCH-modified electrode, however the intensity of the signal was smaller. This was probably due to a lower concentration of 4Fe-4S cluster. An increase in peak intensity was observed on all electrodes upon addition of ATP. Therefore, whether the gold electrode is bare or has a MCH monolayer does not affect the reversible signal observed from Dna2 or the increase

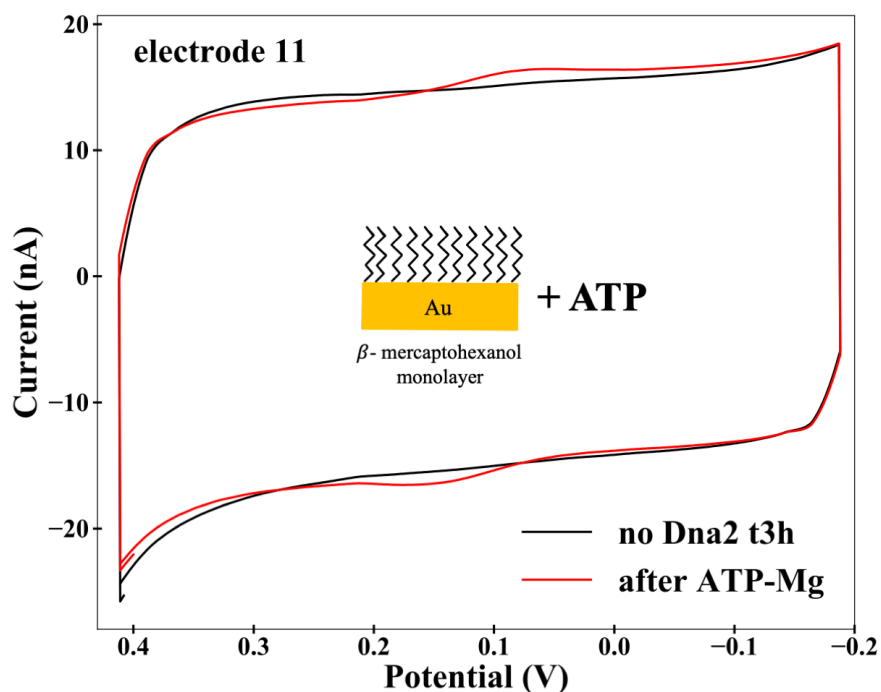


Figure 3.7: Addition of ATP to buffer on multiplexed gold electrode with β -mercaptohexanol monolayer. CV of Dna2 storage buffer before (black) and after (red) addition of 5 mM ATP on multiplexed gold electrode with β -mercaptohexanol monolayer. Reversible signal observed with a midpoint potential of about 110 mV vs. NHE. CVs performed anaerobically at 100 mV/s with Ag/AgCl reference electrode with gel tip.

in peak intensity upon addition of ATP.

When the above protein solution was removed from the electrode, it was analyzed by UV Vis (Figure 3.9). There was a change in the spectra before and after addition to the electrode. After electrochemistry, a pronounced shoulder appeared at 300-350 nm. The Fe(III)-EDTA complex as well as the 3Fe-4S cluster (a degradation product of 4Fe-4S clusters) absorb in this range and could be the source of this shoulder [32–35]. There was also a large increase between 200 and 300 nm which is likely due to ATP, which has an absorption maximum at 260 nm (extinction coefficient = $15.4 \times 10^3 \text{ M}^{-1} \text{ cm}^{-1}$). After Dna2 was removed, the electrode was washed extensively with Dna2 storage buffer and CV was performed in Dna2 storage buffer, which showed no observable peaks. Then a 5 mM solution of ATP and MgCl_2 was added to the electrode. A reversible signal was observed with a midpoint potential of about 125 mV vs. NHE. This signal was very small immediately, but increased significantly after 90 minutes. This is consistent to what was observed with the previous electrode, ATP-Mg on the electrode can cause a reversible

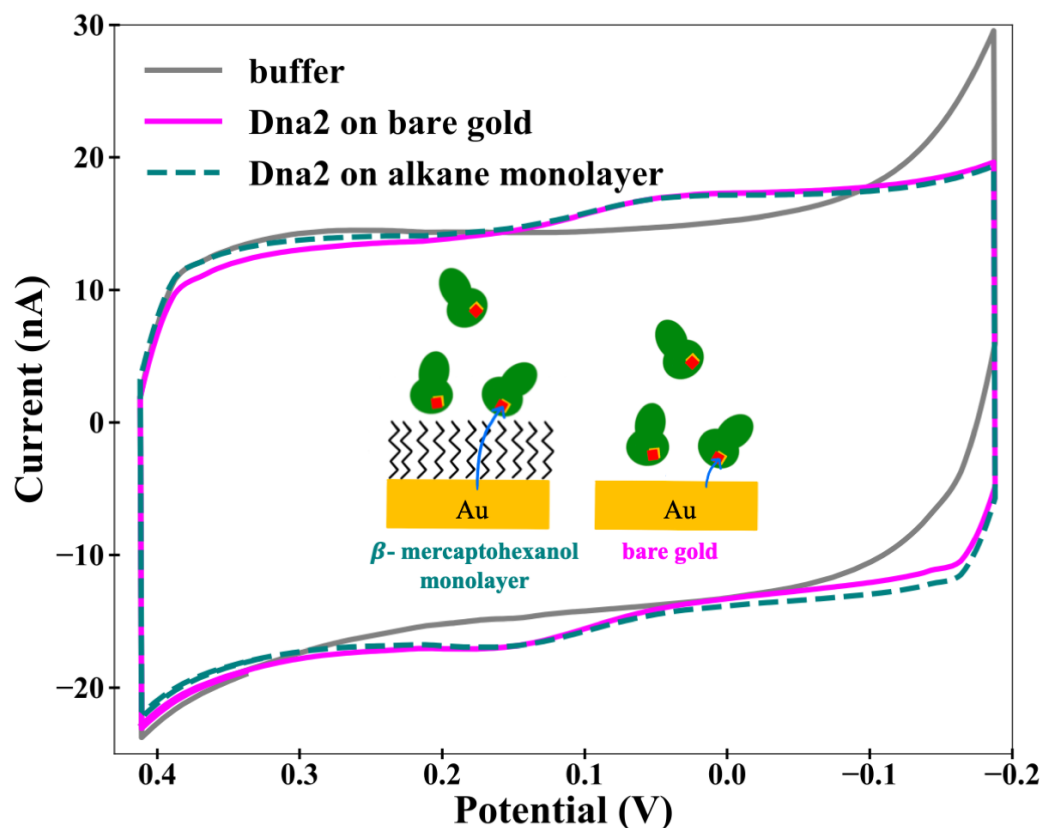


Figure 3.8: CVs of Dna2 on gold electrode with β -mercaptohexanol monolayer and on bare gold electrodes. CV of 2.3 μ M Dna2 on gold electrode with β -mercaptohexanol monolayer (teal) and bare gold electrode (pink). Bare gold and β -mercaptohexanol monolayer were on the same multiplexed chips in different quadrants. Identical reversible signal observed with a midpoint potential of about 90 mV vs. NHE on both types of electrode surface. All CVs performed anaerobically in Dna2 storage buffer (20 mM Tris, 0.5 M NaCl, 0.1 mM EDTA, 5% glycerol, pH 7.74) at 100 mV/s with Ag/AgCl gel-tip reference electrode.

redox signal without the presence of 4Fe-4S protein.

The above results contradict the conclusions regarding the analysis of the redox activity of 4Fe-4S cluster proteins by putative DNA-modified electrochemistry as described in Section II. The experiments in Section II report a reversible signal from the 4Fe-4S cluster with a midpoint potential in the range of 80-100 mV vs. NHE. This signal has been attributed to the DNA-mediated reduction and oxidation of the 4Fe-4S cluster of the protein while it is bound to the putative DNA-monolayer on the electrode. The observations reported in this section, that an identical signal can be observed without the presence of a DNA-monolayer, show that the previously reported signals can not be unequivocally assigned

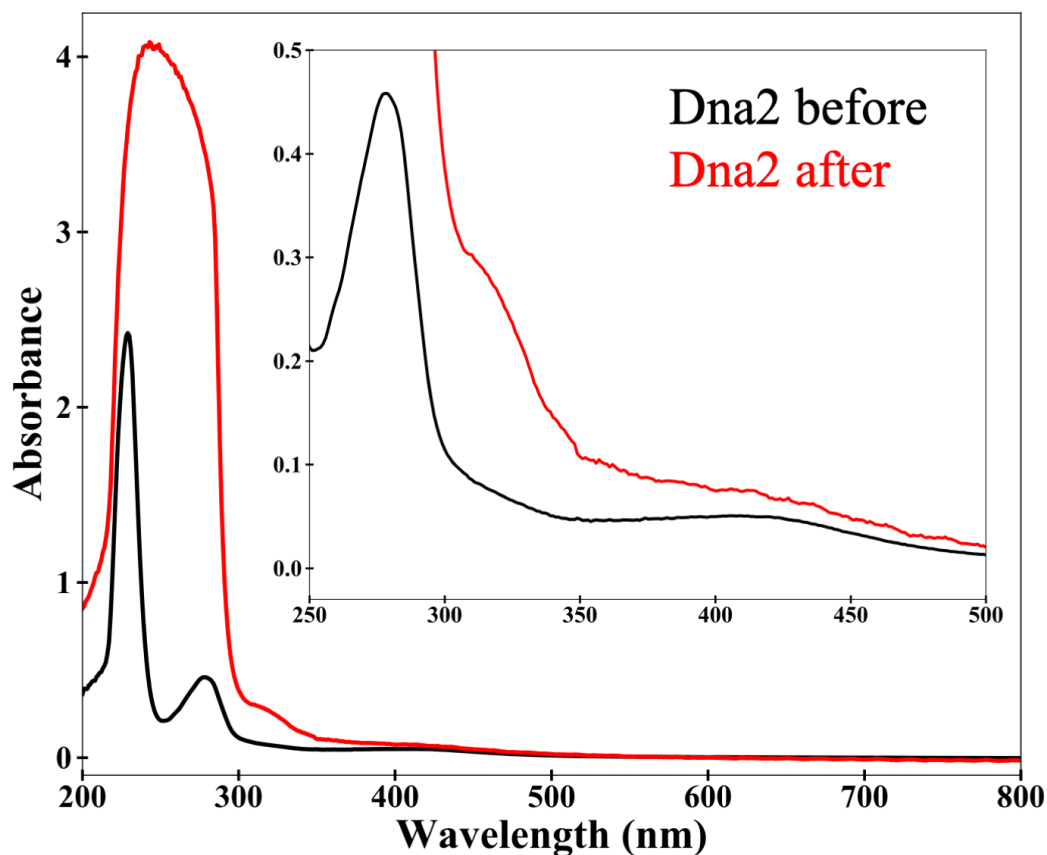


Figure 3.9: UV Vis Spectra of Dna2 before and after putative DNA-modified Electrochemistry. UV Vis of 2.3 μM Dna2 before (black) and after (red) analysis on putative DNA-modified electrodes. After electrochemistry (Figure 5), Dna2 solution was pipetted off of the electrode and analyzed with UV-Vis (red). Spectra shows characteristic 410 nm absorbance of 4Fe-4S cluster. Saturating absorbance at 200-300 nm likely from the 5 mM ATP added to solution during electrochemistry experiment.

to DNA-mediated redox activity. The 4Fe-4S cluster of the protein, or some other redox active species in solution, is able to be reduced or oxidized at the electrode without charge transfer through the DNA bases. Furthermore, previous work on Dna2 showed that the midpoint potential of the 4Fe-4S cluster of DNA-binding proteins shifts with binding to DNA. This conclusion was made by comparing the midpoint potential of Dna2 proteins on graphite electrodes (> 150 mV vs. NHE) vs. DNA-modified gold electrodes (90-100 mV vs. NHE). The above results show that Dna2 had a midpoint potential characteristic of the “DNA bound” species, even though there was no DNA in solution. Finally, the above control experiments establish that ATP-Mg can cause a reversible signal in CV in the absence of 4Fe-4S cluster protein, contradicting the previous conclusion that addition

of ATP causes a conformational change in the protein that increases the coupling of the 4Fe-4S cluster to the DNA.

These control experiments led us to investigate whether there was a redox active species in the solution other than the 4Fe-4S cluster protein that was causing the reversible signal in the CV. Looking to the literature, we found that a complex of Fe-EDTA was found to have a midpoint potential of about 90 mV vs. NHE in CVs at pH 8 [36]. The Dna2 storage buffer, and the buffers used to perform DNA-modified electrochemistry on other 4Fe-4S cluster proteins in the Barton group, contain EDTA in concentrations of 0.1 – 1 mM. Additionally, it is known that the 4Fe-4S cluster can be unstable and degrade (which could be exacerbated by the interaction with the electrode surface [37]), releasing iron into the solution. Therefore, it is highly likely that Fe-EDTA forms in our protein solutions. To determine whether this species was responsible for the observed signal, we sought to investigate the redox activity of Fe-EDTA complexes on our DNA-modified electrochemistry set up.

Electrochemical signals of 4Fe-4S cluster proteins are identical to electrochemical signals arising from Fe-EDTA

As mentioned above, we wanted to investigate the redox activity of Fe-EDTA complexes on our DNA-modified electrodes to observe how they compared to the signals that were previously attributed to 4Fe-4S cluster proteins. Putative DNA-modified multiplexed gold electrodes were prepared using the established protocol (2 quadrants with DNA-monolayer, and 2 quadrants without DNA-monolayer) and a variety of Fe-EDTA species were deposited on the surface and analyzed by cyclic and square wave voltammetry. First, Fe(II) sulphate heptahydrate (2.5 μ M) in HEPES buffer (20 mM HEPES, 0.5 M NaCl, 5% glycerol, pH 7.75) was deposited onto the electrode surface. An irreversible reductive peak was observed in CV at -100 mV vs. NHE (Figure 3.10, black trace). In the first scan there was also a oxidative wave at 190 mV vs. NHE; however, this was not apparent in any future scans. Then, EDTA was added directly to this electrode to a final concentration of 2.5 μ M. This caused a large increase in the irreversible peak at -100 mV vs. NHE in CVs (Figure 3.10, light pink traced). After 30 minutes, CV was performed again and the signal at -100 mV vs. NHE was less intense. There was still an irreversible peak at 190 mV vs. NHE in the first scan of the CV. After 90 and 130 minutes, the irreversible peak at -100 mV vs. NHE was quite small and there was still a large peak in the first scan at 190 mV vs. NHE.

The next species that was investigated was a premixed solution of 2.5 μ M Fe-EDTA in

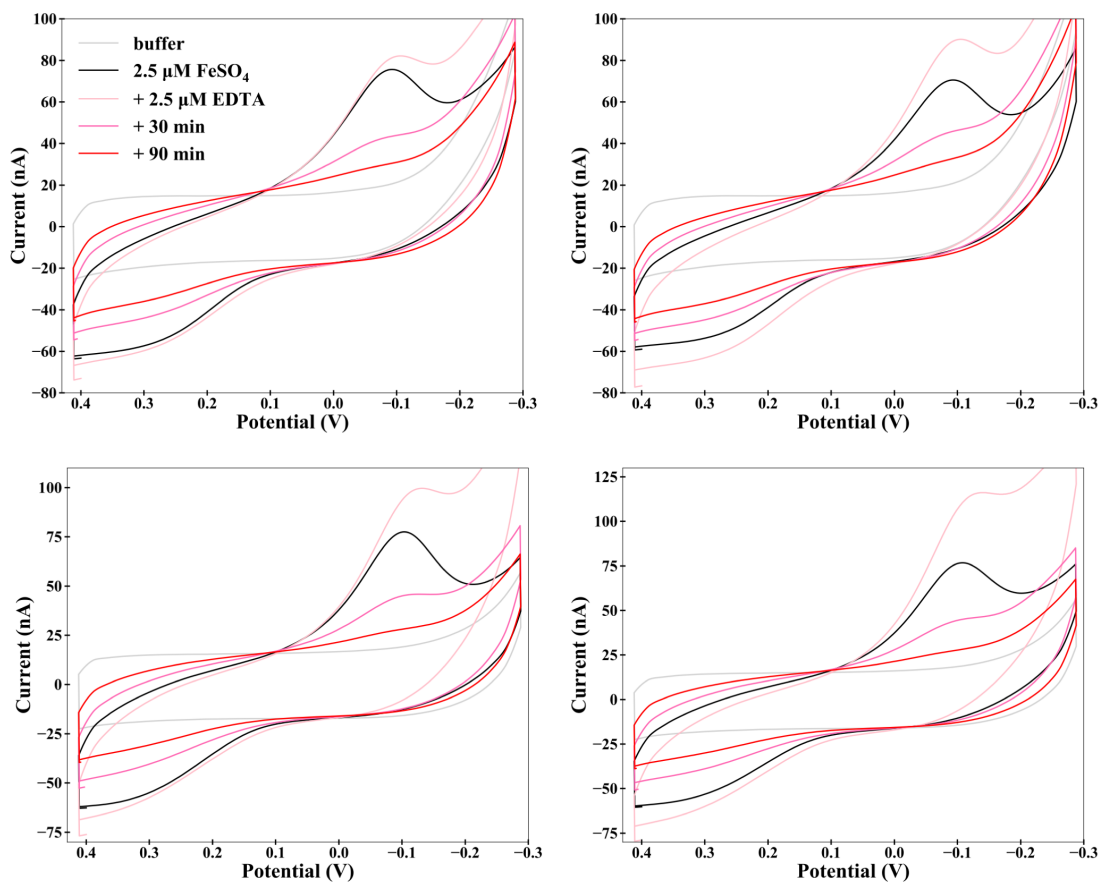


Figure 3.10: Fe^{2+} and EDTA mixed on putative DNA-modified electrode. Cyclic voltammetry of $2.5 \mu\text{M FeSO}_4$ on putative DNA-modified electrode (black). $2.5 \mu\text{M EDTA}$ was then added to the solution on the electrode and CV was performed (light pink). CV was then performed 30 min later (pink) and 90 min later (red). Irreversible reductive wave at about -100 mV vs. NHE apparent from FeSO_4 solution, which increases slightly with addition of EDTA and then decreases over time. Four panels show CVs from 4 representative electrodes of 16-electrode multiplexed chip. All CVs performed anaerobically in HEPES buffer (20 mM HEPES, 0.5 M NaCl, 5% glycerol, pH 7.74) at 100 mV/s with Ag/AgCl gel-tip reference electrode.

HEPES buffer. CVs of this species showed a small reversible signal with a midpoint potential of about 100 mV vs. NHE and an irreversible reductive peak at -100 mV vs. NHE (Figures 3.11 & A.1). Then, a premixed solution of $2.5 \mu\text{M Fe(II)Cl}_2$ was prepared in Tris buffer and analyzed by CV on the same DNA-modified electrode in a different quadrant (Figures 3.12 & A.2). This solution resulted in a reversible signal with a midpoint potential of about 90 mV vs. NHE and an irreversible peak at -100 mV vs. NHE . These signals persisted after 1 hour. At this point, EndoIII was added directly to the electrode (with the Fe-EDTA solution) to a final concentration of $20 \mu\text{M}$ (Figure 3.13).

A clear reversible signal was observed with a midpoint potential of 90 mV vs. NHE, identical to that of published reports of the DNA-modified electrochemistry of EndoIII [38]. This reversible signal overlapped with the reversible signal seen from the premixed solutions of Fe and EDTA in Tris and HEPES. This overlap was observed most clearly in the cathodic square wave voltammetry of both species (Figure 3.13). The reversible signal observed from Dna2 is also seen at this same midpoint potential of 100 mV vs. NHE (Figure 3.7).

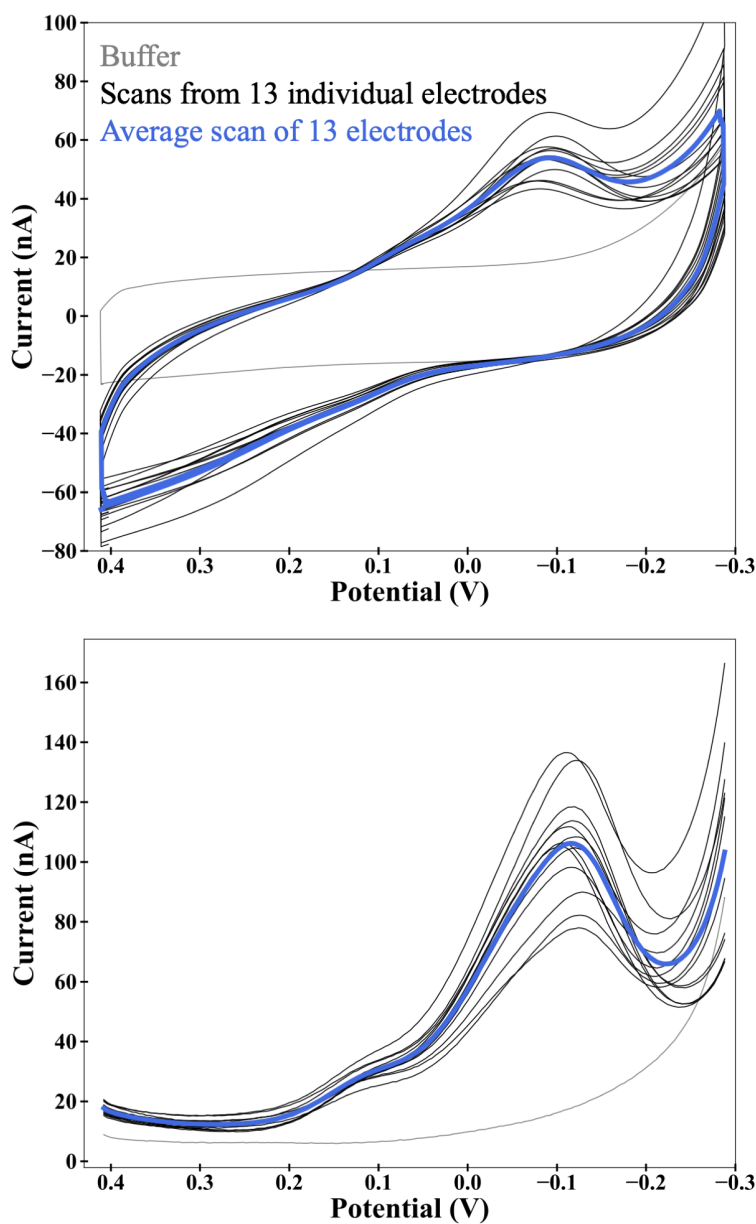


Figure 3.11: Cyclic Voltammetry of premixed solution of Fe^{2+} and EDTA on putative DNA-modified electrodes in HEPES buffer. Cyclic voltammetry (top) and cathodic square wave voltammetry (bottom) of $2.5 \mu\text{M}$ FeEDTA on putative DNA-modified electrodes. Black traces are CVs from 13 individual electrodes on one multiplexed electrode and blue trace is average of all 13 electrodes. Small reversible signal observed in CV and more clearly in square wave voltammetry with midpoint potential of about 90 mV vs. NHE. Irreversible reductive wave at about -100 mV vs. NHE apparent in both CV and square wave voltammograms. All voltammetry performed anaerobically in HEPES buffer (20 mM HEPES, 0.5 M NaCl, 5% glycerol, pH 7.74) at 100 mV/s (CVs) or 15 Hz (square wave voltammetry) with Ag/AgCl gel-tip reference electrode.

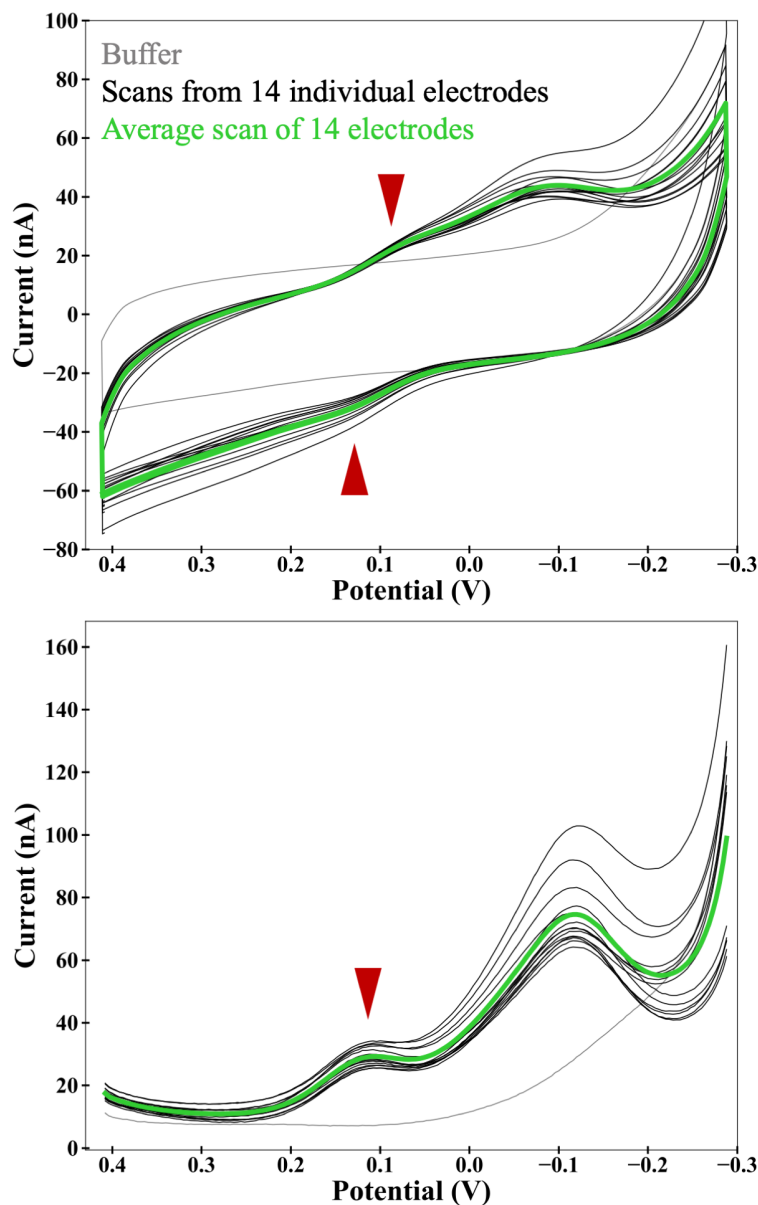


Figure 3.12: Cyclic Voltammetry of premixed solution of Fe^{2+} and EDTA on putative DNA-modified electrodes in Tris buffer. Cyclic voltammetry (top) and cathodic square wave voltammetry (bottom) of $2.5 \mu\text{M}$ FeEDTA on putative DNA-modified electrodes. Black traces are CVs from 14 individual electrodes on one multiplexed electrode and green trace is average of all 14 electrodes. Small reversible signal (red triangles) observed in CV and more clearly in square wave voltammetry with midpoint potential of about 90 mV vs. NHE. Irreversible reductive wave at about -100 mV vs. NHE apparent in both CV and square wave voltammograms. All voltammetry performed anaerobically in Tris buffer (20 mM Tris, 0.5 M NaCl, 5% glycerol, pH 7.74) at 100 mV/s (CVs) or 15 Hz (square wave voltammetry) with Ag/AgCl gel-tip reference electrode.

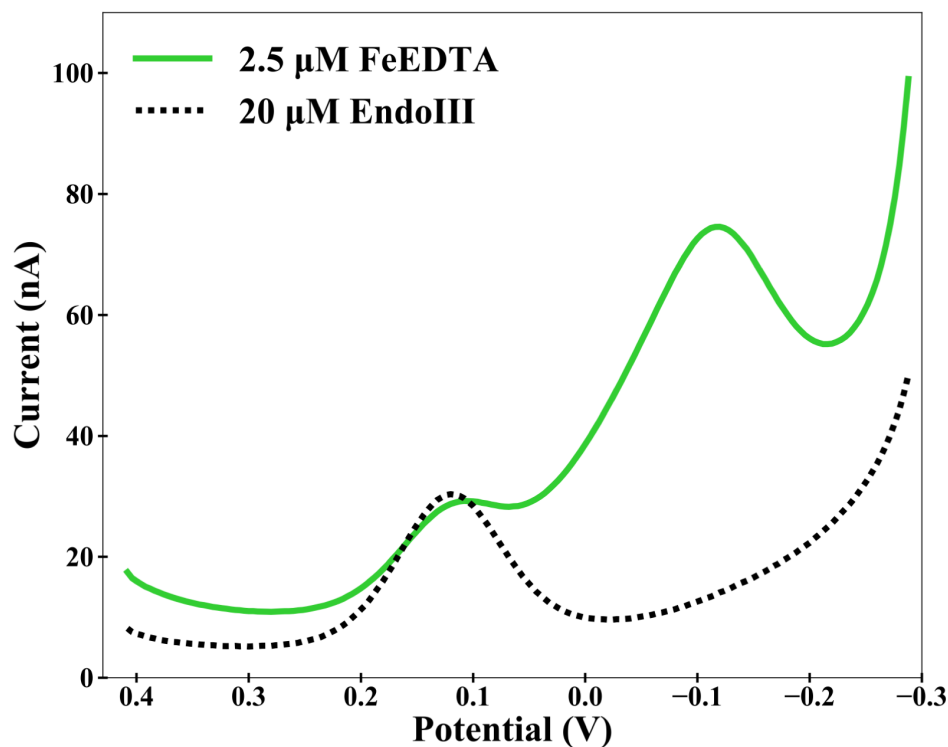


Figure 3.13: Square wave voltammetry of FeEDTA and EndoIII on putative DNA-modified electrodes. Square wave voltammograms of 2.5 μM FeEDTA (green) with addition of 20 μM EndoIII (black dotted) on putative DNA-modified electrodes. Peak from EndoIII solution overlaps with signal at 90 mV vs. NHE from FeEDTA solution. Traces are averages over 13 electrodes. Both solutions were analyzed with the same multiplexed electrode chip. All voltammetry performed anaerobically in Tris buffer (20 mM Tris, 0.5 M NaCl, 5% glycerol, pH 7.74) at 15 Hz with Ag/AgCl gel-tip reference electrode.

The investigation of Fe-EDTA species on our putative DNA-modified electrochemistry platform showed that the signal that we have observed from Dna2, and that has been published for many other 4Fe-4S clusters, is reproduced by adding Fe-EDTA to the electrode. There are two conclusions that follow. Either the previously observed signal is solely due to Fe-EDTA or is a combination of the signal from Fe-EDTA and the DNA-mediated signal from the 4Fe-4S cluster of the DNA-binding protein. The logical next step was to analyze the putative DNA-modified electrochemistry of 4Fe-4S cluster Dna2 (and other 4Fe-4S cluster DNA binding proteins) in the absence of EDTA.

Electrochemical signals of 4Fe-4S cluster proteins are not observed when EDTA is omitted from buffer solutions

To determine whether the previously observed and reported signal from DNA binding 4Fe-4S cluster proteins was solely due to Fe-EDTA in the solution, EDTA was omitted from buffer solutions and these proteins (Dna2 and EndoIII) were analyzed by putative DNA-modified electrochemistry using the established protocol. First, a 13 μM solution of EndoIII was analyzed on a multiplexed gold electrode, in one quadrant with a putative DNA-monolayer and one quadrant without a DNA-monolayer (Figure 3.14). In previous studies and reports, this concentration of 4Fe-4S cluster showed a clear reversible signal with peaks of about 13 nA and a midpoint potential of 80-100 mV vs. NHE. Without EDTA in the buffer, a very small reversible signal was observed with a midpoint potential of 100 mV vs. NHE. Although the small signal without EDTA would suggest that Fe-EDTA isn't the sole source of the reversible signals observed, this signal is considerably less intense than would be expected and what has been seen previously from this concentration of 4Fe-4S cluster protein. Therefore, this could be due to Fe-EDTA that persisted in solution after the buffer exchange out of buffer with 1 mM EDTA. EDTA was then added directly to this solution of EndoIII on the electrode surface to a final concentration of 0.5 mM. CV was then performed and a large reversible signal was observed with a midpoint potential of 100 mV vs. NHE (Figure 3.15 & 3.16). This signal is identical to what has been observed and published previously from solutions of this concentration of EndoIII on DNA-modified electrodes. This would suggest that addition of EDTA causes the formation of a redox-active species in solution, possibly by chelating free iron in the solution or chelating iron directly from the 4Fe-4S cluster of EndoIII and forming the redox-active Fe-EDTA complex. Identical results were observed whether the electrode surface had a putative DNA-monolayer or solely the MCH monolayer (Figure 3.15 & 3.16).

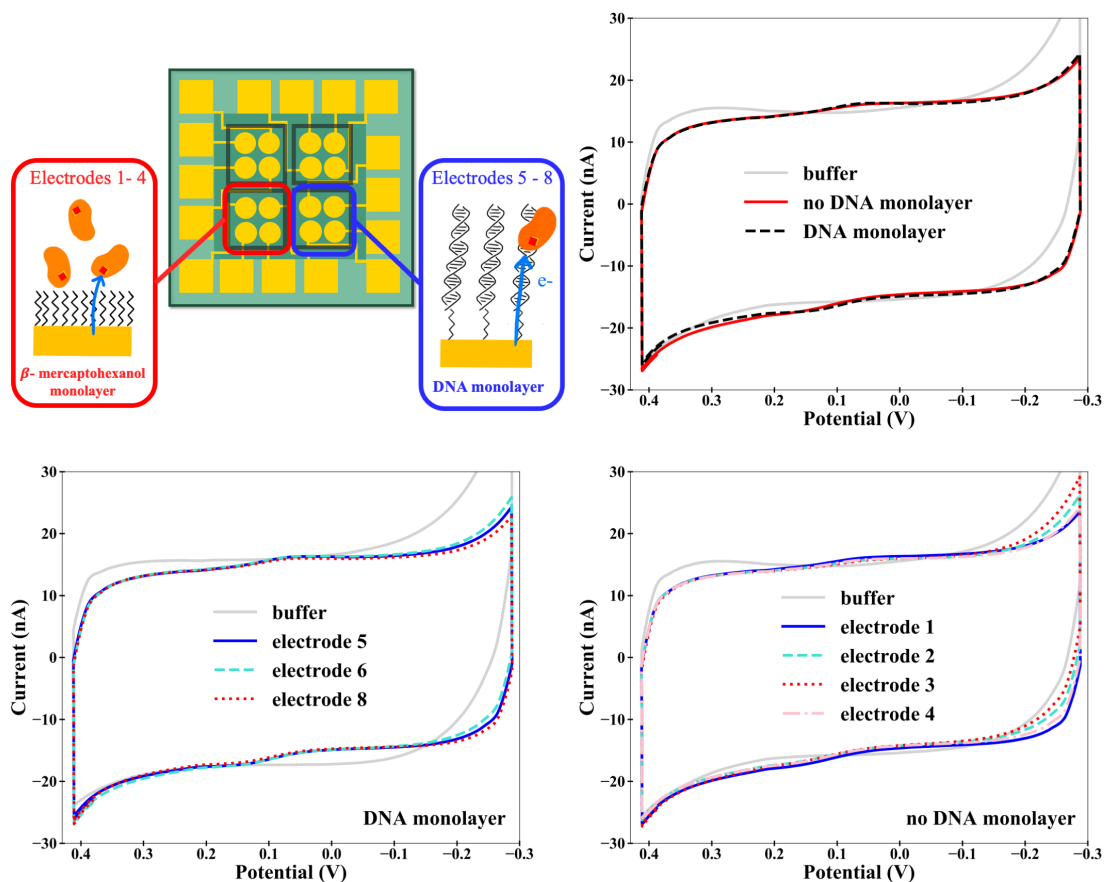


Figure 3.14: Cyclic Voltammetry of 13 μM EndoIII without EDTA. Schematic of multi-plexed gold electrode (top left). On one half of the chip there was a β -mercaptohexanol monolayer and on the other half a putative DNA-monolayer was prepared. EndoIII (13 μM) was deposited on entire chip and cyclic voltammetry was performed. Top right shows representative CVs from electrodes with β -mercaptohexanol monolayer (red) and electrodes with putative DNA-monolayer (black dashed). Bottom panel shows CVs from individual electrodes from quadrant with putative DNA monolayer (left) and β -mercaptohexanol monolayer (right). All CVs performed anaerobically in Dna2 phosphate buffer (20 mM Pi, 150 mM NaCl, pH 7.5) at 100 mV/s with Ag/AgCl gel-tip reference electrode.

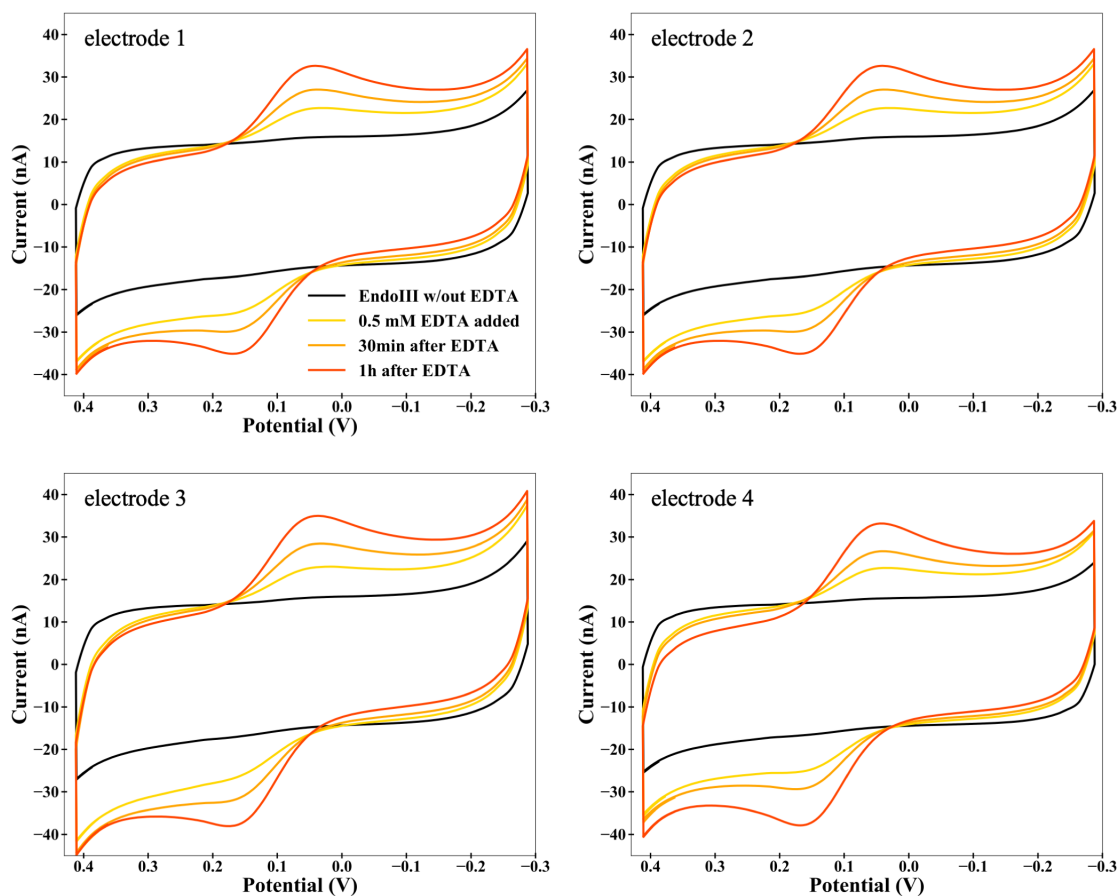


Figure 3.15: Addition of 0.5 mM EDTA to EndoIII on gold electrode with β -mercaptohexanol monolayer. Cyclic Voltammograms of 13 μ M EndoIII on multiplexed gold electrode with β -mercaptohexanol monolayer before (black) and after (orange) addition of EDTA to a final concentration of 0.5 mM EDTA. EndoIII (13 μ M) was added to the electrode surface and CV was performed every hour for 4 hours. Very small reversible signal was observed from EndoIII without EDTA (black trace, and Figure 11). Then, EDTA was added directly to the protein solution on the electrode surface and CV was performed immediately (yellow). CV was performed 30 min later (light orange) and 1 hour later (orange). Reversible signal with midpoint potential of about 90 mV vs. NHE appeared after addition of EDTA and increased over time. Four panels show CVs from four individual electrodes on the same multiplexed electrode chip. All CVs performed anaerobically in Dna2 phosphate buffer (20 mM Pi, 150 mM NaCl, pH 7.5) at 100 mV/s with Ag/AgCl gel-tip reference electrode.

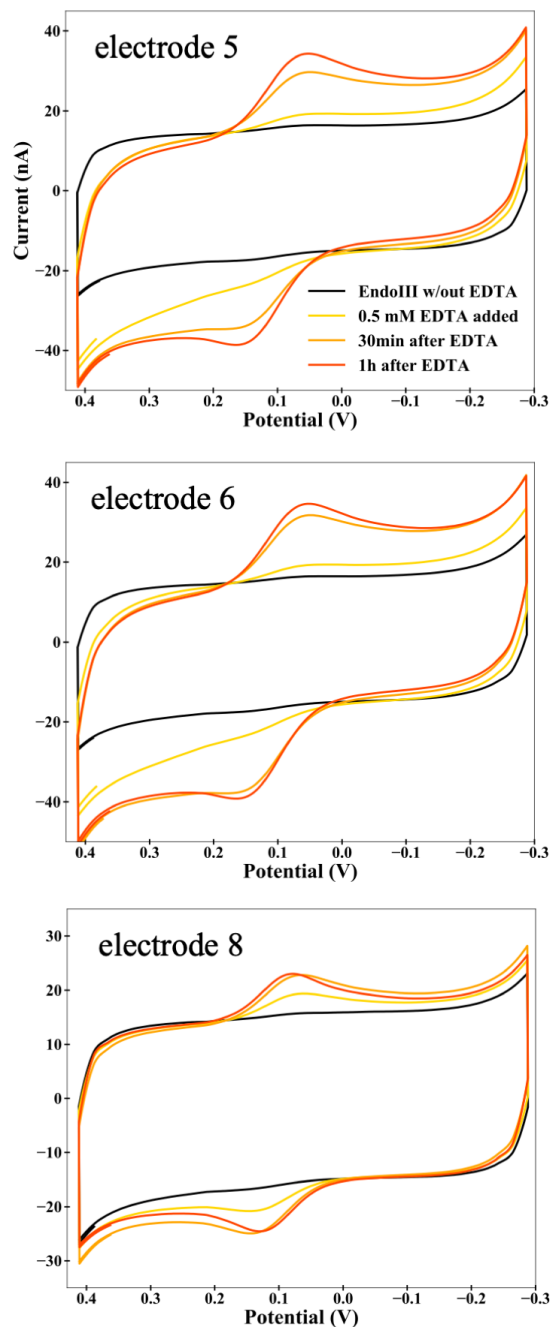


Figure 3.16: Addition of 0.5 mM EDTA to EndoIII on gold electrode with putative DNA monolayer. Cyclic Voltammograms of 13 μM EndoIII on multiplexed putative DNA-modified gold electrode before (black) and after (orange) addition of EDTA to a final concentration of 0.5 mM EDTA. EndoIII (13 μM) was added to the electrode surface and CV was performed every hour for 4 hours. Very small reversible signal was observed from EndoIII without EDTA (black trace, and Figure 11). Then, EDTA was added directly to the protein solution on the electrode surface and CV was performed immediately (yellow). CV was performed 30 min later (light orange) and 1 hour later (orange). Reversible signal with midpoint potential of about 90 mV vs. NHE appeared after addition of EDTA and increased over time. Three panels show CVs from three individual electrodes on the same multiplexed electrode chip. All CVs performed anaerobically in Dna2 phosphate buffer (20 mM Pi, 150 mM NaCl, pH 7.5) at 100 mV/s with Ag/AgCl gel-tip reference electrode.

The same experiment was performed with a 8 μM solution of Dna2 (Figure 3.17). A very small reversible signal was observed from 8 μM Dna2 in both quadrants with and without a DNA-monolayer. This signal was even smaller than that observed from 13 μM EndoIII and did not increase after more than 2 hours. Then, EDTA was added directly to this solution of Dna2 on the electrode surface to a final concentration of 0.4 mM. A signal grew in with a midpoint potential of 100 mV vs. NHE that is identical to what has been seen previously from Dna2 on putative DNA-modified electrodes.

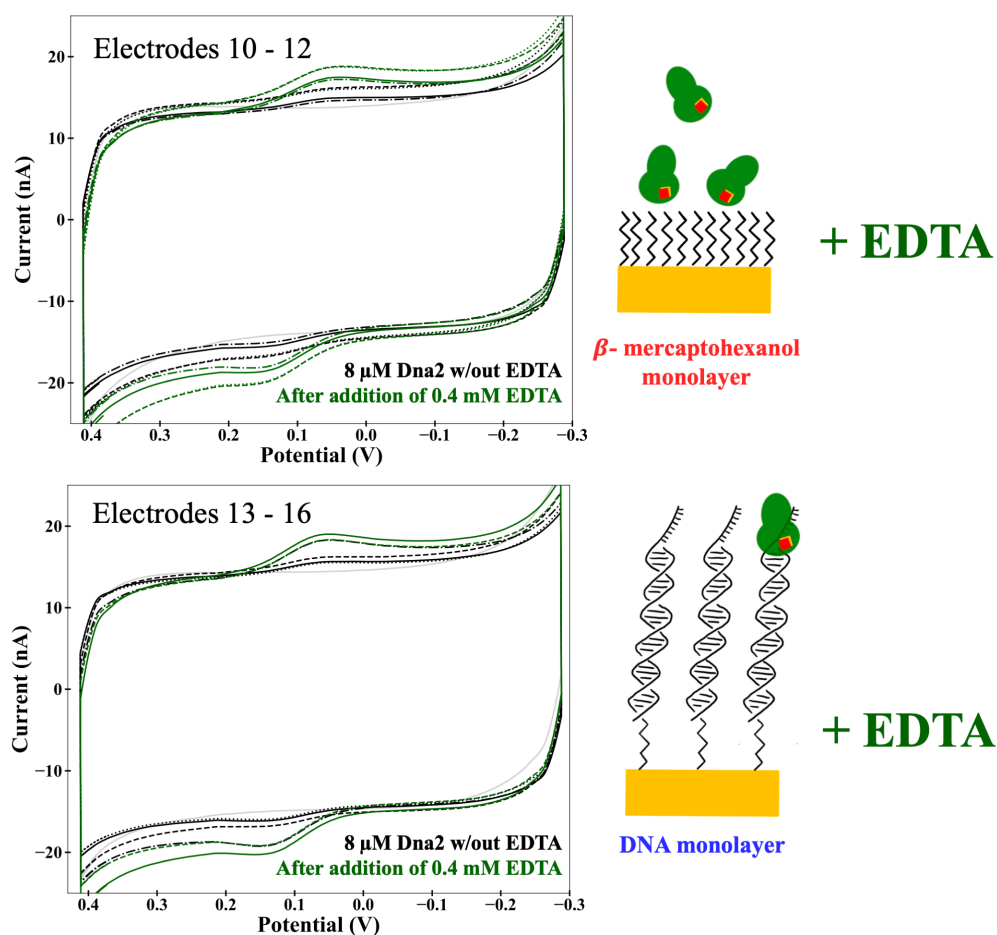


Figure 3.17: Addition of 0.4 mM EDTA to Dna2 on gold electrode with and without putative DNA monolayer. Cyclic Voltammograms of 8 μM Dna2 on multiplexed putative DNA-modified gold electrode before (black) and after (green) addition of EDTA to a final concentration of 0.4 mM EDTA. Dna2 (8 μM) was added to the electrode surface and CV was performed every hour for 2 hours. Very small reversible signal was observed from Dna2 without EDTA, even after 2 hours (black trace). Then, EDTA was added directly to the protein solution on the electrode surface and CV was performed (green). Reversible signal with midpoint potential of about 90 mV vs. NHE appeared after addition of EDTA. Solid, dashed, and dot-dashed lines are from 3 or 4 different electrodes. All CVs performed anaerobically in Dna2 phosphate buffer (20 mM Pi, 150 mM NaCl, pH 7.5) at 100 mV/s with Ag/AgCl gel-tip reference electrode.

The lack of a signal growth without EDTA in the buffer and the significant increase in the signal with addition of EDTA suggests that the redox activity that has been observed on putative DNA-modified electrodes is an artifact resulting from EDTA in our protein buffers. The above experiments with EndoIII were repeated five times on different days with different prepared electrodes and the same results were observed. Even at concentrations up to 20 μM by 4Fe-4S cluster, no signal was observed from EndoIII in cyclic voltammetry or square wave voltammetry in the absence of EDTA on putative DNA-modified electrodes. The redox activity of the 4Fe-4S cluster of EndoIII and Dna2 was not able to be observed with our putative DNA-modified electrochemistry procedure. Fresh electrodes were prepared in the Kavli Nanoscience Institute using the established protocol and there was still no signal from EndoIII without EDTA in the buffer. Fresh thiol-modified DNA was prepared and fresh MCH was purchased and used to make the DNA-monolayer and again, no signal was observed from EndoIII without EDTA. Ruling out these possible causes of the faulty DNA monolayer, other likely sources include the use of commercial DNA and defects/contamination on electrode surface. Instead of synthesizing the thiol-modified DNA using a DNA-synthesizer, as was done for some previously published DNA-modified electrochemistry reports, much of the DNA for these experiments was ordered from IDT. The thiol modified strand was deprotected according to the suppliers instructions and it was purified by HPLC and characterized by UV Vis. It's possible that the deprotection of the thiol modification was not complete, abrogating the binding of the DNA to the gold electrode surface and causing an incomplete DNA monolayer.

3.4 Conclusions and Future Outlook

The investigation reported here was conducted to support the conclusion that the reversible signal observed in CV from Dna2 was due to the DNA-mediated reduction and oxidation of the 4Fe-4S cluster. In doing so, it was revealed that the DNA monolayer was not properly formed as has been reported previously; very low levels of DNA were detected on the electrode surface after the self-assembled monolayer incubation period. Therefore, sufficient levels of 4Fe-4S cluster protein could not bind to the DNA monolayer and be oxidized/reduced by DNA-mediated charge transfer. The duplex DNA solutions used to prepare the monolayers are a likely cause of the insufficient DNA monolayer formation. Incomplete hybridization of the substrate DNA would cause ssDNA to be present on the electrode surface, which is known to adsorb to the surface and prevent formation of an ordered DNA monolayer. Additionally, incomplete removal of the thiol protecting group would prevent the formation of the bond between the DNA and the gold electrode that is

required for monolayer formation. A possible source of these insufficient DNA duplex solutions is the switch to the use of commercial DNA. In previous reports, the thiol-modified DNA for electrochemistry was usually synthesized on an Applied Biosystems 3400 DNA Synthesizer. However, in this report, the thiol-modified DNA and complement sequence were ordered from IDT. If the removal of the thiol-protecting group or the hybridization of this commercial DNA was not complete prior to incubation on the gold electrode surface, a self-assembled duplex DNA monolayer can not be formed. The use of Ellman's reagent is an important procedural step to detect free thiols (and thus, sufficient removal of the thiol protecting group) in the duplex DNA solution before preparation of the electrode. This is an important diagnostic test for the integrity of the DNA monolayer that was not performed for the experiments in this report or previously published reports on DNA-modified electrochemistry.

In addition to preventing the DNA CT between the electrode and the 4Fe-4S cluster protein, a faulty and disordered solution of DNA on the electrode surface will lead to a surface that is not well passivated, which can lead to degradation of 4Fe-4S cluster proteins [37]. The degradation of the 4Fe-4S clusters that was observed in this report is likely due to interaction between the 4Fe-4S cluster protein and the gold electrode. In cases where a proper DNA monolayer is formed on the electrode, the 4Fe-4S clusters would be protected from degradation because the DNA monolayer would prevent the enzyme from coming into contact with the electrode surface. The protein solutions need to be analyzed with UV-Vis before and after DNA-modified electrochemistry to confirm the integrity of the 4Fe-4S cluster.

Due to the major problems that were discovered in the preparation of the DNA monolayers that were used for this report, the observations in this report can not be extended to other DNA-modified electrochemical investigations of 4Fe-4S cluster proteins. The observations presented here suggest that Fe-EDTA is the source of the signal from 4Fe-4S clusters in cyclic and square wave voltammetry. However, in experiments where a satisfactory DNA monolayer is prepared on the electrode, the Fe-EDTA signal might not be observed and protein degradation might not occur. Furthermore, with a proper DNA monolayer, DNA CT could occur between the electrode and the 4Fe-4S cluster.

In order to use DNA-modified electrochemistry as a valid technique to probe the redox activity of 4Fe-4S cluster DNA-binding enzymes, appropriate controls need to be performed to confirm the integrity of the DNA monolayer and the 4Fe-4S cluster. The surface of the fabricated electrodes needs to be rigorously checked for defects, roughness, and contamination prior to use. A thorough characterization of the DNA monolayer,

using orthogonal, non-electrochemical techniques, needs to be performed with each DNA-modified electrochemical investigation. After DNA-modified electrochemistry, enzymes need to be removed from the electrode surface and analyzed by UV-Vis to establish the stability of the 4Fe-4S cluster. And importantly, the presence of other possible sources of electrochemical signals in the buffers needs to be evaluated, which can be achieved by buffer exchanging the protein into fresh buffer and performing voltammetry on the buffer flowthrough as well as the fresh protein solution. Although DNA-modified electrodes have been characterized previously by the Barton group, this characterization was not performed during the preparation of the electrodes for this report. This report provides a valuable cautionary tale of the confusing and inconclusive electrochemical signals that can arise with improper technique in preparation of DNA monolayers.

References

- (1) Barton, J. K.; Kumar, C. V.; Turro, N. J. *J. Am. Chem. Soc.* **1986**, *108*, 6391–6393.
- (2) Purugganan, M. D.; Kumar, C. V.; Turro, N. J.; Barton, J. K. *Science* **1988**, *241*, 1645–1649.
- (3) Kelley, S. O.; Barton, J. K.; Jackson, N. M.; Hill, M. G. *Bioconjugate Chem.* **1997**, *8*, 31–37.
- (4) Kelley, S. O.; Boon, E. M.; Barton, J. K.; Jackson, N. M.; Hill, M. G. *Nucleic Acids Res.* **1999**, *27*, 4830–4837.
- (5) Kelley, S. O.; Jackson, N. M.; Hill, M. G.; Barton, J. K. *Angew. Chem. Int. Ed.* **1999**, *38*, 941–945.
- (6) Boon, E. M.; Livingston, A. L.; Chmiel, N. H.; David, S. S.; Barton, J. K. *PNAS* **2003**, *100*, 12543–12547.
- (7) Boal, A. K.; Yavin, E.; Lukianova, O. A.; O’Shea, V. L.; David, S. S.; Barton, J. K. *Biochemistry* **2005**, *44*, 8397–8407.
- (8) Gorodetsky, A. A.; Boal, A. K.; Barton, J. K. *J. Am. Chem. Soc.* **2006**, *128*, 12082–12083.
- (9) Zwang, T. J.; Tse, E. C.; Barton, J. K. *ACS Chem. Biol.* **2018**, *13*, 1799–1809.
- (10) Mui, T. P.; Fuss, J. O.; Ishida, J. P.; Tainer, J. A.; Barton, J. K. *J. Am. Chem. Soc.* **2011**, *133*, 16378–16381.
- (11) Sontz, P. A.; Mui, T. P.; Fuss, J. O.; Tainer, J. A.; Barton, J. K. *PNAS USA* **2012**, *109*, 1856–1861.
- (12) Grodick, M. A.; Segal, H. M.; Zwang, T. J.; Barton, J. K. *J. Am. Chem. Soc.* **2014**, *136*, 6470–6478.

- (13) O'Brien, E.; Holt, M. E.; Thompson, M. K.; Salay, L. E.; Ehlinger, A. C.; Chazin, W. J.; Barton, J. K. *Science* **2017**, *355*.
- (14) Budd, M. E.; Campbell, J. L. *PNAS* **1995**, *92*, 7642–7646.
- (15) Lin, W.; Sampathi, S.; Dai, H.; Liu, C.; Zhou, M.; Hu, J.; Huang, Q.; Campbell, J.; Shin-Ya, K.; Zheng, L.; Chai, W.; Shen, B. *EMBO J.* **2013**, *32*, 1425–1439.
- (16) Levikova, M.; Cejka, P. *Nucleic Acids Res.* **2015**, *43*, 7888–7897.
- (17) Nanbu, T.; Nguyen, L. C.; Habib, A. G.; Hirata, N.; Ukimori, S.; Tanaka, D.; Masuda, K.; Takahashi, K.; Yukawa, M.; Tsuchiya, E.; Ueno, M. *PLoS One* **2015**, *10*, e0140456.
- (18) Ronchi, D. et al. *Am. J. Hum. Genet.* **2013**, *92*, 293–300.
- (19) Tammaro, M.; Liao, S.; Beeharry, N.; Yan, H. *Nucleic Acids Res.* **2016**, *44*, 221–231.
- (20) Lee, S. H.; Kim, Y. R.; Yoo, N. J.; Lee, S. H. *Korean J. Pathol.* **2010**, *44*, 354–359.
- (21) Strauss, C. et al. *Oncotarget* **2014**, *5*, 9396–9409.
- (22) Zhou, C.; Pourmal, S.; Pavletich, N. P. *eLife* **2015**, *4*, e09832.
- (23) Pinto, C.; Kasaciunaite, K.; Seidel, R.; Cejka, P. *eLife* **2016**, *5*, e18574.
- (24) Ekanger, L. A.; Oyala, P. H.; Moradian, A.; Sweredoski, M. J.; Barton, J. K. *J. Am. Chem. Soc.* **2018**, *140*, 11800–11810.
- (25) Ceres, D. M.; Udit, A. K.; Hill, H. D.; Hill, M. G.; Barton, J. K. *J. Phys. Chem. B* **2007**, *111*, 663–668.
- (26) Barton, J. K.; Bartels, P. L.; Deng, Y.; O'Brien, E. *Meth. Enzymol.* **2017**, *591*, 355–414.
- (27) Yu, H. Z.; Luo, C. Y.; Sankar, C. G.; Sen, D. *Anal. Chem.* **2003**, *75*, 3902–3907.
- (28) Pheaney, C. G.; Arnold, A. R.; Grodick, M. A.; Barton, J. K. *J. Am. Chem. Soc.* **2013**, *135*, 11869–11878.
- (29) Bartels, P. L.; Zhou, A.; Arnold, A. R.; Nuñez, N. N.; Crespilho, F. N.; David, S. S.; Barton, J. K. *Langmuir* **2017**, *33*, 2523–2530.
- (30) Weaver, J.; Pollack, S. *Biochem.* **1989**, *261*, 787–792.
- (31) Romslo, I. In *Iron in Biochemistry and Medicine*, Jacobs, A., Wormwood, M., Eds.; Academic Press Inc: 1983, pp 325–362.
- (32) Ahmad, S.; Rao, G. S. *J. Anal. Toxicol.* **1997**, *21*, 172–173.
- (33) Vogel, H. J.; Shimura, Y. *Meth. Enzymol.* **1971**, *17*, 228–229.
- (34) Duff, J. L.; Breton, J. L.; Butt, J. N.; Armstrong, F. A.; Thomson, A. J. *J. Am. Chem. Soc.* **1996**, *118*, 8593–8603.

- (35) Kocot, P.; Karocki, A.; Stasicka, Z. *J. Photochem. Photobiol. A* **2006**, *179*, 176–183.
- (36) Hutcheson, R. M.; Engelmann, M. D.; Cheng, I. F. *Biometals* **2005**, *18*, 43–51.
- (37) Davis, J. J.; Halliwell, C. M.; Hill, H. A. O.; Canters, G. W.; Van Amsterdam, M. C.; Verbeet, M. P. *New J. Chem.* **1998**, *22*, 1119–1123.
- (38) Tse, E. C.; Zwang, T. J.; Barton, J. K. *J. Am. Chem. Soc.* **2017**, *139*, 12784–12792.

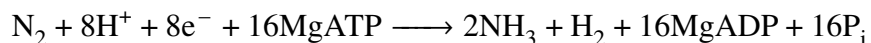
*Chapter 4***INVESTIGATING THE MECHANISM OF NITROGENASE
REDUCTION WITH PROTON INVENTORY STUDIES****4.1 Introduction**

Nitrogenase is the only known biological enzyme that can convert atmospheric dinitrogen, one of the most inert molecules on our planet, into ammonia, an integral building block for the proteins and DNA that make up all life [1, 2]. This reaction, nitrogen fixation, is of great interest to humans because ammonia is a major component of the fertilizers we need to sustain our food supply [3] (despite that fact that 50-75% of applied nitrogen is not absorbed by plants [4]). In 1909, the Haber-Bosch process was developed to industrially perform the nitrogen fixation reaction and while this development was paramount to supporting our growing population, it has contributed substantially to our global CO₂ emissions and depleted our energy resources [3, 5]. In the Haber-Bosch process, N₂ and H₂ are treated over a metal catalyst at pressures of 250-350 bar and temperatures of 600-800 K. The bacterial enzyme nitrogenase fixes dinitrogen at ambient temperature and pressure, sourcing the protons from water [1].

Nitrogenase enzymes are found in a special group bacteria and archaea called *diazotrophes*, many living symbiotically on the root nodules of plants or freely in soil, and the most well-studied forms are those from *Azotobacter vinelandii* and *Clostridium pasteurianum*. These organisms contain genes for 3 types of nitrogenase, named for the distinguishing metal in their active site: Mo-nitrogenase, V-nitrogenase, and Fe-nitrogenase. The focus of this study, Mo-nitrogenase from *A. vinelandii*, is the default nitrogenase for this organism and the other forms are only expressed in molybdenum or vanadium limiting conditions [6]. Nitrogenase is made up of two component proteins, the MoFe protein (Av1), which houses the active site, and the Fe protein (Av2) which is a necessary partner and delivers electrons to the MoFe protein. The Fe protein contains a 4Fe-4S cluster that bridges the two subunits of this component protein and is the source of electron transfer to the MoFe protein. The MoFe protein contains two complex metalloclusters: the active site FeMo-cofactor, a [Fe₇S₉Mo] cluster with an interstitial carbide and a coordinating *R*-homocitrate, and the [Fe₈S₇] P-cluster involved in electron transfer from the [Fe₄S₄] cluster of the Fe protein. [7, 8].

Decades of study on nitrogenase have revealed detailed information about the structure

and activity of the enzyme; however, much is still unknown about the mechanism of reduction. Although the reduction of N_2 to NH_3 is thermodynamically favorable ($\Delta G = -63.62$ kJ/mol N_2) [9], there is a large activation barrier for the reaction and nitrogenase requires at least 16 equivalents of ATP per N_2 fixed as well as 8 reducing equivalents [10, 11]:



The reducing equivalents are transferred to the active site of the MoFe protein from the 4Fe-4S cluster of the Fe protein (which is itself reduced by flavodoxin or ferredoxin). Electron transfer from the Fe protein to the MoFe protein proceeds as follows: reduced Fe protein binds to the MoFe protein, the Fe protein hydrolyzes ATP causing a conformational change that induces electron transfer from the 4Fe-4S cluster of the Fe protein to the P-cluster of the MoFe protein, ADP-bound Fe protein dissociates from the MoFe protein and is re-reduced [12]. Each of these Fe protein cycles of binding, ATP hydrolysis and electron transfer is responsible for the transfer of one electron to the active site (through the P-cluster) [12–15]. In order for dinitrogen to bind to the active site, 3–4 of these cycles must occur, building up 3–4 electrons and protons on the FeMo-cofactor [16, 17]. At this point, dinitrogen binds and subsequent cycles of electron transfer will lead to reduction of the substrate.

In addition to dinitrogen, nitrogenase can reduce a variety of other substrates including C_2H_2 , HCN, $SeCN^-$, SCN^- , and N^{3-} . In the absence of other substrates, or at sufficiently low concentrations of other substrates, nitrogenase will also reduce protons from water to form H_2 . The substrates of focus in this study are acetylene and protons due to their relevance to the overall nitrogen fixation reaction. The acetylene reduction assay is ubiquitous in the field of nitrogen fixation research, both in experiments with purified nitrogenase enzymes, and *in vivo* investigations of nitrogen fixing organisms. This assay is used to measure general nitrogenase activity because acetylene is isoelectronic to N_2 and the product, ethylene, is more straightforward to quantify than ammonia [18]. Dihydrogen is another well studied product of nitrogenase because, in addition to being produced in the absence of substrate, H_2 evolution is observed whenever nitrogenase is reducing N_2 to ammonia [10]. In fact, there is evidence to suggest that H_2 production by nitrogenase is necessary to activate the enzyme for its most important role of nitrogen fixation [19]. For this study, in which the isotopic composition of nitrogenase products are quantified, acetylene and protons are particularly optimal substrates because the gaseous nature of their products makes isotope exchange with solvent after product release an insignificant

variable in their isotopic composition. Even when dissolved in aqueous solution the H-H and C-H bonds of dihydrogen and ethylene, respectively, don't exchange with solvent H/D atoms on the timescale of our reactions.

Stable isotope substitutions, the focus of this report, have a rich history of providing information about how nitrogenase reacts with substrates. One of the most important discoveries of the biological nitrogen fixation reaction, that ammonia is the product of nitrogenase, was established by Burris and co-workers using $^{15}\text{N}_2$ as the substrate for *Azotobacter agile* and detecting ^{15}N -labeled ammonia [20]. Another heavy isotope, deuterium, was paramount to discovering the important relationship between H_2 and N_2 during nitrogen fixation. In N_2 fixing conditions under D_2 (in H_2O), nitrogenase will produce HD and formation of the HD product is largely dependent on the presence of N_2 [21]. This observation was groundbreaking and inspired much future work toward elucidating the role of H_2 evolution in N_2 reduction. Stable isotopes have further provided information about the orientation, stoichiometry, and exchange properties of acetylene binding to the nitrogenase active site. Acetylene reduction assays with C_2D_2 (in H_2O) provided the valuable insight that nitrogenase predominantly produces *cis*- $\text{C}_2\text{H}_2\text{D}_2$ with only a small fraction of the *trans*- species [22]. Using ^{13}C -acetylene and ^{13}C ENDOR, Lee et al. were able to detect two acetylene molecules bound to the FeMo-cofactor of a nitrogenase mutant; ^1H ENDOR on the C_2H_2 - and C_2D_2 -bound species in H_2O and D_2O established that H/D atoms on the bound acetylene cannot exchange with solvent [23]. In addition to these qualitative observations, stable isotopes were used to quantitatively measure the $^{15}\text{N}/^{14}\text{N}$ kinetic isotope effect for N_2 reduction using isotope ratio mass spectrometry (1.017 ± 0.002) [24].

The deuterium isotope is particularly valuable for mechanistic explorations because the factor of two difference in atomic mass between H and D contributes to a potentially significant kinetic isotope effect. A kinetic isotope effect is defined as a change in the rate of a reaction upon isotopic substitution of atoms in the reaction. These effects can provide information about the atoms involved in the reaction mechanism, the structure of the transition state, and the rate limiting step. Solvent isotope experiments are a type of isotope study in which the protons of the solvent are replaced with deuterium (in this case, H_2O replaced with D_2O) [25]. For a change in rate to be observed upon deuterium enrichment of the solvent, solvent H/D atoms must be involved in the rate limiting step. The rate limiting step in the nitrogenase mechanism has been identified as the dissociation of inorganic phosphate from the Fe protein after ATP hydrolysis during the electron transfer cycle [26], of which multiple cycles are necessary to build up reducing equivalents at

the active site of the MoFe protein. Changes in rate of reduction upon D₂O enrichment of the solvent have not been observed with nitrogenase¹ because any changes in rate associated with H⁺/D⁺ transfer at the active site are eclipsed by the slow dissociation of P_i from the Fe protein in each electron transfer cycle. However, this does not preclude the use of solvent isotope experiments to learn about the nitrogenase mechanism at the active site. For irreversible reactions that result in incorporation of non-exchangeable H atoms into products (such as acetylene and proton reduction by nitrogenase), the relative amount of deuterium incorporation into the products can be used to unmask the isotope effects associated with hydrogen transfer at the active site and can shed light on the reaction pathway. These measurements are often termed product deuterium isotope effect experiments [28].

Isotope effect experiments in mixed H₂O/D₂O buffers offer advantages over those determined from separate assays in either H₂O or D₂O because error due to differences in experimental conditions such as pL (*L* denotes either H or D) and temperature across reaction vials can be minimized and there is no need to correct for secondary solvent isotope effects [29]. When the reaction mechanism involves the transfer of one hydrogen, the isotope effect is simply the ratio of the amount of products with hydrogen incorporated to the amount of products with deuterium incorporated divided by the D₂O/H₂O ratio of the solvent [29, 30]. When more than one hydrogen transfer occurs, as is the case with all reductions performed by nitrogenase, products with multiple levels of deuteration can be formed and the isotope effect can be calculated from the relative levels of these products.

The level of incorporation of heavy isotopes into enzyme products are also of interest in the field of geochemistry and these results are termed *fractionation factors* instead of isotope effects. The fractionation of a heavy isotope such as deuterium is related to the ratio of the amount of deuterium in the product (in parts per thousand) to the natural abundance of deuterium in a standard water sample. Mechanistic conclusions are rarely made from these

¹To our knowledge, the only change in overall nitrogenase substrate reduction with substitution of H₂O for D₂O in the solvent was observed with the reduction of acrylonitrile to propane and propylene [27]. In Mo-nitrogenase assays in D₂O, the yield of products of acrylonitrile reduction were twice that of assays in 100% H₂O. Enhancement of reduction products in D₂O was also seen for reduction of propionitrile to propane and acetonitrile to ethane. The *K_m* for acrylonitrile reduction was the same in H₂O and D₂O, indicating that the enhancement of reduction in D₂O was not due to changes in binding affinity of acrylonitrile for the active site of nitrogenase. Instead, the isotope effect was explained as resulting from an increase in the available electrons used to reduce acrylonitrile relative to protons; D₂O promotes acrylonitrile reduction at the expense of hydrogen evolution. Although no isotope effect was observed on total H₂ evolution in the absence of substrate, the authors suggest that a slight isotope effect on H₂ evolution is enhanced or manifested during substrate reduction. The mechanistic conclusions made from this result are as follows: the activation energy for electron transfer to acrylonitrile, H₃O⁺, and D₃O⁺ are relatively similar and substitution of D₃O⁺ for H₃O⁺ causes a shift in relative electron transfer activation energies favoring increased electron transfer to acrylonitrile.

fractionation factors and instead, they provide clues as to the microbial sources of important chemicals such as NH_3 and CH_4 in the environment [31–35]. Upon inspection of the definitions of isotope effect and fractionation factor, in the case of solvent isotope effect experiments where protons are sourced from the solvent as in reduction by nitrogenase, the fractionation factor is the reciprocal of the isotope effect. In this work, we calculate isotope effects of nitrogenase reduction assays; however, the results can also easily be expressed as fractionation factors and are relevant to studies of geological nitrogen fixation.

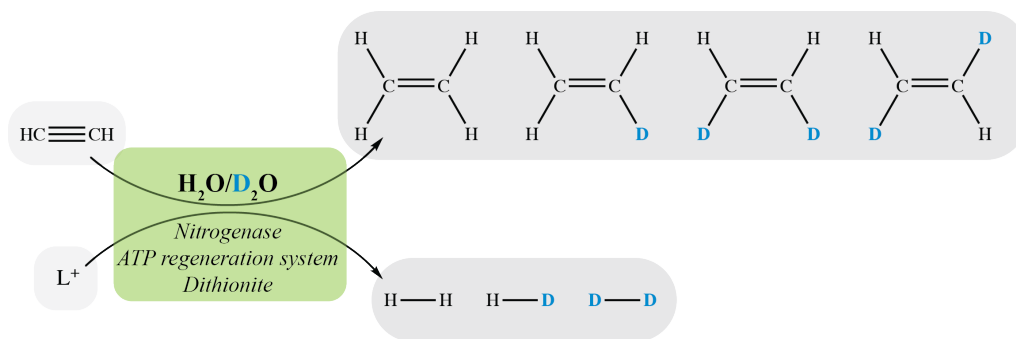


Figure 4.1: Isotope effect experiments of acetylene and proton reduction assays by nitrogenase from *A. vinelandii*. Acetylene and proton reduction assays were performed in mixed $\text{H}_2\text{O}/\text{D}_2\text{O}$ buffers and the relative amounts of product isotopologues were quantified. Products of acetylene reduction assays are d_0 -ethylene, d_1 -ethylene, *cis*- d_2 -ethylene, and *trans*- d_2 -ethylene. Products of proton reduction assay are H_2 , HD, and D_2 . All nitrogenase assays require the ATP regeneration system and a reductant (in this case, dithionite).

In this study, we evaluated the potential role of solvent isotope effects in the nitrogenase mechanism by performing acetylene, cyanide and proton reduction assays in buffers of varying mole fraction of deuterium (Figure 4.1). The products of these reactions, ethylene, methane, and dihydrogen, respectively, are well suited for these studies since the H/D(s) incorporated during substrate reduction do not subsequently exchange with solvent, a process that precludes characterization of the ammonia product of dinitrogen reduction by this approach. The product isotopologues were quantified by GC-MS, FTIR, and ^1H NMR and these data were used to determine the isotope effect associated with the reduction of protons to H_2 and acetylene to ethylene. Interestingly, these results show that the isotope effect of acetylene reduction by nitrogenase is small (1.4 ± 0.05), while that of the reduction of protons to H_2 is significantly greater at 4.2 ± 0.1 , suggesting differences in the H-atom transfer steps during reduction of these two substrates. We note that our results from proton reduction assays are comparable to an early report that quantified dihydrogen isotopologue products of partially purified nitrogenase from *A. vinelandii* [36]. Due to

uncertainty in the deuterium fractionation of the substrate for cyanide reduction assays (HCN vs. DCN), the isotope effect of this reaction could not be precisely measured; however, our results reveal that the value of the isotope effect for this reaction is likely even greater than that of proton reduction.

Nitrogenase is often thought of as a relatively non-specific, sequential deliverer of electrons and protons to reduced substrates, as electron flux through nitrogenase is typically independent of the substrate being reduced [37]. Therefore, it could be expected that the level of H/D isotope discrimination during reduction would also be independent of the substrate. However, the significantly different solvent isotope effects that we observe in the reductions of acetylene and protons support variations in the H-atom transfer steps during reduction of these two substrates, and are indicative of differences in the detailed reduction mechanisms of different substrates by nitrogenase.

4.2 Methods

Materials and Buffer Preparation

Dithionite and all components of the ATP regeneration system (creatine phosphate, ATP, creatine phosphokinase) were purchased from Sigma Aldrich. Tris buffer (50 mM, pL = 7.8) was prepared in H₂O and D₂O (Cambridge Isotope Labs) and combined in appropriate ratio for the desired final D₂O composition of assay. Buffers were adjusted to pL = 7.8 with either HCl or DCl. For buffers containing D₂O, the pH meter was first immersed in 100% D₂O for 20 minutes prior to use. The following calculation was used to convert the reading on the pH meter (pH_{obs}) to the actual pL of the solution [38]:

$$pL = pH_{obs} + 0.311n + 0.0766n^2$$

where n is the mole fraction of deuterium in the solution. The mole fraction of deuterium in the final buffers were confirmed by NMR and the error in D₂O percentage of the solution was measured to be 3%.

Nitrogenase Expression and Purification

Nitrogenase from *A. vinelandii* was purified as previously described [39]. Briefly, *A. vinelandii* was grown in Burk's minimal media (20 g/L sucrose, 0.2 mM FeSO₄ • 7 H₂O, 3 μM Na₂MoO₄ • 2 H₂O, 1.67 mM MgSO₄, 0.9 mM CaCl₂, 0.9 mM KH₂PO₄ pH 7.5, 1.3 mM NH₄Cl) in a 10 L fermenter and harvested at OD₆₀₀ = 0.8-1.7. The purification of nitrogenase was conducted under anaerobic conditions. The harvested cells were resuspended in degassed lysis buffer (50 mM Tris/HCl pH 7.5, 150 mM NaCl, 5 mM dithionite) and homogenized with handheld homogenizers. Cells were lysed with an

Emulsiflex C5 (pressurized with argon gas) and the supernatant was loaded onto a HiTrap Q HP anion exchange column on an Akta FPLC system and eluted with an NaCl gradient. The MoFe and Fe protein fractions (eluting at 260-330 mM NaCl and 420-460 mM NaCl, respectively) were collected, concentrated, and loaded onto a Superdex 200 equilibrated with anaerobic 50 mM Tris/HCl pH 7.5, 200 mM NaCl, 5 mM dithionite. Acetylene reduction activity assays were performed after each purification (specific activity ≈ 3000 nmol ethylene min^{-1} mg Av1 $^{-1}$). See Figure B.1 for representative FPLC traces and protein gels from purifications.

Nitrogenase Acetylene Reduction Assay

The ATP regeneration system (final concentrations: 15 mM creatine phosphate, 3.8 mM ATP, 3.8 mM MgCl₂, 50 units/mL creatine phosphokinase) was prepared in buffer (50 mM Tris/HCl, pH 7.8) of appropriate deuterium enrichment to provide the desired final isotope composition in the assay. This solution was transferred (1 mL each) to 9 mL Wheaton vials and the vials were sealed with a polytetrafluoroethylene (PTFE) septa with an aluminum cap. The vials were degassed with 12 cycles of 2 min vacuum followed by 1 min argon. Dithionite (DT, 0.5 M in 0.5 M Tris base pH 10.1, 50 μL , final [DT] in assay = 20 mM), 5mM DT SEC buffer (50 mM Tris/HCl, 200 mM NaCl, pH 7.8), acetylene (1 mL, 1 atm, 40.8 μmol , 10% of assay atmosphere), and Av1 (0.03 mg per assay) were added by gas-tight Hamilton syringe. The appropriate amount of Av2 [component ratio (mol Av2:mol FeMo cofactor) = 3-25] was added to start the reaction and the vials were incubated at 30 °C with shaking. The reaction was quenched after 10-30 min by the addition of citric acid (3 M, 1 mL). For quantification of total ethylene, the headspace (50 μL) was injected into a SRI Instrumens GC equipped with an activated alumina column (60/80 mesh) operated at 110 °C and a flame ionization detector.

Gas Chromatography-Mass Spectroscopy Quantification of Ethylene Isotopologues

For quantification of ethylene isotopologues, the headspace (50 μL) of acetylene reduction assays was injected into an HP 5890 Gas Chromatograph with an HP 5972 Mass Spectrometer equipped with a GASPRO PLOT-Q (Restek) column operated at 80 °C. Overlapping ethylene isotopologue mass spectra are deconvoluted using the fragmentation pattern of a C₂H₄ standard (see Figures B.2 & B.3 and Appendix Section B.4).

Fourier Transform Infrared Spectroscopy Quantification of Ethylene Isotopologues

Acetylene reduction assays were performed as described above, except the reactions were scaled up 3X and glass beads were used in the Wheaton vial to minimize headspace

volume, thereby increasing the concentration of ethylene in the gas phase. An FTIR gas cell with NaCl windows was degassed (10 cycles of vacuum followed by backfilling with argon) and placed in the sample chamber of a Bruker Vertex 80 FTIR Spectrometer. The sample chamber was purged for 15 minutes with N₂ and then a background scan was run (128 scans, 1 cm⁻¹ resolution). The headspace of the assay reaction vial was transferred to the sample cell by vacuum with a cannula. The sample chamber was closed and allowed to purge with N₂ for 15 minutes and then an FTIR scan was performed. Peak heights of the stretches in the 840-1000 cm⁻¹ region, corresponding to the wagging mode of the H-C-H or H-C-D moieties [40], were used to quantify the ethylene isotopologue species. The molar absorptivities of the C₂H₄ stretch (949 cm⁻¹) and the C₂H₂D₂ stretch (843 cm⁻¹) are reported to be equivalent. However, there is a discrepancy in the literature as to whether the C₂H₃D stretch (943 cm⁻¹) has a molar absorptivity that is the same, or only half, that for C₂H₄ and C₂H₂D₂ [22, 41, 42]. Therefore, a standard curve was performed with C₂H₄ and C₂H₃D to determine their molar absorptivities as described in Appendix Section B.5, which confirmed that the molar absorptivity of C₂H₃D is about half of that of C₂H₄ and C₂H₂D₂.

Proton Reduction Assay

The proton reduction assay was performed in the same way as the acetylene reduction assay, except for the omission of acetylene in the reaction vials, and the reaction volume was scaled up. The ATP regeneration system (final concentrations: 15 mM creatine phosphate, 3.8 mM ATP, 3.8 mM MgCl₂, 50 units/mL creatine phosphokinase) was prepared in the appropriate buffer (50 mM Tris/HCl, pH 7.8) to provide the desired final isotope composition in the assay. This solution was transferred (2.2 mL each) to 9 mL Wheaton vials (equipped with glass beads to take up space) and the vials were sealed with PTFE septa with aluminum caps. The vials were degassed with 12 cycles of 2 min vacuum followed by 1 min argon. Dithionite (DT, 0.5 M in 0.5 M Tris base pH 10.1, 150 μL, final [DT] in assay = 20 mM), 5 mM DT SEC buffer (50 mM Tris/HCl pH 7.8, 200 mM NaCl), and Av1 (0.09 mg Av1 per assay) were added by gas-tight Hamilton syringe. The appropriate amount of Av2 (component ratio = 15) was added to start the reaction (total reaction volume = 3 mL) and the vials were incubated at 30 °C with shaking. The reaction was quenched after 10-60 min by the addition of citric acid (3 M, 1 mL). For quantification of total L₂, the headspace (100 μL) was injected into a HP 5890 GC equipped with a molecular sieve 5 Å column operated at 110 °C and a thermal conductivity detector. H₂ standard curves were performed with each assay.

¹H NMR Quantification of H₂ and HD

The headspace (3 mL) from the proton reduction assay was transferred using a gastight Hamilton syringe to an NMR tube filled with CDCl₃ (1 mL) and equipped with a PTFE septa, bubbling the headspace through the CDCl₃. ¹H NMR spectra were taken on a Varian 600 MHz Spectrometer with a 5 mm triple resonance inverse probe with deuterium decoupling. The relaxation delay was 16 sec, the pulse angle was 90° and at least 256 scans were performed. The H₂ and HD peaks were confirmed with standards. Baseline correction, phase shifting and peak fitting were performed in Mestrenova and the areas under the fitted peaks were used to determine the relative quantities of H₂ and HD (peak area of HD peak multiplied by two). Unfortunately, ²H NMR was not sensitive enough to detect D₂ from our assays.

Note: We first attempted to quantify the products of proton reduction assays (H₂, HD, and D₂) in H₂O/D₂O with GC-MS. Modifications to the GC-MS system were made to optimize quantification of the hydrogen isotopologues and are described in Appendix Section B.8. When the headspace of nitrogenase proton reduction assays was analyzed with these GC-MS conditions, the results agreed with the quantification by ¹H NMR reported below; however, the precision was not satisfactory (Figure B.10 and Table B.3).

NaCN Reduction Assays

The sodium cyanide reduction assays were performed in a similar manner to the proton and acetylene reduction assays. The ATP regeneration system (final concentrations: 15 mM creatine phosphate, 3.8 mM ATP, 3.8 mM MgCl₂, 19 units creatine phosphokinase) was prepared in buffer (50 mM Tris/HCl pH 7.8) of appropriate deuterium enrichment to provide the desired final isotope composition in the assay. This solution was transferred (1 mL each) to 9 mL Wheaton vials and the vials were sealed with a PTFE septa with an aluminum cap. The vials were degassed with 12 cycles of 2 min vacuum followed by 1 min argon. Dithionite (0.5 M in pH 10.1 0.5 M Tris base, 50 μL, final conc. = 20 mM), 5mM DT SEC buffer (50 mM Tris/HCl pH 7.8, 200 mM NaCl), NaCN (50 μL, 50 mM/25mM in 5 mM DT SEC, 2.5/1.25 μmol, final concentration in assay either 2 or 1 mM), and Av1 (0.125 mg per assay) were added by gas-tight Hamilton syringe. The appropriate amount of Av2 (component ratio = 4 or 8) was added to start the reaction and the vials were incubated at 30 °C with shaking. The reaction was quenched after 15-30 min by the addition of citric acid (3 M, 1 mL). For quantification of total methane, the headspace (50 μL) was injected into an SRI Instruments GC equipped with an activated alumina column (60/80 mesh) operated at 110 °C and a flame ionization detector.

Gas Chromatography-Mass Spectroscopy Quantification of Methane Isotopologues

For quantification of methane isotopologues, the headspace (50 μL) of NaCN reduction assays was injected into a HP 5890 Gas Chromatograph with a HP 5972 Mass Spectrometer equipped with a Molecular Sieve 5 A (Restek) column operated at 70 $^{\circ}\text{C}$ with splitless injection. Mass spectra were generated by integrating under the methane peak of the extracted ion chromatograms at $m/z = 13\text{-}20$. Overlapping methane isotopologue mass spectra were deconvoluted using the fragmentation pattern of a CH_4 standard in an analogous manner to the method used for ethylene mass spectra.

4.3 Results

Acetylene and Proton Reduction

We first confirmed literature reports [22, 36], demonstrating the absence of a significant solvent kinetic isotope effect on the specific activity of acetylene and proton reduction by nitrogenase. In both acetylene and proton reduction assays, the maximal rates of ethylene or H_2 produced in H_2O versus 51% D_2O agreed within 10-20% (Figure 4.2), although it is to be noted that the rate in H_2O was somewhat larger for both substrates.

Gas Chromatography Mass Spectroscopy (GC-MS) and Fourier Transform Infrared Spectroscopy (FTIR) were used to detect and quantify the ethylene isotopologue products of acetylene reduction by nitrogenase in 51% D_2O buffer (Figure 4.3, bottom left). In the mass spectra of the ethylene peak from assays in 100% H_2O , the molecular ion was at $m/z = 28$, as expected for the C_2H_4 product, and the magnitude of the abundance observed at $m/z = 29$ was 2% of the molecular ion, consistent with the 1.1% natural abundance of ^{13}C . The ethylene mass spectra obtained from assays performed in 51% D_2O showed significant abundance at both $m/z = 29$ and $m/z = 30$ that were not present in spectra C_2H_4 alone, indicating the formation $\text{C}_2\text{H}_3\text{D}$ and $\text{C}_2\text{H}_2\text{D}_2$ as products of nitrogenase upon deuterium enrichment of the buffer (Figure 4.3, bottom left). Minimal abundance at $m/z = 31$ (ranging from undetectable to 5% of the molecular ion peak) was probably due to the natural abundance of ^{13}C in the products and possibly very small amounts of C_2HD_3 . As expected, no abundance was observed at $m/z = 32$, indicating that C_2D_4 was not formed. The overlapping mass spectra of C_2H_4 , $\text{C}_2\text{H}_3\text{D}$, and $\text{C}_2\text{H}_2\text{D}_2$ were deconvoluted as described in Appendix Section B.4 and the distribution of products was determined to be $28 \pm 2\%$ C_2H_4 , $52 \pm 2\%$ $\text{C}_2\text{H}_3\text{D}$, and $20 \pm 1\%$ $\text{C}_2\text{H}_2\text{D}_2$ (*cis*- and *trans*- d_2 -ethylene could not be distinguished by GC-MS). The $m/z = 27$ abundance of the acetylene peak was monitored to determine the extent of H/D exchange in the substrate pool, revealing that C_2HD made up $<1\%$ of the total acetylene on the timescale of our assays.

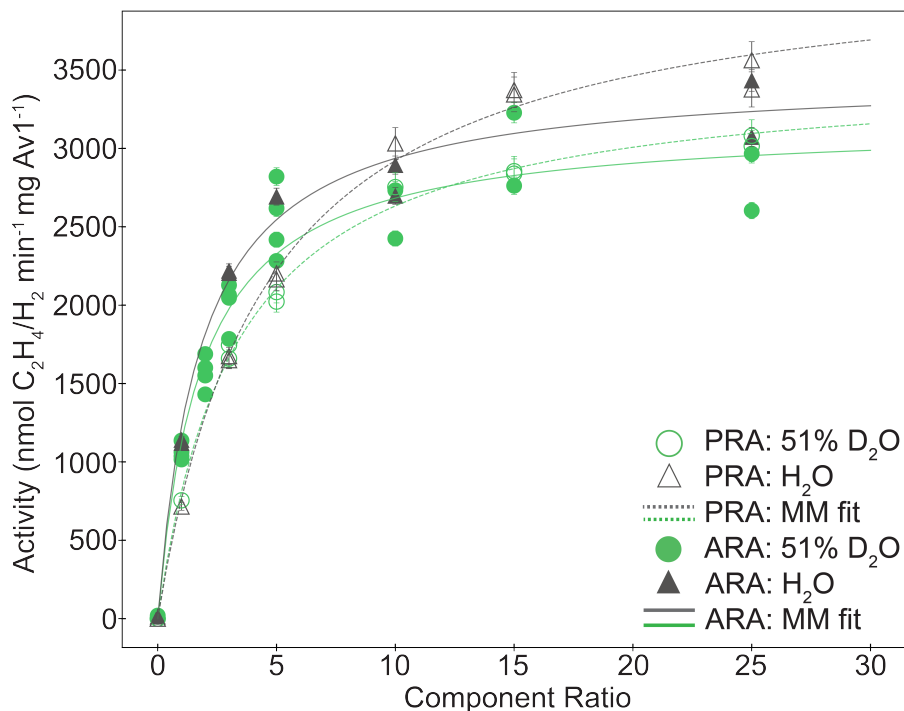


Figure 4.2: Total acetylene and proton reduction activity of nitrogenase in mixed isotope buffers. Acetylene and proton reduction assays were performed separately as described in *Methods*. Acetylene reduction assays (solid markers, solid lines) were quenched after 10 min and ethylene was quantified by injecting 50 μL of headspace into the GC-FID. Proton reduction assays (hollow markers, dashed lines) were quenched after 30 min and H_2 was quantified by injecting 100 μL of headspace into the GC-TCD. Standard curves were produced by preparing assay vials in the same method as experimental samples omitting protein and injecting known volumes of ethylene or dihydrogen. Standard curves were used to calculate the activity (nmol $\text{C}_2\text{H}_4/\text{H}_2$ per min per mg Av1). Error bars on points are calculated from relative error of two replicates of standard curves. Data was fit to the Michaelis Menton equation: $V_{max, \text{H}_2\text{O}, \text{ethylene}} = 3500 \pm 100 \text{ nmol min}^{-1} \text{ mg Av1}^{-1}$; $K_{m, \text{H}_2\text{O}, \text{ethylene}} = 1.8 \pm 0.3$; $V_{max, 51\% \text{D}_2\text{O}, \text{ethylene}} = 3200 \pm 100 \text{ nmol min}^{-1} \text{ mg Av1}^{-1}$; $K_{m, 51\% \text{D}_2\text{O}, \text{ethylene}} = 1.8 \pm 0.3$; $V_{max, \text{H}_2\text{O}, \text{dihydrogen}} = 4200 \pm 100 \text{ nmol min}^{-1} \text{ mg Av1}^{-1}$; $K_{m, \text{H}_2\text{O}, \text{dihydrogen}} = 4.6 \pm 0.4$; $V_{max, 51\% \text{D}_2\text{O}, \text{dihydrogen}} = 3500 \pm 100 \text{ nmol min}^{-1} \text{ mg Av1}^{-1}$; $K_{m, 51\% \text{D}_2\text{O}, \text{dihydrogen}} = 3.3 \pm 0.3$, where the units for K_m are defined in terms of the component ratio.

In Figure 4.3 (top left, black), the quantities of the deuterated ethylene isotopologues, $\text{C}_2\text{H}_3\text{D}$ and $\text{C}_2\text{H}_2\text{D}_2$, produced from acetylene reduction assays in 51% D_2O are plotted relative to the amount of all-hydrogen ethylene produced in the same assay, showing that the ratio of $\text{C}_2\text{H}_4 : \text{C}_2\text{H}_3\text{D} : \text{C}_2\text{H}_2\text{D}_2$ produced is $1 : 1.9 \pm 0.2 : 0.73 \pm 0.09$. If isotope discrimination by nitrogenase resembled a binomial distribution in which the probability of incorporating a hydrogen atom instead of a deuterium atom was $\frac{1}{2}$, we would expect a

1:2:1 ratio of products in a 50% D₂O solution. Therefore, the relative amounts of ethylene isotopologue products that we observe in an approximately 50% D₂O solution (51% D₂O) represent a slight depletion of deuterium into the products relative to the solvent. These data are the average of 20 trials performed at varying component ratios (Figure 4.3, top right, black and grey points, black cat-and-whisker plot). No significant difference in distribution of isotopologue products was observed upon variation of the component ratio, indicating that the rate of electron flow to the active site of the MoFe protein does not affect the isotope discrimination during reduction.

FTIR Spectroscopy was also used to quantify the results of acetylene reduction assays to confirm the quantification determined by GC-MS (Figure 4.3, top left, black squares; Figure 4.3, bottom right). Stretching frequencies at 943 cm⁻¹ and 843 cm⁻¹ were observed by FTIR in acetylene reduction assays performed with deuterium enrichment of the buffer, but not in assays without D₂O, corresponding to the presence of C₂H₃D and *cis*-C₂H₂D₂, respectively. The peak heights of the FTIR stretches were used to quantify the products as described in *Methods* and the distribution of ethylene isotopologues were 31 ± 1 % C₂H₄, 54 ± 1 % C₂H₃D, and 14 ± 2 % C₂H₂D₂, agreeing well with the results obtained by GC-MS. The FTIR stretch from *trans*-C₂H₂D₂ at 988 cm⁻¹ could not be observed, indicating that the levels of the *trans*-C₂H₂D₂ product were very low. Previous reports [22] have shown that, in 100% D₂O, nitrogenase makes about 96% *cis*-C₂H₂D₂ and only about 4% *trans*-C₂H₂D₂ which is consistent with the undetectable levels of *trans*-C₂H₂D₂ in the headspace of our assays.

In contrast to the results of acetylene reduction assays, proton reduction assays showed significant deuterium fractionation during H₂ production (Figure 4.3A, orange points and orange cat-and-whisker plot). Analogously to the acetylene reduction experiments, proton reduction assays were performed in either H₂O or 51% D₂O, and the products in the headspace were quantified by ¹H NMR. A 1:1:1 triplet corresponding to HD was observed at δ 4.82 ppm from assays in 51% D₂O that was absent in assays performed in 100% H₂O. Deuterium decoupling was employed to compress the triplet into a singlet for more accurate quantification of the HD peak (Figures 4.3D & B.6). The amount of HD relative to H₂ in the headspace of proton reduction assays of nitrogenase was quantified by NMR to be 0.5 ± 0.1 (5 replicates), indicating a significant depletion of deuterium in the products relative to the solvent. H₂ production during the acetylene reduction assays was not observed.

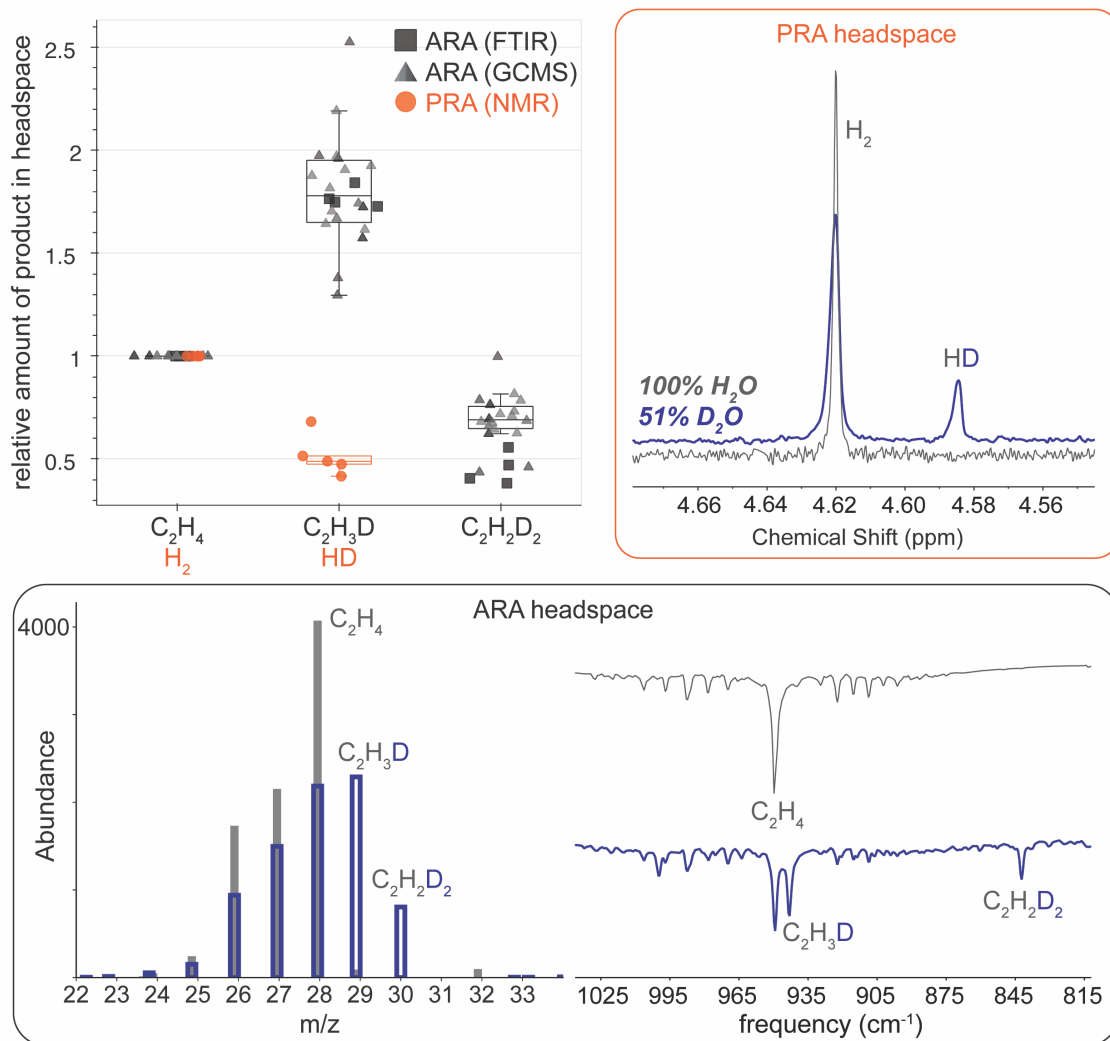


Figure 4.3: Quantification of isotopologue products of nitrogenase acetylene (ARA) and proton reduction assays (PRA) in 51% D_2O . Top left panel shows overlay of results of all assays (ARAs and PRAs) in 51% D_2O . The amount of deuterated product (C_2H_3D , $C_2H_2D_2$, or HD) is plotted relative to the amount of the all-hydrogen product (C_2H_4 or H_2). Small black and grey triangles are data from GC-MS quantification where each triangle is the result of quantification of one assay vial. The different shades of the triangles represent different component ratios (CRs) used in those assays (20 replicates, CR = 3-25). Black squares represent the data from assays quantified by FTIR (CR = 25, 4 replicates). Orange dots are the results of quantification of the products of proton reduction assays (CR = 15, 5 replicates). Representative 1H NMR spectra with deuterium decoupling of headspace from proton reduction assay in 100% H_2O (grey) or 51% D_2O (blue) shown in orange box. Representative GC-MS (left) and FTIR (right) of headspace of acetylene reduction assays in 100% H_2O (grey) or 51% D_2O (blue) are shown in the bottom panel.

Next, a proton inventory analysis was performed in which the deuterium enrichment was varied (25%, 51%, and 73% D₂O) and the relative amounts of isotopologue products were quantified (acetylene reduction: Tables B.1 & B.2; proton reduction: Table B.4). From the relative distribution of isotopologue products of acetylene and proton reduction assays, the isotope effects of hydrogen/deuterium addition were determined for these processes. Under conditions when a process involves two proton/deuteron transfer steps, each with the same isotope effect, the mole fraction of each of the isotopologue products can be expressed in terms of the isotope effect and the deuterium enrichment of the solvent by the following equations (see Appendix Section B.9 for derivation) [43, 44]:

$$X_{2H:0D} = \frac{IE^2 f_H^2}{(IE f_H + f_D)^2} \quad (4.1)$$

$$X_{1H:1D} = \frac{2IE f_D f_H}{(IE f_H + f_D)^2} \quad (4.2)$$

$$X_{0H:2D} = \frac{f_D^2}{(IE f_H + f_D)^2} \quad (4.3)$$

where $X_{2H:0D}$, $X_{1H:1D}$, and $X_{0H:2D}$ are the mole fractions of the isotopologue product with 2 Hs (C₂H₄ or H₂), 1 H and 1D (C₂H₃D or HD), or 2Ds (C₂H₂D₂ or D₂) incorporated, respectively. IE is the isotope effect of H/D addition (k_H/k_D), and f_H and f_D are the mole fractions of hydrogen and deuterium in the solvent, respectively. Least squares fits of the products of the acetylene reduction assays to Equations 4.1-4.3 results in three isotope effect values for each of the ethylene isotopologues (Figure B.11). The isotope effect parameters obtained from the least squares fits are shown in Table 4.1: 1.28 ± 0.04 , 1.4 ± 0.1 , and 1.59 ± 0.05 for C₂H₄, C₂H₃D, and C₂H₂D₂, respectively. Alternatively, we can calculate the total amounts of hydrogen vs. deuterium atoms incorporated into the ethylene products by the following equations:

$$X_D = \frac{1}{2} X_{C_2H_3D} + X_{C_2H_2D_2} \quad (4.4)$$

$$X_H = \frac{1}{2} X_{C_2H_3D} + X_{C_2H_4} \quad (4.5)$$

where X_D and X_H are the mole fractions of H vs. D incorporated into the reduced products. The mole fraction of deuterium incorporated (X_D) is related to the isotope effect by the following equation:

$$X_D = \frac{f_D^2 + IE f_D f_H}{(IE f_H + f_D)^2} \quad (4.6)$$

A least squares fit of Equation 4.6 to the experimental data from the acetylene reduction assays resulted in an isotope effect of 1.40 ± 0.05 , which agrees with the values obtained from the individual least squares fits of Equations 4.1-4.3 (Table 1, Figure B.12).

For the proton reduction assays, we were unable to quantify the relative amounts of D₂ by either GC-MS or NMR, so it is not possible to use equations 4.1-4.6 to obtain isotope effects for the proton reduction data. However, the ratio of H₂ to HD can be calculated from the data, and this ratio can be written in terms of the isotope effect and the deuterium enrichment of the solvent:

$$\frac{X_{H_2}}{X_{HD}} = \frac{IE^2 f_H^2}{(IE f_H + f_D)^2} \cdot \frac{(IE f_H + f_D)^2}{2IE f_D f_H} = \frac{IE f_H}{2f_D} \quad (4.7)$$

The isotope effects observed from proton reduction assays were much greater than those seen during acetylene reduction. The H₂ to HD ratio observed from proton reduction assays was 6.3 ± 0.6 in 25% D₂O, 1.9 ± 0.3 in 51% D₂O, and 0.9 ± 0.08 in 73% D₂O, which results in isotope effects of 4.2 ± 0.4 , 5.0 ± 0.4 , and 4.1 ± 0.7 , respectively. This product distribution indicates a significantly greater preference for H vs. D in proton reduction compared to acetylene reduction by nitrogenase. A least squares fit was performed on the experimental H₂/HD ratio of products observed against the deuterium enrichment of the solvent with Equation 4.7 and the isotope effect obtained from this fit was 4.2 ± 0.1 (Table 4.1, Figure B.13).

Models were also constructed with two distinct isotope effects for the two H/D atoms incorporated in ethylene/H₂; however, the least squares fits of the data to these models were indistinguishable from the aforementioned models with a single isotope effect for both H/Ds added, so only the latter values are reported.

In Figure 4.4, Equations 4.1-4.3 and 4.7 are used to plot the theoretical mole fraction of ethylene isotopologue products (left y-axis) and the theoretical H₂:HD ratio (right y-axis) as a function of the isotope effect. The experimental data for the relative amounts of isotopologues produced (y-axis) are shown as points at the IE (x-axis) where they intersect with their respective model, illustrating the significant difference between the isotope effect of proton reduction and acetylene reduction by nitrogenase. For the results of both the acetylene and proton reduction assays, the isotope effect value where the experimental mole fraction intercepts with the model does not vary with the level of deuterium enrichment of the solvent, indicating that the isotope effect is not affected by the level of deuterium enrichment of the solvent.

At all levels of deuterium enrichment studied, the isotope effect associated with acetylene reduction is within the range 1.3-1.6, which is similar to what is observed from secondary

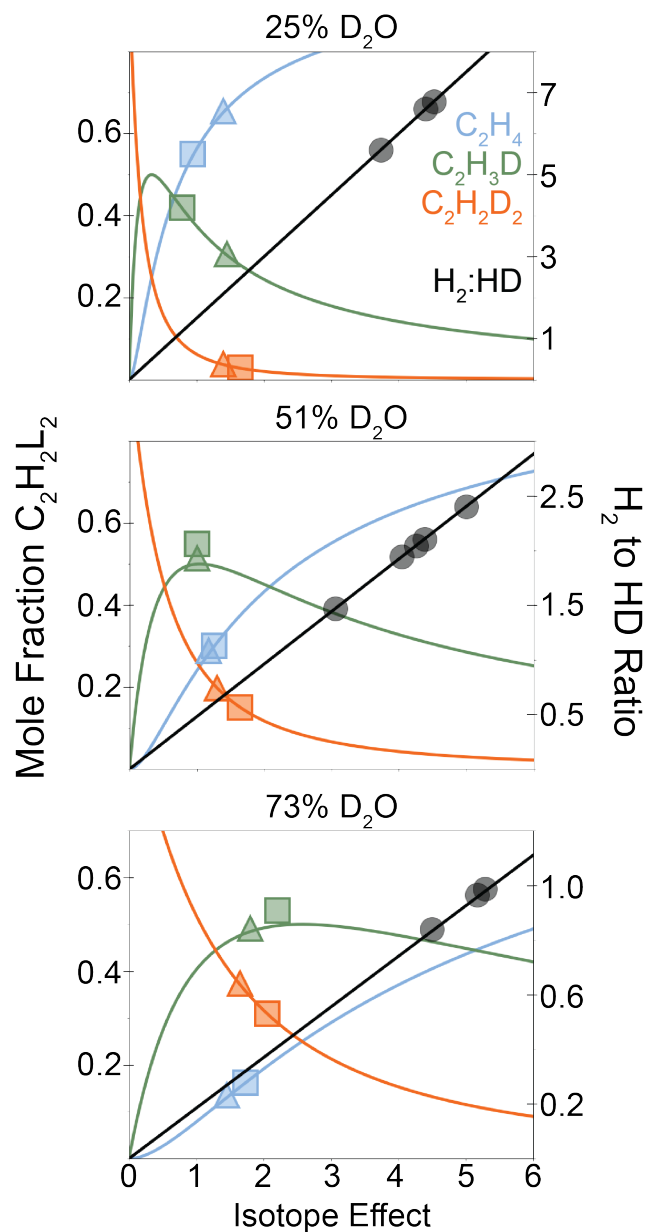


Figure 4.4: Proton inventory analysis of acetylene and proton reduction by nitrogenase. Results of all assays at 25 % D₂O (top), 51% D₂O (middle) and 73% D₂O (bottom) are shown as markers. Solid lines are plots of equations 4.1-4.3 and 4.7, the model expressions for mole fraction of isotopologue product as a function of IE. Markers are experimental data from the reduction assays with triangles and squares as the results of quantification of acetylene reduction assay products by GC-MS and FTIR, respectively. Circles are the ¹H NMR quantification of products of proton reduction assays. The blue, green, and orange line and markers are the model and experimental data for the mole fraction of C₂H₄, C₂H₃D, and C₂H₂D₂, respectively. The black line is the plot of Equation 4.7, the ratio of the mole fraction of H₂ to HD as a function of the IE and uses the right y-axis. The black circles are the experimental data from each proton reduction assay trial.

Table 4.1: Isotope Effects of Acetylene and Proton Reduction by Nitrogenase

	acetylene reduction			proton reduction	
	C ₂ H ₄	C ₂ H ₃ D	C ₂ H ₂ D ₂	X _D *	
IE	1.28 ± 0.04	1.4 ± 0.1	1.59 ± 0.05	1.40 ± 0.05	4.2 ± 0.1

* mole fraction of deuterium incorporated into products (X_D) calculated with Equation 4.4; this X_D value used to generate least squares fit of Equation 4.6 to calculate IE.

isotope effects and smaller than what is often observed for primary isotope effects [45]. For the proton reduction assay, the isotope effect was significantly larger at 4.2 ± 0.1 and also did not vary with deuterium enrichment. There is no significant exchange between the protons of ethylene or dihydrogen with water in the time scale of the assays (tested by analyzing the headspace at various time points up to one hour after quenching) so the isotopologue products in the headspace are an accurate reflection of the products of nitrogenase.

Cyanide Reduction

Similarly to the what was observed with proton and acetylene reduction, the rates of methane production in nitrogenase NaCN reduction assays were comparable in H₂O vs. 51% D₂O buffer (Figure 4.5). Therefore, no isotope effect could be determined from the relative amount of methane produced with and without deuterium enrichment of the solvent. Instead, the incorporation of deuterium into methane products was quantified and used to calculate an isotope effect associated with NaCN reduction.

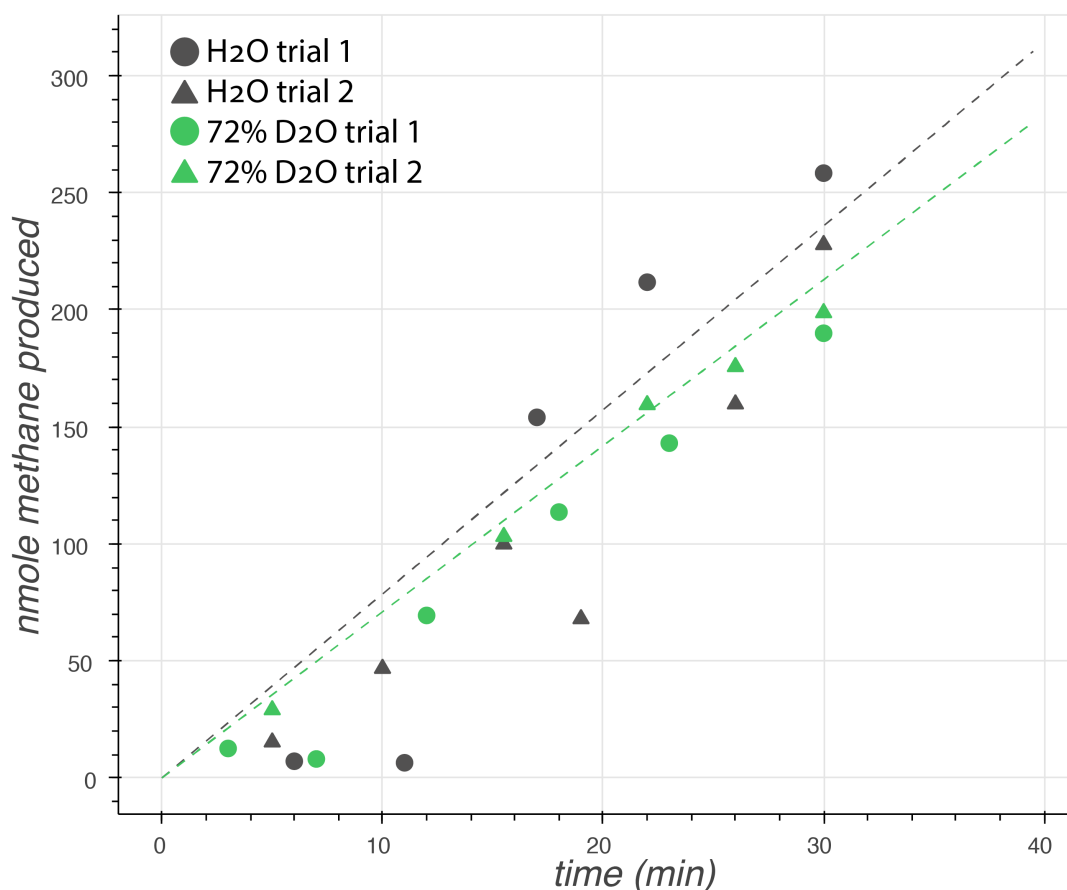


Figure 4.5: Time course of NaCN reduction assays in H₂O (grey) and 72% D₂O (green). Dashed lines are linear least squares fit to trial 2 from assays performed in H₂O (grey dashed, rate = 7.861 nmol methane produced min⁻¹) or 72% D₂O (green, rate = 7.095 nmol methane produced min⁻¹).

GC-MS was used to quantify methane isotopologue products of assays performed in 51% D₂O and 72% D₂O (Figure B.14). From assays performed in H₂O, the mass spectra of the methane peak in the gas chromatogram showed the greatest abundance at $m/z = 16$ corresponding to the expected molecular ion of methane. Abundance was also observed at

Table 4.2: Distribution of Methane Isotopologue Products from Nitrogenase Cyanide Reduction Assays in 51% and 72% D₂O

	CH ₄ (%)	CH ₃ D(%)	CH ₂ D ₂ (%)	CHD ₃ (%)	CD ₄ (%)
51% D ₂ O	38 ± 6	51 ± 6	6 ± 4	3.4 ± 0.6	0
72% D ₂ O	17 ± 2	38 ± 1	31 ± 2	11 ± 1	1.4 ± 0.8

$m/z = 15$ and $m/z = 14$ corresponding to the fragmentation of methane. These mass spectra peaks were also observed from assays performed in 51% D₂O, in addition to abundance at $m/z = 17$, $m/z = 18$, and $m/z = 19$, indicating the formation of CH₃D, CH₂D₂, and CHD₃ in addition to CH₄. From assays in 72% D₂O, abundance was also observed at $m/z = 20$ indicating the formation of CD₄. Overlapping mass spectra of the methane isotopologues were deconvoluted in an analogous manner to that used for ethylene isotopologues in order to calculate the relative levels of methane isotopologues produced. The results of all assays are shown in Figure 4.6 and reported in Table 4.2.

There is more uncertainty in calculating the isotope effect from the product isotopologue distribution for NaCN reduction than for the proton and acetylene reduction because the identity of the substrate, either HCN or DCN, is affected by the deuterium enrichment of the solvent. Therefore, the identity of one of the H/D atoms in the methane product is not due to an isotope effect of nitrogenase, but rather a function of the HCN:DCN ratio in solution. This ratio of HCN:DCN as a function of the deuterium enrichment of the solvent is not straightforward to calculate. The ratio of the dissociation constant of HCN to DCN has been reported to be 1.2 [46], which would suggest that the ratio of HCN/DCN will be less than the ratio of H₂O to D₂O in solution because DCN is more likely to form than HCN. However, at the pH in our assays, >95% of the cyanide species is in the protonated form, so it is unclear whether this difference in dissociation constant would lead to a significant difference between the HCN/DCN ratio and the H₂O/D₂O ratio. Therefore, in our models of mole fraction of methane isotopologues as a function of the isotope effect of H/D transfer, there is another variable x , which explains the probability of the substrate being HCN (instead of DCN), in addition to the same p and q variables defined in Appendix Section B.9 for the probability of nitrogenase incorporating an H vs. D during substrate reduction. The models are also complicated by the fact that the possible pathways for formation of a particular methane isotopologue are different whether the substrate is HCN or DCN. Figure B.15 outlines all possible pathways for generating all methane isotopologues from either HCN or DCN. For example, CH₃D can be formed by either 3 H additions to DCN or by the addition of 2 Hs and 1 D to HCN. The formation

of CH₃D from DCN is modeled by the expression $X_{CH_3D} = (1 - x)p^3$. The formation of CH₃D from HCN is more complicated because there are three permutations of the addition of 2Hs and 1D so the formation of this product is modeled by equation $X_{CH_3D} = 3xp^2q$. Therefore, the overall expression for the probability of formation of CH₃D is the sum of these models, $X_{CH_3D} = (1 - x)p^3 + 3xp^2q$. The expressions for the probability of forming each of the methane isotopologues are as follows:

$$X_{CH_4} = xp^3 \quad (4.8)$$

$$X_{CH_3D} = 3xp^2q + (1 - x)p^3 \quad (4.9)$$

$$X_{CH_2D_2} = 3xpq^2 + 3(1 - x)p^2q \quad (4.10)$$

$$X_{CHD_3} = xq^3 + 3(1 - x)pq^2 \quad (4.11)$$

$$X_{CD_4} = (1 - x)q^3 \quad (4.12)$$

where X_{CH_4} , X_{CH_3D} , $X_{CH_2D_2}$, X_{CHD_3} , and X_{CD_4} are the mole fractions of CH₄, CH₃D, CH₂D₂, CHD₃, and CD₄, respectively; x is the probability that the substrate is HCN, and p and q are the probabilities of incorporating an H or a D, respectively. The derivation and expressions for p and q are included in Appendix Section B.9.

Equations 4.8-4.12 are plotted in Figures 4.7 and 4.8 for the conditions where the mole fraction of deuterium in the solvent is 51% and 72% respectively, and x equals the mole fraction of H in the solvent. Under both deuterium enrichment conditions, the experimental data (horizontal lines) intercepts with the models at isotope effects ranging from 6-10. Although we don't have enough data to confidently report an isotope effect of H atom incorporation by nitrogenase during cyanide reduction (due to the uncertainty in x), there is clearly a significant normal isotope effect favoring hydrogen, resulting in considerable deuterium depletion in the methane products.

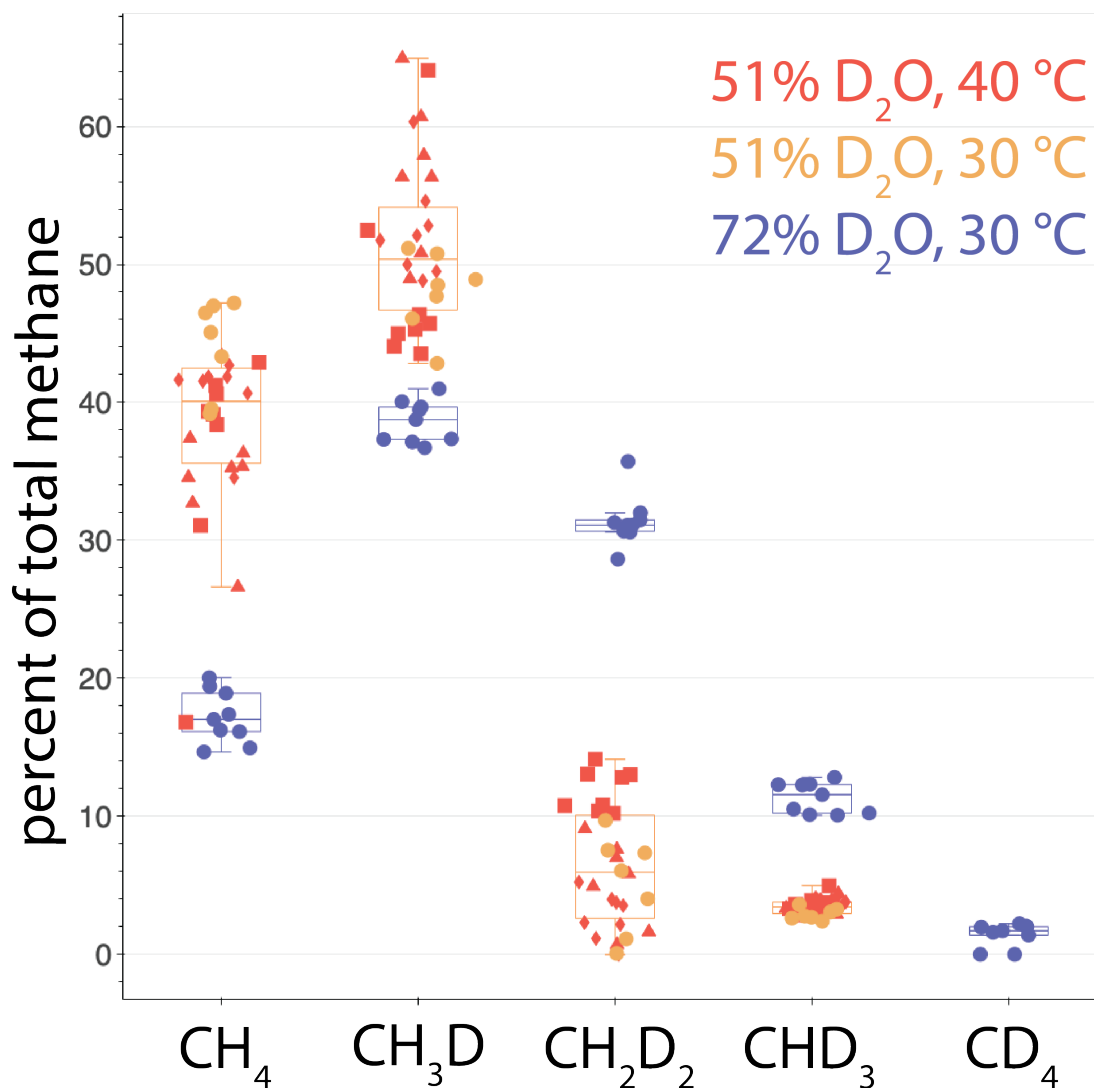


Figure 4.6: Distribution of methane isotopologue products from nitrogenase NaCN reduction assays in 51% D₂O (red and orange) and 72% D₂O (purple). Each point represents a single assay trial. Red points represent assays performed at 40 °C and the rest of the points represent assays performed at 30 °C. There was no significant difference in methane isotopologue distribution at 40 and 30 °C, so boxes representing mean and error for production of each isotopologue were generated from all 51% D₂O data. The data from the assays in 51% D₂O includes 22 different trials on 4 different days, with different shaped points representing assays on different days and the 72% D₂O data includes 9 trials on a single day.

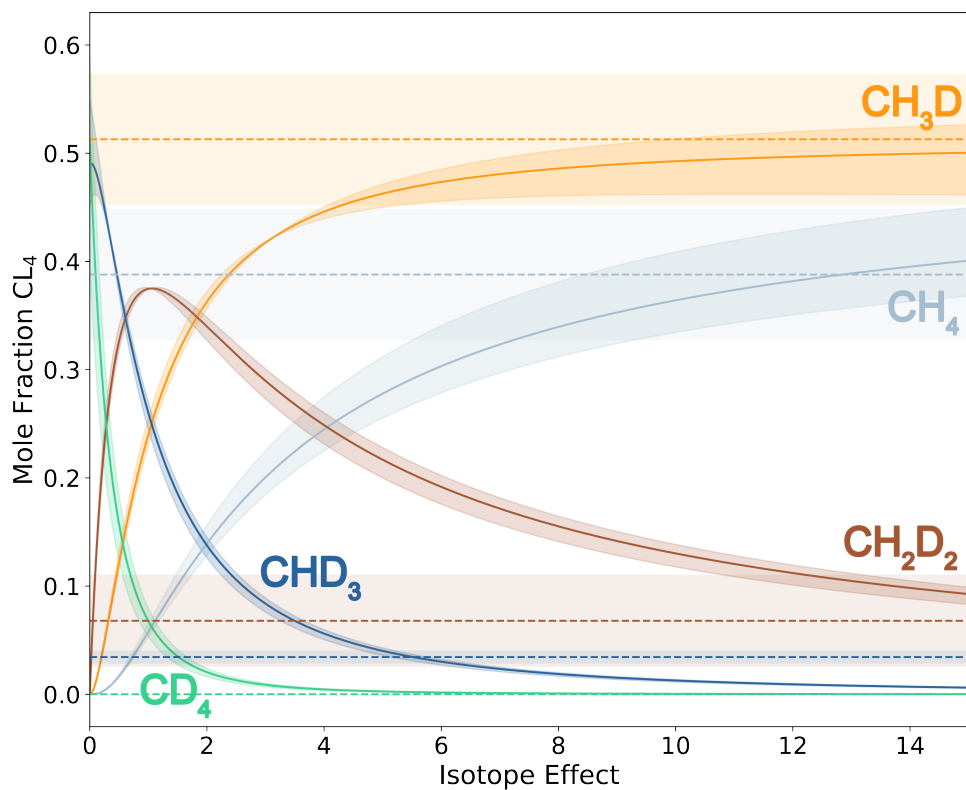


Figure 4.7: Models for the mole fraction of methane isotopologue product as a function of isotope effect in assays at 51% D₂O. Model functions (equations 4.8-4.12) plotted as solid line, with shading representing range in x (probability of substrate being HCN, instead of DCN) from 0.45 to 0.55. Experimental values for the relative amount of each methane isotopologue produced shown as dashed horizontal lines, with shading representing error in measurements.

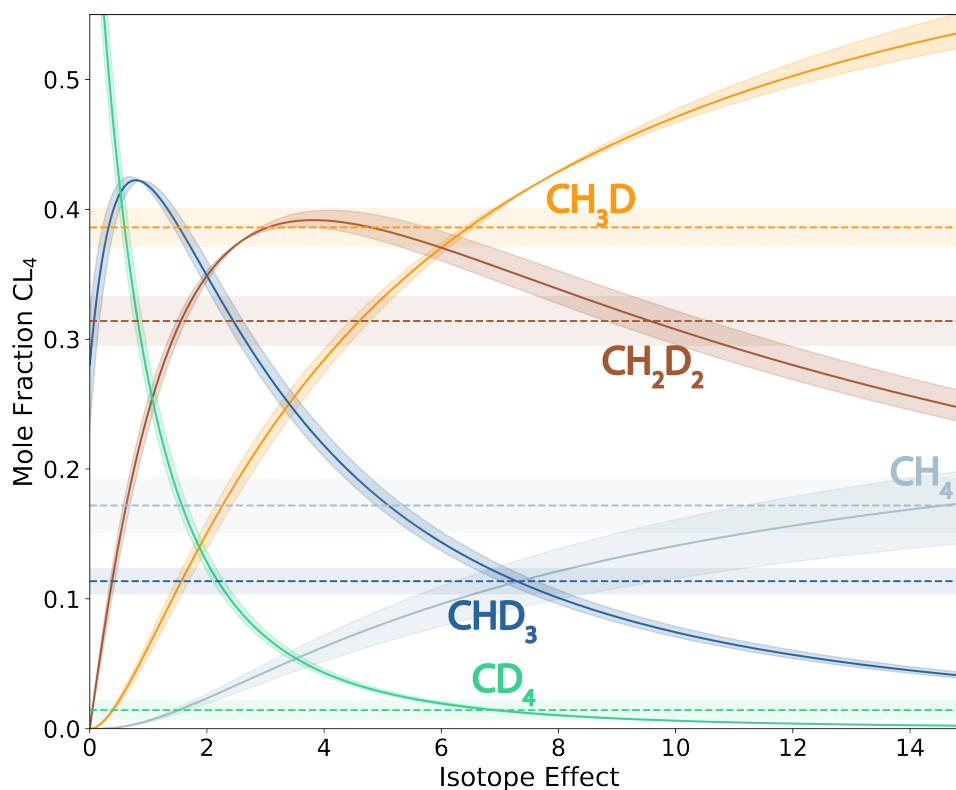


Figure 4.8: Models for the mole fraction of methane isotopologue product as a function of isotope effect in assays at 72% D_2O . Model functions (equations 4.8-4.12) plotted as solid lines, with shading representing range in x (probability of substrate being HCN, instead of DCN) from 0.23 to 0.32. Experimental values for the relative amount of each methane isotopologue produced shown as dashed horizontal lines, with shading representing error in measurements.

4.4 Conclusions and Future Outlook

In agreement with previous reports, our assays exhibited no significant solvent isotope effect on the specific activity of total substrate reduction by nitrogenase. This result is consistent with release of inorganic phosphate from ATP during the Fe protein cycle, rather than substrate reduction, being the rate limiting step of the nitrogenase mechanism [26]. This masking of the kinetic isotope effect at the active site by the slow electron transfer process has precluded the use of kinetic isotope experiments to probe the mechanism of nitrogenase in the past. However, because the reduction performed by nitrogenase is irreversible, an isotope effect can be determined from the extent of incorporation of

non-exchangeable deuterium into the products upon deuterium enrichment of the solvent.

We measured this H/D incorporation into products to determine the isotope effect associated with acetylene, proton, and cyanide reduction by Mo-nitrogenase from *A. vinelandii*. Various analytical chemistry techniques were used to accurately quantify the isotopologue products of these reactions. In acetylene reduction assays, there is a slight depletion of deuterium in the ethylene products, corresponding to an isotope effect of 1.40 ± 0.05 , whereas significant deuterium depletion is observed in proton reduction assays, with an isotope effect of 4.2 ± 0.1 . These results suggest that there are different mechanisms involved in proton transfer during the reduction of acetylene vs. protons and/or the proton source for these reductions is different. We did not collect enough data to report a precise isotope effect value for the reduction of cyanide; however, the preliminary results show that the isotope effect is likely greater than that of proton reduction, in the range of 6-10.

Our observations of the isotopic effects associated with dihydrogen production by nitrogenase are in general agreement with previous reports. A pioneering study by Hardy and coworkers quantified H₂, HD, and D₂ produced by partially-purified nitrogenase in varying mole fractions of D₂O in the solvent and our results are similar to what they observed [36]. They attributed the observed isotope effect to the depletion of deuterium in the L₃O⁺ ion; the reported ratio of H₃O⁺ to D₃O⁺ [47] in H₂O/D₂O mixtures agreed with the ratios of H to D in their products. Therefore, one interpretation of our results is that the isotope effect of proton reduction is a reflection of the fractionation of H₃O⁺/D₃O⁺ and not an effect intrinsic to the nitrogenase enzyme. A more recent report took a different approach to determining the kinetic isotope effect of H₂ production by eliminating the need for the slow steps of the Fe protein that mask the kinetic isotope effects at the active site. In this work, the MoFe protein was immobilized on an electrode surface and directly reduced with the aid of a redox mediator [48]. By measuring the catalytic current of H₂ production in varying levels of D₂O enrichment in the buffer, a kinetic isotope effect of about 2.7 was calculated. The kinetic isotope effect of about 2.7 observed from electrocatalysis of MoFe protein was attributed to the movement of a single hydron toward the transition state; specifically the heterolytic cleavage of a proton/deuteron on one of the sulfurs of the cofactor to protonate a hydride/deuteride bridging two irons of the cofactor. The zero point energy of bonds to deuterium are lower than that of bonds to hydrogen and the reactant state of the cluster has two deuterium/hydrogens bound while the transition state has only the bridging hydride/deuteride bound. Therefore, upon isotopic substitution, the ground state energy of the reactant state decreases more than that of the transition state, causing an increase in the activation energy and thus, imparting a kinetic isotope effect. An isotope

effect for H₂ evolution by nitrogenase was also observed spectroscopically by irradiation of the FeMo-cofactor (with 4 H atoms bound) at 450 nm. This photoinduced reductive elimination of H₂ and subsequent oxidative addition of H₂ upon annealing showed large kinetic isotope effects of about 10 and 5, respectively; interpreted as evidence that both processes involve an energy barrier and that hydrogen tunneling could be involved [19, 49].

In other reports measuring deuterium fractionation into dihydrogen by cyanobacteria [50] or purified hydrogenases [32] significant depletion of deuterium was also observed. When we convert our isotope effect values to fractionation factors (see Appendix Section B.11 and Table B.4) our results are comparable to these studies on hydrogenases, which could indicate that deuterium depletion is a common feature of H₂ production.

To our knowledge, the only previous report investigating deuterium incorporation from the solvent during the reduction of acetylene by nitrogenase was performed in 100% D₂O buffer and the products of this assay were 96% *cis*-C₂H₂D₂ and 4% *trans*-C₂H₂D₂; however, no isotope effects were measured in these studies [22].

Similar to our cyanide reduction results, a large hydrogen isotope effect was also observed for methane production (from CO₂) by the V- and Fe-only nitrogenases in *Rhodospseudomonas palustris*. The hydrogen isotope fractionation that they observed was the largest ever reported for any biogenic and geogenic methane evolution pathway. Interestingly, the ¹³C fractionation observed from methane production by this organism was more modest and within the range of other microbial methanogenesis. There are significant differences between our studies and this report including the fact that they measured *in vivo* fractionation (from a different organism than *A. vinelandii*) and the substrate of their methanogenesis is CO₂ (instead of NaCN). However, these reports suggest that deuterium depletion could be a common feature of methane production by nitrogenase.

When the ultimate source of H atoms is the bulk water, as is the case with nitrogenase, solvent isotope experiments in which H₂O is substituted with D₂O can reveal information about the intermediate states of the H atoms between their presence in the bulk water to their incorporation in the final reduced product. Our observation that the solvent kinetic isotope effects of acetylene reduction and proton reduction are different suggests that the identities of the H atoms on the path toward these two products are different. There is precedent for this in the observation that pH-rate profiles for acetylene and proton reduction are shifted relative to each other [51]. The H atoms in nitrogenase products could be derived from H₂O, H₃O⁺, or hydrides on the Fe-Mo-cofactor. If H atoms are sourced directly from H₂O, with no isotope effect of H atom transfer, the deuterium enrichment of

the product would reflect the deuterium enrichment of the solvent and would thus result in a isotope effect close to unity. As mentioned previously, protons from H_3O^+ will result in products depleted in deuterium with an isotope effect consistent with the difference in pK_a between H_2O and D_2O . More generally, the substitution of D for H typically shifts the pK values by 0.5 units, and so a similar isotope effect might be expected for proton donation from an amino acid side chain [52].

Hydrides on the FeMo-cofactor will likely also exhibit an isotope effect. In a synthetic FeFe complex with a terminal thiolate ligand and a bimetallic center, similar to the FeMo-cofactor, H/D exchange between the bridging hydride and the proton on the sulfur was studied [53]. This report found that H/D exchange between the protonated sulfur and the solvent was fast because the thiol is acidic, while the H/D exchange on the hydride was slow. The K_{eq} of the interconversion of the complex with deuterium at the hydride position and hydrogen on the sulfur to the complex with hydrogen at the metal hydride position and deuterium on the sulfur was measured to be 2.36, indicating that a 50% D_2O solution will produce complexes in which 70% of the bridging metal hydrides are occupied by hydrogen and 30% are occupied by deuterium.

If the large isotope effect we see from proton reduction is due to fractionation of deuterium in D_3O^+ or on the metal hydrides of the FeMo-cofactor, we are left with the interesting question of why we only observe a modest isotope effect from acetylene reduction. Our results could suggest that the bridging hydrides play a relatively small role in the reduction of acetylene or that the protons involved in acetylene reduction are sourced from H_2O (instead of H_3O^+).

Clearly, more experiments are needed to make strong mechanistic conclusions from the product deuterium isotope effects of acetylene and proton reduction by nitrogenase; however these results open the door to a novel approach for learning about the nitrogenase mechanism. Previous studies have shown that the V- and Fe- nitrogenases incorporate less ^{15}N than the Mo-nitrogenase when fixing nitrogen [54] so it will be interesting to explore if these alternative nitrogenases have different deuterium fractionation properties as well. Future studies will include investigating other substrates of nitrogenase and the effect of competing substrates on the deuterium fractionation. Investigating the isotope effect of proton reduction in the absence and presence of dinitrogen will shed light on the interesting connection between these two substrates. Preliminary experiments toward this end show no significant difference in deuterium fractionation with and without N_2 (see section B.8, Table B.3); however, these experiments are being refined and approached with more precise analytical techniques. The use of product deuterium isotope effect experiments

will add a new dimension to the previous explorations of nitrogenase enzymatic activity and deepen our understanding of the complex reactions at the active site.

References

- (1) Buscagan, T. M.; Rees, D. C. *Joule* **2019**, *3*, 2662–2678.
- (2) Jia, H. P.; Quadrelli, E. A. *Chem. Soc. Rev.* **2014**, *43*, 547–564.
- (3) Gruber, N.; Galloway, J. N. *Nature* **2008**, *451*, 293–296.
- (4) Sharma, L. K.; Bali, S. K. *Sustainability* **2017**, *10*.
- (5) Smith, C.; Hill, A. K.; Torrente-Murciano, L. *Energy Environ. Sci* **2020**, *13*, 331.
- (6) Seefeldt, L. C.; Yang, Z. Y.; Lukoyanov, D. A.; Harris, D. F.; Dean, D. R.; Raugei, S.; Hoffman, B. M. *Chem. Rev.* **2020**, *120*, 5082–5106.
- (7) Einsle, O.; Rees, D. C. *Chem. Rev.* **2020**, *120*, 4969–5004.
- (8) Spatzal, T.; Aksoyoglu, M.; Zhang, L.; Andrade, S. L.; Schleicher, E.; Weber, S.; Rees, D. C.; Einsle, O. *Science* **2011**, *334*, 940.
- (9) Alberty, R. A. *J. Biol. Chem* **1994**, *269*, 7099–7102.
- (10) Simpson, F. B.; Burris, R. H. *Science* **1984**, *224*, 1095–1097.
- (11) Howard, J. B.; Rees, D. C. *Chem. Rev.* **1996**, *96*, 2965–2982.
- (12) Hageman, R. V.; Burris, R. H. *Proc. Natl. Acad. Sci. USA* **1978**, *75*, 2699–2702.
- (13) Danyal, K.; Dean, D. R.; Hoffman, B. M.; Seefeldt, L. C. *Biochemistry* **2011**, *50*, 9255–9263.
- (14) Jasniewski, A. J.; Sickerman, N. S.; Hu, Y.; Ribbe, M. W. *Inorganics* **2018**, *6*, 1–14.
- (15) Tezcan, F. A.; Kaiser, J. T.; Mustafi, D.; Walton, M. Y.; Howard, J. B.; Rees, D. C. *Science* **2005**, *309*, 1377–1380.
- (16) Thorneley, R. N. F.; Lowe, D. J. *Biochem. J* **1984**, *224*, 887–894.
- (17) Lowe, D. J.; Thorneley, R. N. F. *Biochem. J* **1984**, *224*, 877–886.
- (18) Borden, W. T. *Journal of Physical Chemistry A* **2017**, *121*, 1140–1144.
- (19) Lukoyanov, D.; Khadka, N.; Yang, Z.-Y.; Dean, D. R.; Seefeldt, L. C.; Hoffman, B. M. *J. Am. Chem. Soc.* **2016**, *138*, 10674–10683.
- (20) Newton, J. W.; Wilson, P. W.; Burris, R. H. *J. Biol. Chem* **1953**, *204*, 445–451.
- (21) Burgess, B. K.; Wherland, S.; Newton, W. E.; Stiefe, E. J. *Biochemistry* **1981**, *20*, 5140–5146.
- (22) Han, J.; Newton, W. E. *Biochemistry* **2004**, *43*, 2947–2956.
- (23) Lee, H. I.; Sørliie, M.; Christiansen, J.; Song, R.; Dean, D. R.; Hales, B. J.; Hoffman, B. M. *J. Am. Chem. Soc.* **2000**, *122*, 5582–5587.

- (24) Sra, A. K.; Hu, Y.; Martin, G. E.; Snow, D. D.; Ribbe, M. W.; Kohen, A. *J. Am. Chem. Soc.* **2004**, *126*, 12768–12769.
- (25) Schowen, K. B. J. In *Transition States of Biochemical Processes*, 1978, pp 225–283.
- (26) Yang, Z. Y.; Ledbetter, R.; Shaw, S.; Pence, N.; Tokmina-Lukaszewska, M.; Eilers, B.; Guo, Q.; Pokhrel, N.; Cash, V. L.; Dean, D. R.; Antony, E.; Bothner, B.; Peters, J. W.; Seefeldt, L. C. *Biochemistry* **2016**, *55*, 3625–3635.
- (27) Fuchslkhan, W. H.; Hardy, R. W. F. *Bioinorg. Chem.* **1972**, *1*, 195–213.
- (28) Amyes, T. L.; Richard, J. P. *Methods in Enzymology* **2017**, *596*, 163–177.
- (29) Tsang, W.-Y.; Richard, J. P. *J. Am. Chem. Soc.* **2007**, *129*, 10330–10331.
- (30) Kolmar, S. S.; Mayer, J. M. *J. Am. Chem. Soc.* **2017**, *139*, 10687–10692.
- (31) Luxem, K. E.; Leavitt, W. D.; Zhang, X. *Appl. Environ. Microbiol.* **2020**, *86*, 00849–20.
- (32) Yang, H.; Gandhi, H.; Cornish, A. J.; Moran, J. J.; Kreuzer, H. W.; Ostrom, N. E.; Hegg, E. L. *Rapid Communications in Mass Spectrometry* **2016**, *30*, 285–292.
- (33) Löffler, M.; Kümmel, S.; Vogt, C.; Richnow, H. H. *Front. Microbiol.* **2019**, *10*.
- (34) Yang, H.; Gandhi, H.; Shi, L.; Kreuzer, H. W.; Ostrom, N. E.; Hegg, E. L. *Rapid Commun. Mass Spectrom.* **2012**, *26*, 61–68.
- (35) Zhang, X.; McRose, D. L.; Darnajoux, R.; Bellenger, J. P.; Morel, F. M.; Kraepiel, A. M. *Biogeochemistry* **2016**, *127*, 189–198.
- (36) Jackson, E. I.; Parshall, G. W.; Hardy, R. W. F. *J. Biol. Chem.* **1968**, *243*, 4952–4958.
- (37) Burgess, B. K.; Lowe, D. J. *Chem. Rev.* **1996**, *96*, 2983–3011.
- (38) Barbara Schowen, K.; Schowen, R. L. *Meth. Enzymol.* **1982**, *87*, 551–606.
- (39) Spatzal, T.; Perez, K. A.; Einsle, O.; Howard, J. B.; Rees, D. C. *Science* **2014**, *345*, 1620–1623.
- (40) Lin-Vien, D.; Fateley, W. G.; Davis, L. C. *App. Environ. Microbiol.* **1989**, *55*, 354–359.
- (41) Benton, P. M.; Christiansen, J.; Dean, D. R.; Seefeldt, L. C. *J. Am. Chem. Soc.* **2001**, *123*, 1822–1827.
- (42) Fisher, K.; Dilworth, M. J.; Kim, C. H.; Newton, W. E. *Biochemistry* **2000**, *39*, 10855–10865.
- (43) Khushvakov, J.; Nussbaum, R.; Cadoux, C.; Duan, J.; Stripp, S. T.; Milton, R. D. *Angew. Chem. Int. Ed.* **2021**, *60*, 10001–10006.
- (44) Spencer, R. W.; Daniels, L.; Fulton, G.; Orme-Johnson, W. H. *Biochemistry* **1980**, *19*, 3678–3683.

- (45) Caldwell, R. A.; Misawa, H.; Healy, E. F.; S Dewar, M. J.; Riel, v. *J. Chem. Soc., Chem.* **1987**, *109*, 6869–6870.
- (46) Reenstra, W. W.; Abeles, R. H.; Jencks, W. P. *J. Am. Chem. Soc.* **1982**, *104*, 1016–1024.
- (47) Lumry, R.; Smith, E. L.; Glantz, R. R. *J. Am. Chem. Soc.* **1951**, *73*, 4330–4340.
- (48) Khadka, N.; Milton, R. D.; Shaw, S.; Lukoyanov, D.; Dean, D. R.; Minter, S. D.; Raugei, S.; Hoffman, B. M.; Seefeldt, L. C. *J. Am. Chem. Soc.* **2017**, *139*, 13518–13524.
- (49) Lukoyanov, D.; Yang, Z. Y.; Duval, S.; Danyal, K.; Dean, D. R.; Seefeldt, L. C.; Hoffman, B. M. *Inorg. Chem.* **2014**, *53*, 3688–3693.
- (50) Luo, Y.-H.; Sternberg, L.; Suda, S.; Kumazawa, S.; Mitsui, A. *Plant Cell Physiol.* **1991**, *32*, 897–900.
- (51) Pham, D. N.; Burgess, B. K. *Biochemistry* **1993**, *32*, 13725–13731.
- (52) Schowen, K. B.; Schowen, R. L. *Meth. Enzymol.* **1982**, *87*, 551–606.
- (53) Yu, X.; Pang, M.; Zhang, S.; Hu, X.; Tung, C. H.; Wang, W. *J. Am. Chem. Soc.* **2018**, *140*, 11454–11463.
- (54) McRose, D. L.; Lee, A.; Kopf, S. H.; Baars, O.; Kraepiel, A. M.; Sigman, D. M.; Morel, F. M.; Zhang, X. *Geochim. Cosmochim. Acta* **2019**, *244*, 12–23.

*Chapter 5***CHARACTERIZATION OF METAL CONTENT AND ATPASE
ACTIVITY OF HOLO- AND APO-AV2 PROTEINS OF
NITROGENASE (IN COLLABORATION WITH AILIENA
MAGGIOLO)****5.1 Introduction**

Although pursuits probing the mechanism of nitrogenase often focus on the MoFe protein (Av1), which houses the unique active site, the Fe protein (Av2) also contains immense complexity and there are many unanswered questions about this component of the nitrogenase enzyme. In addition to its most-cited role as the obligate reductase to the MoFe protein during substrate reduction, the Fe protein is also required for maturation of both metalloclusters on the MoFe component protein, the FeMo-cofactor and the P-cluster [1]. The Fe protein is a homodimer with a 4Fe-4S cluster coordinated at the dimer interface and one MgATP binding site per monomer and both of these cofactors are integral to the protein's role as a reductase during turnover [2].

The activity of the Fe protein as obligate reductase during turnover is often termed the "Fe protein cycle" and it begins with reduction of the 4Fe-4S cluster of the Fe protein by ferredoxins and flavodoxins in the cell. The reduced Fe protein then binds to the MoFe and hydrolyzes two ATP, which causes the transfer of one electron from the 4Fe-4S cluster of the Fe protein to the P cluster (and ultimately to the active site) of the MoFe protein. The oxidized, ADP-bound Fe protein then dissociates from the MoFe protein and is re-reduced. Several of these Fe-protein cycles are required to build up reducing equivalents on the active site FeMo-cofactor in order for substrates to bind and be reduced [1, 3].

In its role supporting maturation of the FeMo-cofactor, the Fe protein participates in the insertion of molybdenum and homocitrate onto a 8Fe-9S precursor bound to the FeMo-cofactor biosynthesis scaffold complex NifEN and is also required for the ultimate insertion of the mature FeMo-co onto NifDK (Av1) [4]. The Fe protein supports P-cluster maturation in an "*in situ*" role; that is, the P-cluster is already bound to its appropriate coordination site in the MoFe protein before the Fe protein gets involved in the maturation process. In this process, it is plausible that the Fe protein plays a reductase role, delivering an electron to a precursor to the P-cluster, which leads to the formation of the final active P-cluster; however, much is still unknown about this process [5].

ATP hydrolysis by the Fe protein is an important subject of study because it is not only required for the Fe protein's role as the obligate reductase during substrate turnover, but also for its role supporting maturation of the FeMo-cofactor. During turnover, ATP hydrolysis causes a conformational change that positions the 4Fe-4S cluster of the Fe protein even closer to the exterior of the enzyme and closer to the P-cluster of the MoFe protein, facilitating electron transfer between these Fe-S clusters [3]. After electron transfer and dissociation of the Fe protein from the MoFe protein, phosphate release from the Fe protein is the rate limiting step of the overall reduction mechanism of nitrogenase [6]. Additionally, ADP is strongly inhibiting to the activity of the Fe protein, and thus inhibits substrate reduction by the nitrogenase complex, which results in the requirement of an ATP regeneration system for activity assays of the nitrogenase complex.

In addition to the MgATP binding/hydrolysis site, the other key feature of the Fe protein is the redox-active 4Fe-4S cluster. The Howard group observed that the 4Fe-4S cluster of the reduced Fe protein could be chelated by α, α' -dipyridyl, but only in the presence of MgATP; concluding that the conformational change induced by ATP hydrolysis caused the 4Fe-4S cluster to be more surface exposed [7]. When the *oxidized* Fe protein was treated with this chelator, with or without MgATP, the 4Fe-4S cluster was removed in a biphasic process, the initial step of which left an intermediate reminiscent of a 2Fe-2S ferredoxin cluster which was then completely removed [8]. A physiological role has been suggested for the apo-Fe protein; however, there has been no clear evidence that the 4Fe-4S cluster is indispensable for the reductase and cluster maturation/insertion roles of the Fe protein.

These two key features of the Fe protein, coordination of the 4Fe-4S cluster and MgATP hydrolysis, are explored in this chapter by measuring the ATP hydrolysis of an apo-form of the Fe protein. Ailiena Maggiolo has discovered a novel form of the apo-Fe protein, generated under crystallization conditions (Figure 5.1). Maggiolo has solved the crystal structure of this apo-Fe protein, revealing that no iron sulfur cluster is present and that the dimer adopts an orientation that hasn't been seen before in any other structures of the Fe protein. In relation to the structure of holo-Av2, the dimer of this apo-form is rotated $\sim 30^\circ$ about the nucleotide binding position and the loops that normally coordinate the 4Fe-4S cluster are disordered. Even with these extreme differences in orientation of the dimer between the apo- and holo- forms of Av2, the nucleotide binding site of the apo-form is still intact and very similar to that of holo-Av2. The discovery of this new form of the apo-Fe protein led us to investigate the metal-binding and ATPase activity of the enzyme.

The most common method for quantifying ATPase activity is the use of a colorimetric assay which involves a color change upon reaction of the free phosphate with a reagent in

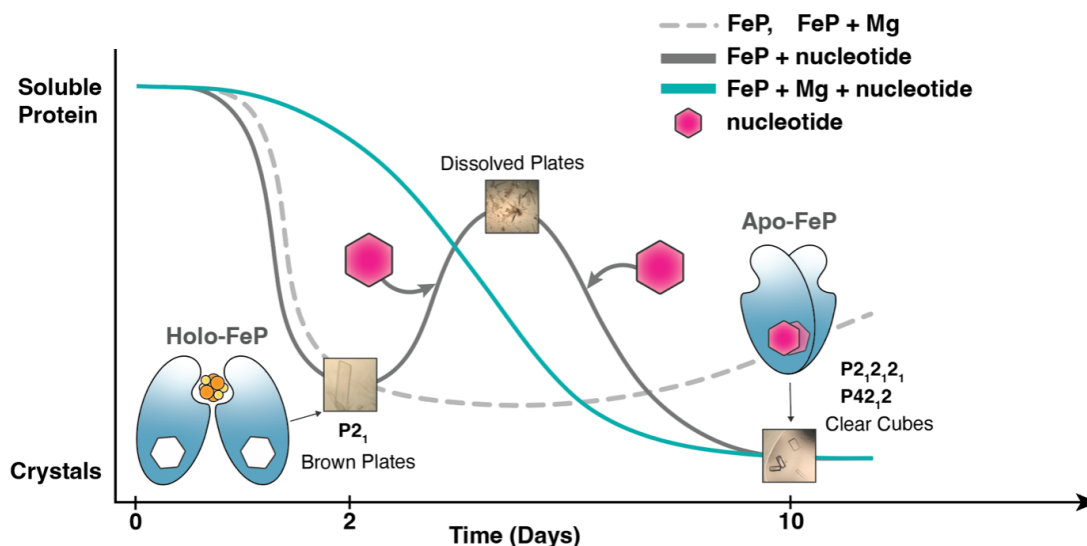


Figure 5.1: Figure courtesy of Ailiena Maggiolo. Schematic of crystallization kinetics to demonstrate apoFeP crystals form by co-crystallization of holoFeP with nucleotide. HoloFeP alone or holoFeP co-crystallized with MgCl_2 form brown plate-like crystals within 2 days. These crystals were determined to have spacegroup symmetry $P2_1$ and contain FeP with an intact $4\text{Fe}4\text{S}$ cluster. HoloFeP that was co-crystallized with ATP or MgATP first formed brown plate-like crystals after 2 days, then spontaneously dissolved back into the crystal drop solution. After ~ 1 week, new crystals appeared which were clear and cube-shaped. These crystals were determined to have spacegroup $P2_1(2_1)2_1(1)$ or $P4_2(1)2$. Both crystal forms had FeP which was lacking the $4\text{Fe}4\text{S}$ cluster and had ADP bound.

the assay. This color change is then measured spectroscopically to quantify the amount of free phosphate released by ATP hydrolysis. Although these phosphate quantification kits have been optimized and many of them are commercially available, they are incompatible with the Fe protein assays because the ATP regeneration system interferes with the P_i quantification assay components and we observed a large background from the ATP regeneration system alone when we attempted phosphate quantification by these assays. Another method to measure ATPase activity is to use ^{32}P -labeled ATP and quantify $^{32}\text{P}_i$ with a phosphorimager, which is an extremely sensitive technique but comes with the safety hazards and the complexities of using a radioactive reagent [9]. By the suggestion of Prof. Jim Howard, we attempted direct quantification of free phosphate by ion chromatography and have developed a new protocol for sensitive and straightforward quantification of P_i release by the Fe protein. This method is superior to previous methods for quantifying ATPase activity because after completion of the assay, no additional reagents are required and the sample only needs to be diluted before subjected to the automated sample injection

system of the ion chromatography instrument.

In this chapter, we first characterized the stoichiometry of Fe binding to the novel form of the apo-Fe protein by accurate metal and protein quantification by ICP-MS and amino acid analysis, respectively. We then measured the rate of ATP hydrolysis by the holo- and apo-Fe protein using ion chromatography. Significantly, we observed robust ATPase activity by the apo-Fe protein, which to our knowledge has not been previously reported.

5.2 Methods

Amino acid analysis of holo- and apo- Av2

Samples of holo- and apo-Av2 in 5mM DT SEC buffer (50 mM Tris/HCl pH 7.5, 200 mM NaCl, 5 mM dithionite) were sent to the UC Davis Molecular Structure Facility for amino acid analysis on the L-8800 Hitachi analyzer with a lithium citrate buffer system. Holo-Av2 samples were sent as-purified and apo-Av2 samples were generated by a crystallography method developed by Maggiolo (Figure 5.1). Briefly, crystals of apo-Av2 were redissolved by depositing 5 mM DT SEC on the crystal slide. Then the solution was retrieved by pipetting and buffer exchanged into 5 mM DT SEC to remove the crystallization components. The concentration of the Av2 samples determined by amino acid analysis are shown in Table 5.1.

Table 5.1: Concentration of Av2 Samples Determined by Amino Acid Analysis

apo Av2 batch 1	apo Av2 batch 2	holo Av2
4.74 mg/mL	3.40 mg/mL	18.36 mg/mL

Metal analysis of Holo-Av2, Apo-Av2, and Av1 by Inductively Coupled Plasma Mass Spectrometry

Apo Av2 samples (10 μ L) and Holo Av2 samples (2.5 μ L) were diluted into 5 mM DT SEC (final volume 100 μ L) in the anaerobic chamber. Samples were removed from the anaerobic chamber, 70% nitric acid was added (285 μ L) and samples were placed at 50 $^{\circ}$ C for 2 hr. All samples were added to 5.615 mL of milliQ water in plastic Falcon tubes with 4 rounds of rinsing (1 mL milliQ water used for each rinse) for a final volume of 10 mL in each Falcon tube. ICP-MS was performed on Helium mode and O₂ mode using a Hewlett-Packard 4500 ICP mass spectrometer (Agilent Technologies) with a CETAC ASX-500 autosampler (CETAC) at the Caltech Resnick Water and Environment Lab.

Measurement of ATPase Activity of Holo- and Apo-Av2 by Ion Chromatography

Nitrogenase ATP assays were conducted anaerobically under an Ar atmosphere (<3% H₂) in an aqueous solution (50 mM Tris-HCl pH 7.8, 100 μ L reaction volume) using 96 well plates. Using the protein concentrations determined by amino acid analysis, equimolar stock concentration of holo- and apo-Av2 were prepared (0.32 mg/mL for a final concentration in assay of 0.08 mg/mL). Either holo-Av2 or apo-Av2 were added to solution of either 2.912 mg/mL Av1 (CR = 0.05) or 0.5824 mg/mL Av1 (CR = 0.25) in the presence of an ATP regeneration system (12 mM creatine phosphate, 5 mM ATP, 5 mM MgCl₂, 19 units kinase) and 20 mM dithionite. Each well was a single time point, and at the appropriate time, 25 μ L of 400 mM EDTA (pH 7.8) was added to quench the reaction. Control conditions included omission of everything except buffer and ATP ("ATP only"), omission of everything except buffer, creatine phosphate and Mg-ATP ("no protein"), omission of both nitrogenase components ("ATP regeneration system"), and each of the nitrogenase components on their own with the ATP regeneration system ("Av1 alone", "holo-Av2 alone", and "apo-Av2 alone"). After completion of the assays, the samples were diluted 20x (50 μ L into 1 mL) in milliQ water and subject to ion chromatography on a Thermo Scientific Dionex Integrion HPIC with a Dionex VWD. An isocratic method was run on a method and eluents were detected by absorbance at 214 nm. Phosphate was calculated with a standard curve generated by phosphate standards.

5.3 Results

Aliquots of holo-Av2 and apo-Av2 were split, with part of the sample subject to amino acid analysis, part of the sample subject to ICP-MS, and the rest of the sample frozen for future ATPase assays. This workflow allowed for precise determination of the concentration of Fe protein and the stoichiometry of Fe bound to the protein before measurement of the ATP hydrolysis rates of the enzymes (Table 5.2). The iron quantification in He vs. O₂ mode agree within error. There were slightly more than 4 Fe per Av2 dimer in the holo-Av2 sample, consistent with the coordination of a 4Fe-4S cluster and suggesting that some Fe is bound adventitiously or there are contaminating proteins with Fe-cofactors. The iron quantification of both apo-Av2 samples agrees within error, equivalent to about 2 Fe atoms per Av2 dimer.

Table 5.2: Ratio of Fe atoms to Av2 Dimers in Holo- and Apo-Av2 samples

Sample	Fe:Av2 dimer (He)	Fe:Av2 dimer (O ₂)
apo Av2 batch 1	2.5 \pm 0.3	2.1 \pm 0.3
apo Av2 batch 2	2.1 \pm 0.3	1.8 \pm 0.3
holo Av2	5.3 \pm 0.6	4.4 \pm 0.5

Ion chromatography was successfully utilized to measure the ATPase activity of holo-Av2 and apo-Av2 by directly measuring the concentration of inorganic phosphate in solution (released after ATP hydrolysis by Av2). Figure 5.2 shows the results of all ATPase assays with nitrogenase components or only the ATP regeneration system. Figures 5.3 and 5.4 focus on the conditions of low component ratio (0.05) and high component ratio (0.25) respectively, where the component ratio is defined as moles Av2 dimer per mole Av1 active site (with 2 active sites per Av1 tetramer). Because it is known that the presence of Av1 is required for Av2 ATPase activity and we were interested in measuring the rate of ATP hydrolysis by Av2, we chose component ratios that saturated Av2 with Av1. At the higher component ratio of 0.25, there are 2 Av1 tetramer per Av2 and at the lower component ratio of 0.05, there are 10 Av1 tetramer per Av2. As expected we observed ATPase activity from holo-Av2 in the presence of Av1 and the rate of ATP hydrolysis was higher at the lower component ratio, supporting previous reports that Av1 is required for ATP hydrolysis by Av2. Surprisingly, we also observed ATP hydrolysis by apo-Av2, indicating that the 4Fe-4S cluster is not required for ATPase activity by Av2. The ATP hydrolysis rates of apo-Av2 were less than those of holo-Av1 (discussed further below) and also increased at the lower component ratio.

Importantly, phosphate concentrations from controls containing only the ATP regeneration system, ATP alone, and the ATP regeneration system excluding kinase ("no protein") were well below those observed from the samples with the nitrogenase component proteins, indicating that the phosphate released into solution is the result of nitrogenase activity (Figure 5.5).

Some ATPase activity is observed from assays with Av1 in the absence of Av2. This is probably due to contamination from Av2 (or other ATPases) that weren't sufficiently removed during the nitrogenase purification. Under the same concentrations of Av1, the ATPase activities in the presence of both holo-Av2 and apo-Av2 are significantly higher than the background ATPase activity observed from Av1 alone (Figure 5.2 & 5.3, compare gray with pink(holo) and blue(apo)). At a component ratio of 0.05, when Av2 is completely saturated by Av1 (10 Av1 per every 1 Av2), we observed maximal rates of ATP hydrolysis of $3.7 \pm 0.3 \mu\text{mole } P_i \text{ min}^{-1} \text{ mg Av2}^{-1}$ and $0.89 \pm 0.01 \mu\text{mole } P_i \text{ min}^{-1} \text{ mg Av2}^{-1}$ for holo- and apo-Av2 respectively; the rate of ATP hydrolysis by holo-Av2 is 4.2 times the rate of hydrolysis by apo-Av2. The rate of ATP hydrolysis in the Av1 alone sample was $0.32 \pm 0.02 \mu\text{mole } P_i \text{ min}^{-1} \text{ mg Av2}^{-1}$, well below that of the samples with Av2 (note: the rate of hydrolysis of the Av1 alone sample was also divided by the same value for the mg of Av (0.008 mg) even though there was no Av2 added to this sample).

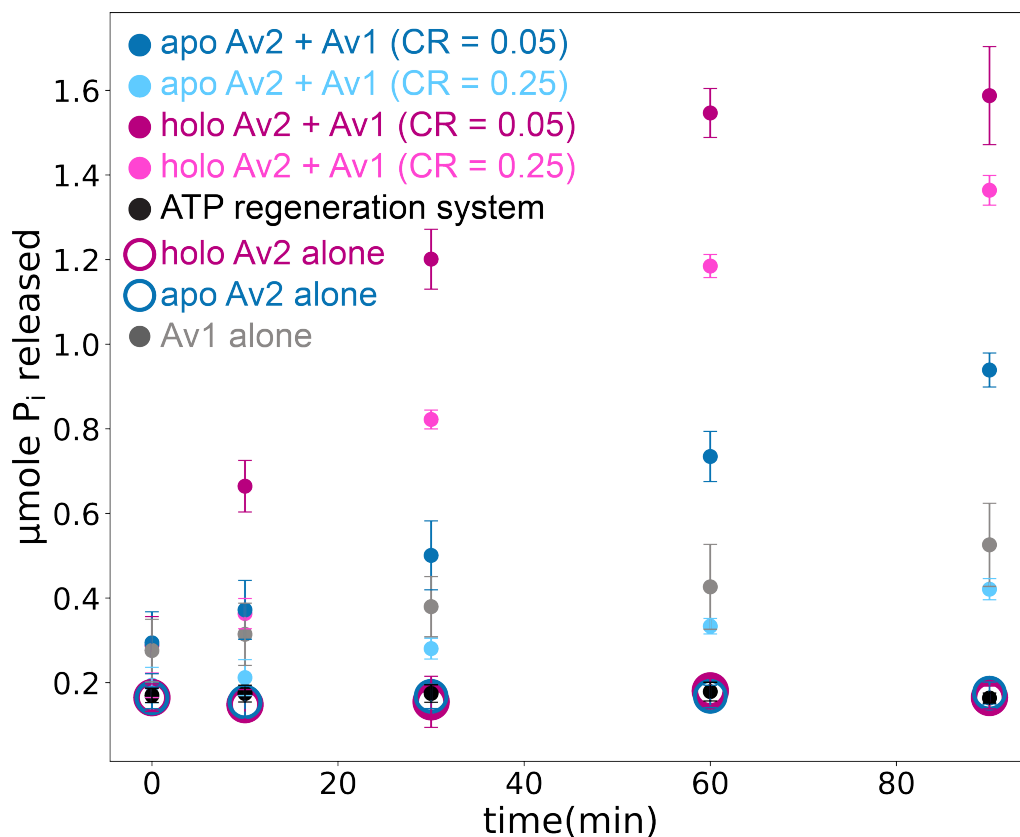


Figure 5.2: ATPase time trial of holo- and apo-Av2 with Av1 and ATP regeneration system. ATPase activity determined by measuring inorganic phosphate concentration in assay samples by ion chromatography (see *Methods*). Each point and error bars are the average and standard deviation, respectively, of three trials performed on the same day. Av1 alone sample contains the same concentration of Av1 as the CR = 0.05 samples and 5 times as much Av1 as the CR = 0.25 samples.

If we subtract the rate of ATP hydrolysis by the Av1 alone sample from those with Av2, our adjusted rates for ATP hydrolysis by holo- and apo-Av2 are $3.4 \pm 0.3 \mu\text{mole P}_i \text{ min}^{-1} \text{ mg Av2}^{-1}$ and $0.6 \pm 0.3 \mu\text{mole P}_i \text{ min}^{-1} \text{ mg Av2}^{-1}$, respectively, resulting in a corrected ratio for the rate of ATP hydrolysis by the holo-Av2 to the rate by apo-Av2 of 6.0.

No significant phosphate released was observed in the absence of Av1 (Figure 5.2, open circles), confirming previous reports that Av2 must bind to Av1 for ATP hydrolysis. It is interesting that this necessity is conserved even when Av2 does not contain the 4Fe-4S cluster, because the main purpose of Av2 binding to Av1 is understood to be to facilitate electron transfer from the 4Fe-4S cluster of Av2 to the P-cluster of Av1. ATP hydrolysis by both holo- and apo-Av2 is dependent on Av1, with the rate of inorganic phosphate release increasing with the concentration of Av1 (all assays were performed at the same concentration of Av2). The rates of ATP hydrolysis by holo- and apo- Av2 increase 1.4 and

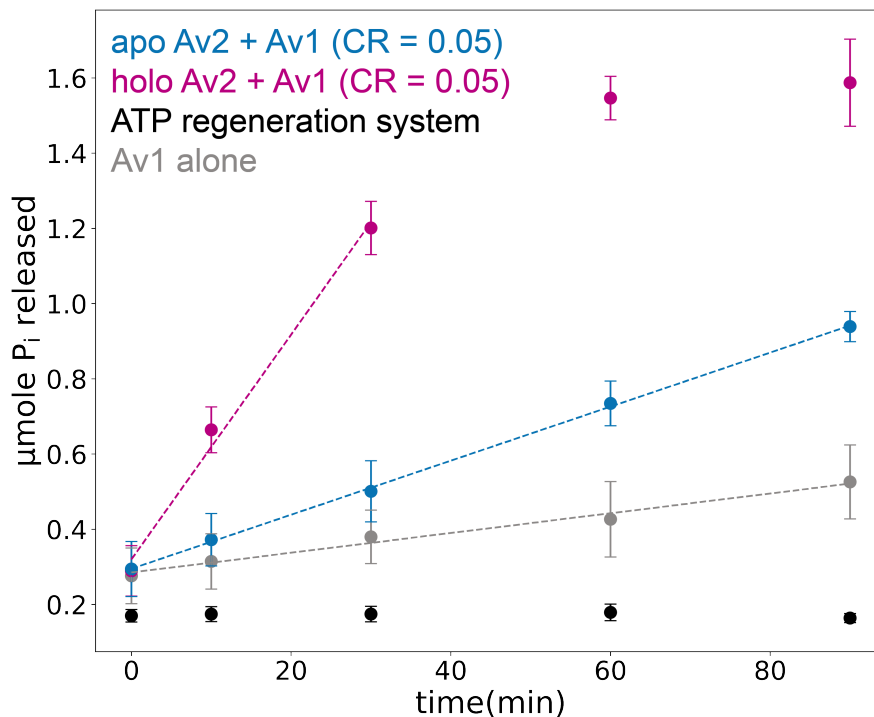


Figure 5.3: ATPase time trial of holo- and apo-Av2 with Av1 and ATP regeneration system at low component ratio (Av2 saturated by Av1, CR = 0.05). ATPase activity determined by measuring inorganic phosphate concentration in assay samples by ion chromatography (see *Methods*). Each point and error bars are the average and standard deviation, respectively, of three trials performed on the same day. Av1 alone sample contains the same concentration of Av1 as the CR = 0.05 samples. Dashed lines are linear least squares fit lines of the data (only the linear region of holo Av2 data used), the slope of which is divided by the amount of Av2 in the assays (0.008 mg) to obtain the rate of ATPase activity by Av2: $v_{holoAv2} = 3.7 \pm 0.3 \mu\text{mol P}_i \text{ min}^{-1} \text{ mg Av2}^{-1}$, $v_{apoAv2} = 0.90 \pm 0.01 \mu\text{mol P}_i \text{ min}^{-1} \text{ mg Av2}^{-1}$, $v_{Av1alone} = 0.33 \pm 0.02 \mu\text{mol P}_i \text{ min}^{-1} \text{ mg Av2}^{-1}$ (for the purpose of comparison with assays with Av2, the rate of P_i release was divided by 0.008 mg Av2 in the *Av1 alone* sample even though no Av2 was added to this assay).

2.9 fold, respectively, with the decrease in component ratio from 0.25 to 0.05. The Av1 alone sample was performed at the same concentration of Av1 as the assays performed at CR = 0.05, and thus 5 times greater Av1 concentrations than in the assays performed at CR = 0.25. Therefore, the rate of P_i release from the Av1 alone assays was divided by 5 to correct for the background ATPase activity from the Av1 samples in the CR = 0.25 assays. Before correction, the rate of ATPase activity by holo- and apo-Av2 at CR = 0.25

(2 Av1 for every 1 Av2) was $2.6 \pm 0.2 \mu\text{mole P}_i \text{ min}^{-1} \text{ mg Av2}^{-1}$ and $0.31 \pm 0.02 \mu\text{mole P}_i \text{ min}^{-1} \text{ mg Av2}^{-1}$, respectively. After correcting for 1/5 of the rate of ATP hydrolysis of Av1 alone (at 5X the Av1 concentration in these CR = 0.25 assays), the rates of ATP hydrolysis of holo- and apo- Av2 were $2.6 \pm 0.2 \mu\text{mole P}_i \text{ min}^{-1} \text{ mg Av2}^{-1}$ and $0.25 \pm 0.02 \mu\text{mole P}_i \text{ min}^{-1} \text{ mg Av2}^{-1}$, which reveals that the rate of ATP hydrolysis of holo-Av2 is 12 times that of apo-Av2 at a component ratio of 0.25.

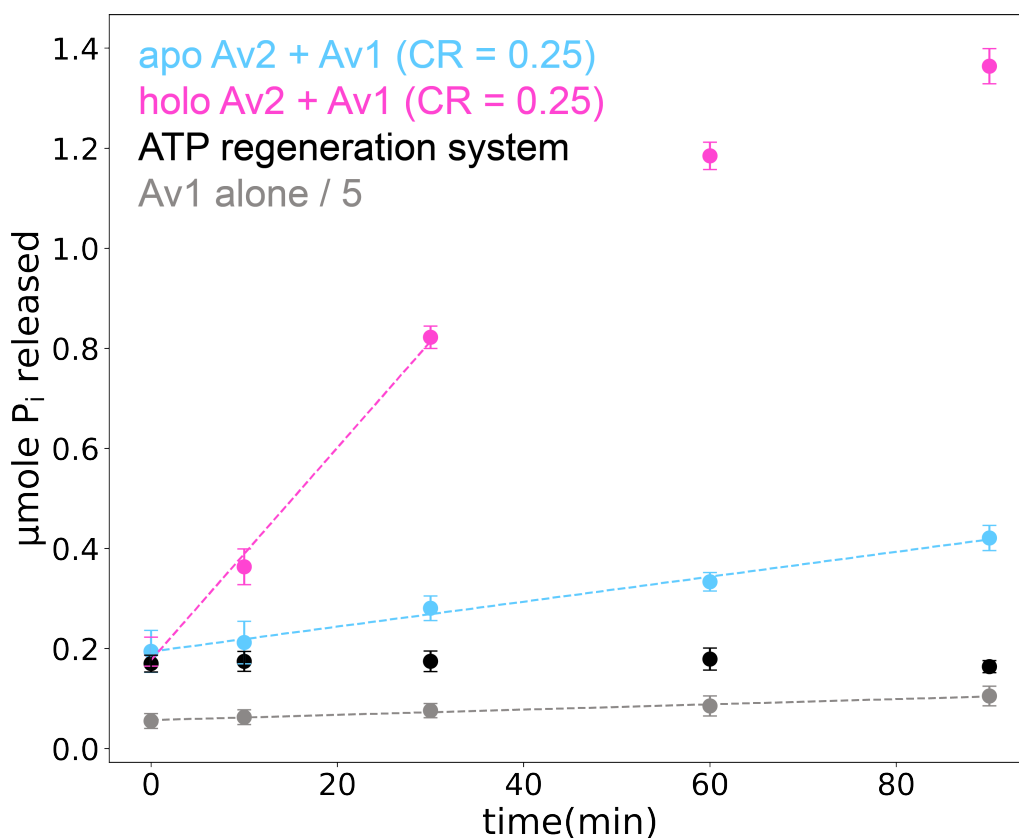


Figure 5.4: ATPase time trial of holo- and apo-Av2 with Av1 and ATP regeneration system at component ratio = 0.25. ATPase activity determined by measuring inorganic phosphate concentration in assay samples by ion chromatography (see *Methods*). Each point and error bars are the average and standard deviation, respectively, of three trials performed on the same day. Av1 alone sample contains 5 times the amount of Av1 as the CR = 0.25 samples so the values for phosphate released from these samples were divided by 5. Dashed lines are linear least squares fit lines of the data (only the linear region of holo Av2 data used), the slope of which is divided by the amount of Av2 in the assays (0.008 mg) to obtain the rate of ATPase activity by Av2: $v_{holoAv2} = 2.7 \pm 0.2 \mu\text{mol P}_i \text{ min}^{-1} \text{ mg Av2}^{-1}$, $v_{apoAv2} = 0.31 \pm 0.02 \mu\text{mol P}_i \text{ min}^{-1} \text{ mg Av2}^{-1}$, $v_{Av1alone} = 0.066 \pm 0.005 \mu\text{mol P}_i \text{ min}^{-1} \text{ mg Av2}^{-1}$ (for the purpose of comparison with assays with Av2, the rate of P_i release was divided by 0.008 mg Av2 in the *Av1 alone* sample even though no Av2 was added to this assay).

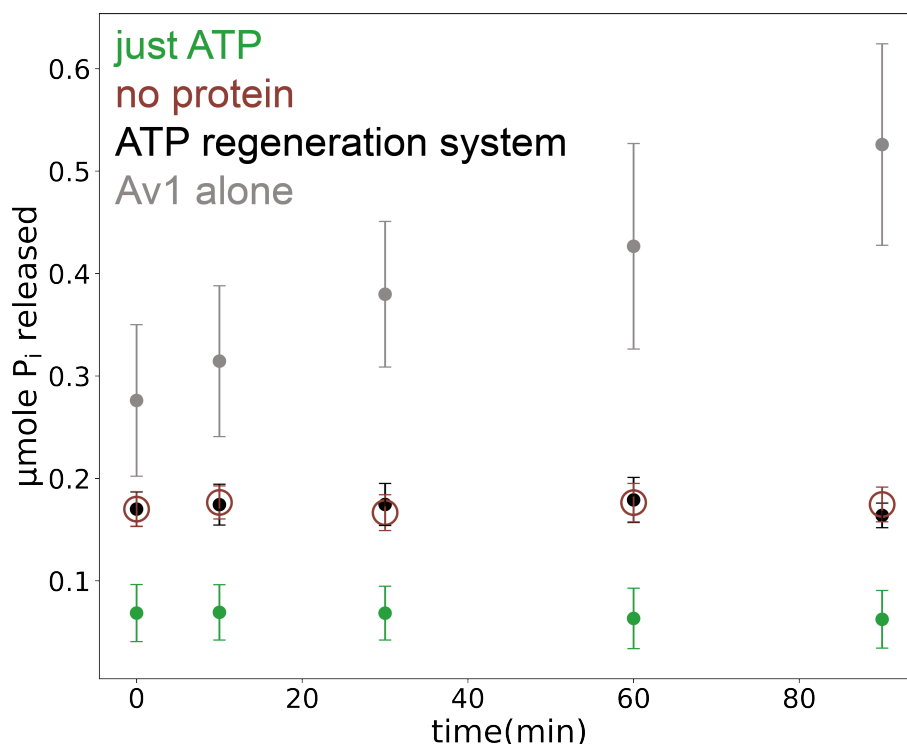


Figure 5.5: ATPase time trial of control samples from ATPase assay reported in Figures 5.2 and 5.3 (included separately for clarity). ATPase activity determined by measuring inorganic phosphate concentration in assay samples by ion chromatography (see *Methods*). Each point and error bars are the average and standard deviation, respectively, of three trials performed on the same day. Av1 alone sample contains the same concentration of Av1 as the CR = 0.05 samples and 5 times as much Av1 as the CR = 0.25 samples.

5.4 Conclusions and Future Outlook

A novel form of the nitrogenase Fe protein was discovered by X-ray crystallography and this report includes a characterization of the metal-binding and ATPase activity of this enzyme. Amino acid analysis and ICP-MS were used in parallel to precisely determine the stoichiometry of Fe binding to the holo- (as purified) and apo-Av2, revealing that slightly more than 4 Fe atoms were present for every holo-Av2 dimer and about 2 Fe atoms were present for every apo-Av2 dimer. We expect 4 Fe atoms bound to every holo-Av2 dimer and the excess iron we observe could be due to adventitious iron bound at other positions on Av2 or contaminating proteins that also coordinate iron. There are multiple possibilities for the identity of the Fe atoms in the apo-Av2 samples. The 2 Fe per Av2 dimer could indicate that half of the Av2 enzymes are in the holo- form (with a 4Fe-4S cluster bound) and half of the Av2 enzymes have no iron atoms bound. Alternatively, most of the Av2 enzymes could have a 2Fe-2S cluster bound, although this is not supported by EPR analysis or the crystal structure. Finally, the majority of the sample could lack a

4Fe-4S cluster, with iron adventitiously bound or Fe bound at a specific location distinct from the 4Fe-4S cluster binding site, which is supported by iron anomalous diffraction data showing Fe bound at the MgATP binding site after soaking apo-Av2 crystals in a 9.9 mM iron solution.

Ion chromatography was used to accurately measure the rates of phosphate release by holo- and apo-Av2 and this method offers many advantages over established ATPase assay methods. As expected, holo-Av2 is an active ATPase and the rates of ATP hydrolysis are similar to what have been observed from previous reports. At a component ratio of 0.25 we observe an ATPase rate of $2.7 \pm 0.2 \mu\text{mol P}_i \text{ min}^{-1} \text{ mg Av2}^{-1}$ for holo-Av2 while Cordewener et al. measured an ATPase rate of about $4 \mu\text{mol P}_i \text{ min}^{-1} \text{ mg Av2}^{-1}$ at the same component ratio [10]. Cordewener et al. observed a plateau in the ATPase activity of Av2 at an Av1:Av2 ratio of 2 (CR = 0.25) whereas we saw greater ATPase activity at CR = 0.05 compared to CR = 0.25, indicating that increasing the Av1:Av2 ratio above 2 further enhances ATPase activity by Av2. Danyal et al. performed pre-steady state quenched flow measurements of P_i release from nitrogenase assays and found a ATPase rate of 17 P_i released per second per MoFe protein [11]. As their assays contained 80 μM Fe protein and 20 μM MoFe protein, this corresponds to a rate of 4.25 P_i released per second per Fe protein. In our ATPase assays at CR = 0.5 (compared to their CR = 4), we measure a P_i release rate of 2.7 P_i per Fe protein per second, which is about half of the rate that they observe. However, it is important to note that their assays were performed at a higher component ratio, which we show causes a decrease in ATPase activity. Also, they measured stopped flow pre-steady state ATPase activity, which could differ significantly from ATPase on the longer timescales that we measured.

Significantly, we observed that the 4Fe-4S cluster of the nitrogenase Fe protein is not required for its role as an ATPase. ATPase activity has not been observed previously with forms of apo-Av2 that have been generated by chemical chelation and future work will include measuring the ability of chemically-chelated apo-Av2 to hydrolyze ATP. We will also investigate whether apo-Av2 formed by the novel crystallographic method reported here is capable of supporting reduction of substrates by the nitrogenase complex. Not only does this work reveal the unexpected result that the Fe protein is an active ATPase in the absence of the 4Fe-4S cluster, but also provides a new method for phosphate quantification that will be valuable for future scientists studying ATPase enzymes.

References

- (1) Rangaraj, P.; Shah, V. K.; Ludden, P. W. *PNAS USA* **1997**, *94*, 11250–11255.

- (2) Georgiadis, M. M.; Komiya, H.; Chakrabarti, P.; Woo, D.; Kornuc, J. J.; Rees, D. C. *Science* **1992**, *257*, 1653–1659.
- (3) Jasniewski, A. J.; Sickerman, N. S.; Hu, Y.; Ribbe, M. W. *Inorganics* **2018**, *6*, 1–14.
- (4) Hu, Y.; Corbett, M. C.; Fay, A. W.; Webber, J. A.; Hodgson, K. O.; Hedman, B.; Ribbe, M. W. *PNAS* **2006**, *103*, 17125–17130.
- (5) Hu, Y.; Corbett, M. C.; Fay, A. W.; Webber, J. A.; Hedman, B.; Hodgson, K. O.; Ribbe, M. W. *PNAS USA* **2005**, *102*, 13825–13830.
- (6) Yang, Z. Y.; Ledbetter, R.; Shaw, S.; Pence, N.; Tokmina-Lukaszewska, M.; Eilers, B.; Guo, Q.; Pokhrel, N.; Cash, V. L.; Dean, D. R.; Antony, E.; Bothner, B.; Peters, J. W.; Seefeldt, L. C. *Biochemistry* **2016**, *55*, 3625–3635.
- (7) Hausingers, R. P.; Howard, J. J. *Biol. Chem* **1983**, *258*, 13486–13492.
- (8) Anderson, G. L.; Howard, J. B. *Biochemistry* **1984**, *23*, 2118–2122.
- (9) Katz, F. E.; Shi, X.; Owens, C. P.; Joseph, S.; Tezcan, F. A. *Anal. Biochem.* **2017**, *520*, 62–67.
- (10) Cordewener, J.; Kruse-Wolters, M.; Wassink, H.; Haaker, H.; Veeger, C. *Eur. J. Biochem* **1988**, *172*, 739–745.
- (11) Danyal, K.; Shaw, S.; Page, T. R.; Duval, S.; Horitani, M.; Marts, A. R.; Lukoyanov, D.; Dean, D. R.; Raugei, S.; Hoffman, B. M.; Seefeldt, L. C.; Antony, E. *PNAS USA* **2016**, *113*, E5783–E5791.

Appendix A

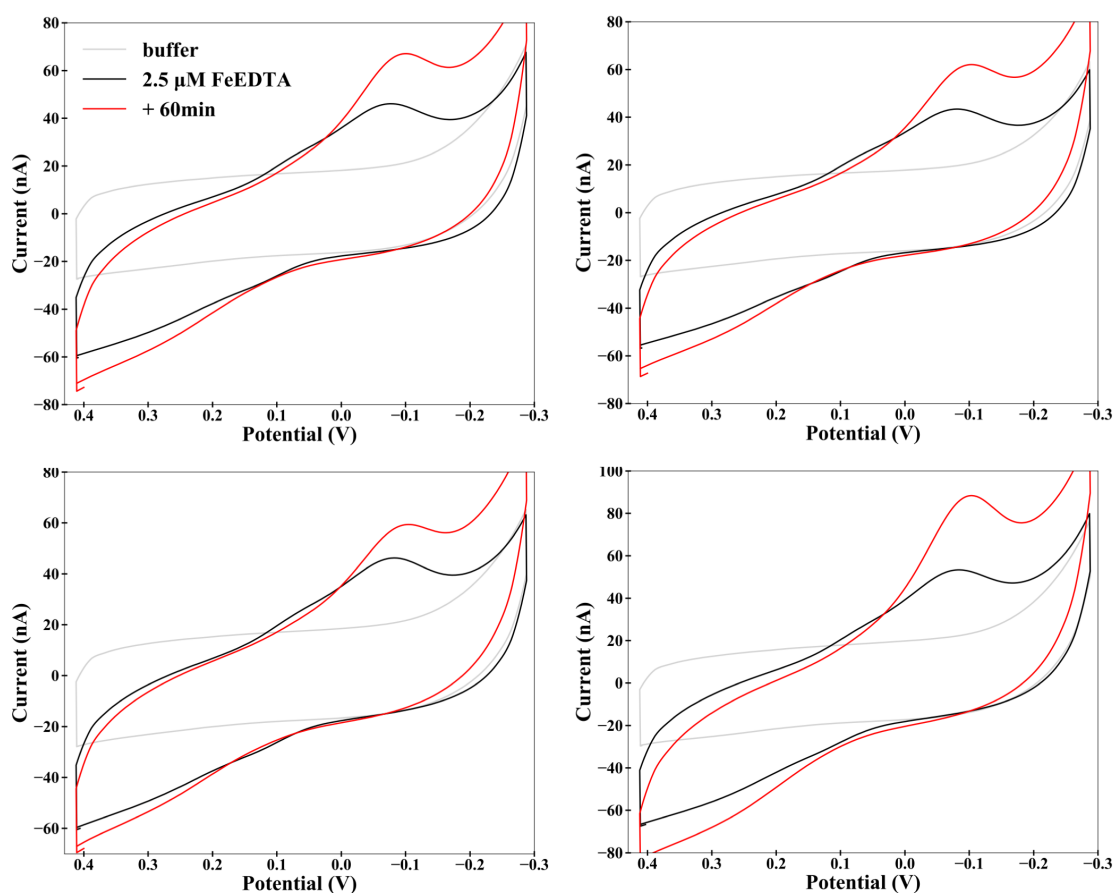
SUPPORTING INFORMATION FOR CRITICAL INVESTIGATIONS
OF THE ELECTROCHEMISTRY OF DNA2A.1 Cyclic Voltammetry of premixed solution of Fe^{2+} and EDTA on DNA-modified electrodes in HEPES Buffer

Figure A.1: Cyclic voltammetry of $2.5 \mu\text{M}$ FeEDTA on DNA-modified electrodes (black). CV was performed initially after deposition of the solution onto the electrode (black) and one hour later (red). Irreversible reductive wave at about -100 mV vs. NHE apparent initially and increases over time. Four panels show CVs from 4 representative electrodes of 16-electrode multiplexed chip. All CVs performed anaerobically in HEPES buffer (20 mM HEPES, 0.5 M NaCl, 5% glycerol, pH 7.74) at 100 mV/s with Ag/AgCl gel-tip reference electrode.

A.2 Cyclic Voltammetry of premixed solution of Fe^{2+} and EDTA on DNA-modified electrodes in Tris Buffer

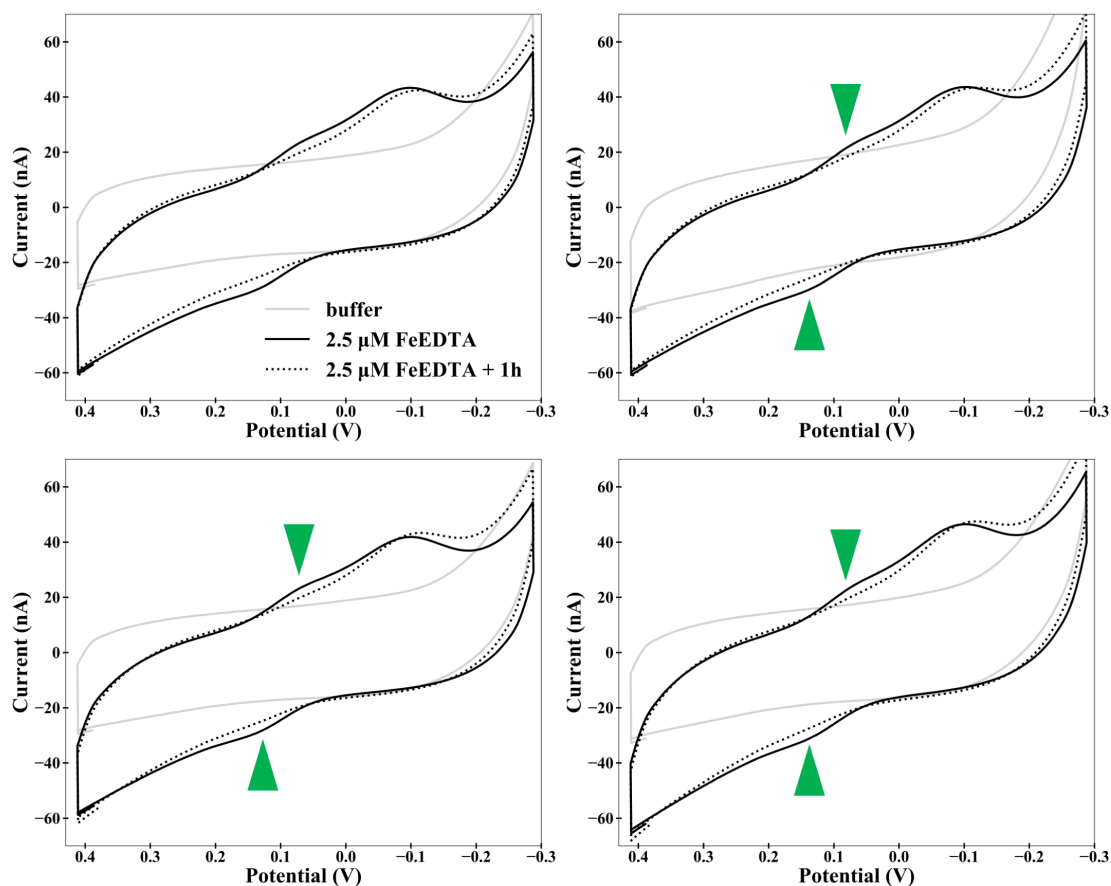


Figure A.2: Cyclic voltammetry of 2.5 μM FeEDTA on DNA-modified electrodes. CV was performed initially after deposition of the solution onto the electrode (solid black) and one hour later (dotted black). Two signals were observed: an irreversible reductive wave at about -100 mV vs. NHE and a reversible signal with midpoint potential of about 90 mV vs. NHE (green triangles). Four panels show CVs from 4 representative electrodes of 16-electrode multiplexed chip. All CVs performed anaerobically in Tris buffer (20 mM Tris, 0.5 M NaCl, 5% glycerol, pH 7.74) at 100 mV/s with Ag/AgCl gel-tip reference electrode.

Appendix B

SUPPORTING INFORMATION FOR ISOTOPE EFFECT STUDIES OF NITROGENASE

B.1 Nitrogenase Purification

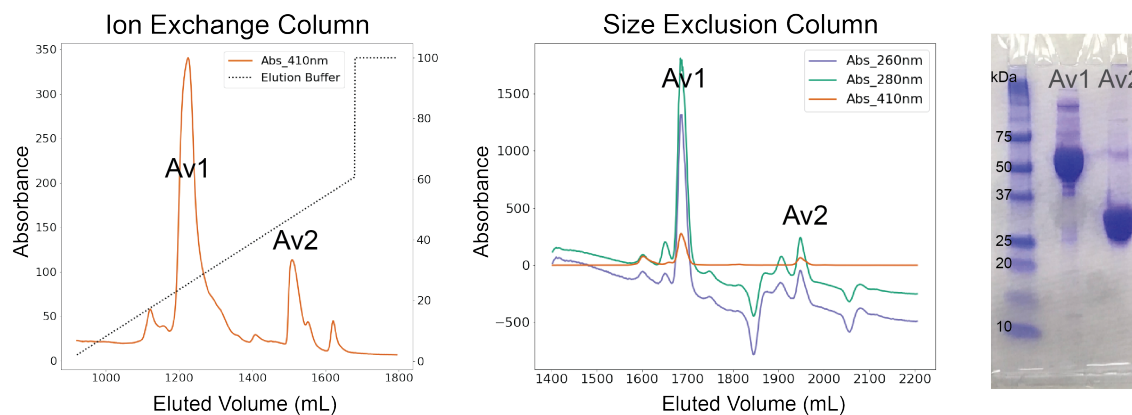


Figure B.1: Representative FPLC traces and denaturing gels from purification of nitrogenase enzyme from *Azotobacter vinelandii*. Av1 and Av2 purified using ion exchange chromatography (left) followed by size exclusion chromatography (middle). Details of purification described in *Methods*. Av1 collected from ion exchange column at 19-22.5% Elution Buffer (311.5-341.3 mM NaCl) and Av2 collected from ion exchange column at 37.5-40.8% Elution Buffer (468.8-496.8 mM NaCl). Av1 collected from size exclusion at 1671-1703 mL and Av2 collected from size exclusion column at 1940-1971 mL. To run gel (BioRad Mini-PROTEAN TGX Stain Free Gels), 15 μ L sample was combined with 5 μ L of loading dye and 11 μ L of the mixture was loaded into each well. Gel ran at 200 V for 20 minutes then rinsed with milliQ water, stained with Coomassie blue, and destained with a 40% methanol 10% acetic acid solution.

B.2 Gas Chromatographs of Headspace of Acetylene Reduction Assays

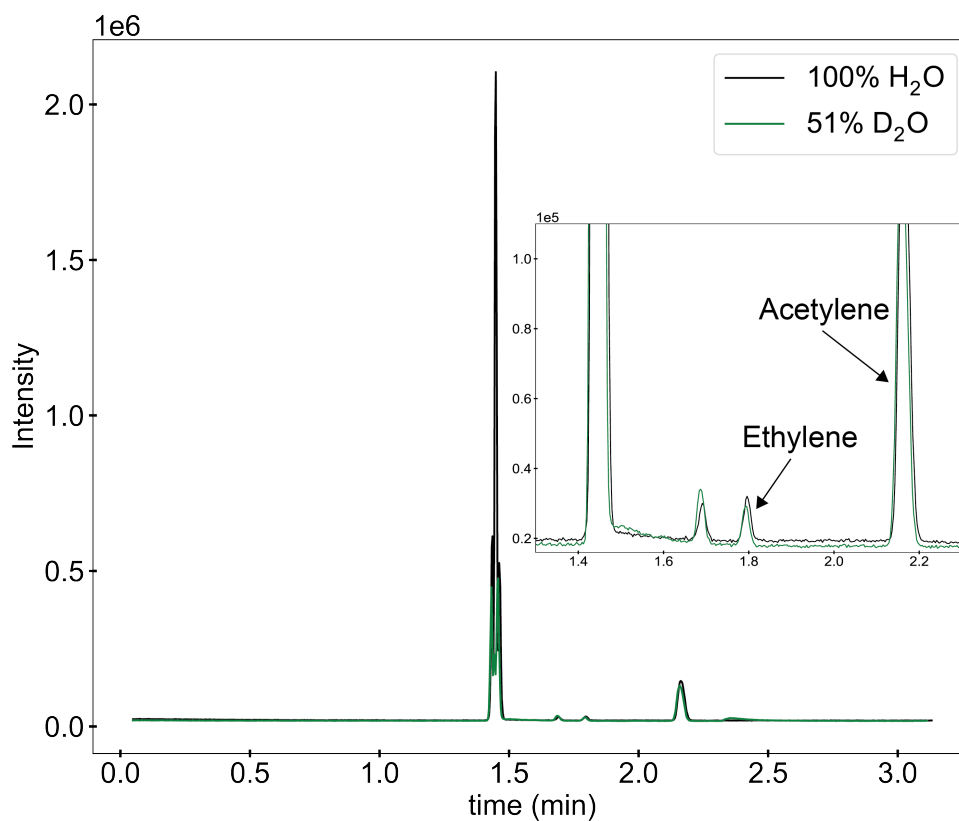


Figure B.2: Representative gas chromatogram of headspace of acetylene reduction assay of nitrogenase in 100% H_2 (black) or 51% D_2O (green). Inset is zoom of region where ethylene peak elutes (1.8 min). Assay and GC-MS quantification of ethylene isotopologues described in *Methods*. Headspace (50 μL) injected using a Hamilton gastight syringe. Column : GASPRO PLOT-Q (Restek), column temperature: 80 $^{\circ}C$ (isothermal).

B.3 Mass Spectra of Ethylene Peak of Headspace of Acetylene Reduction Assays

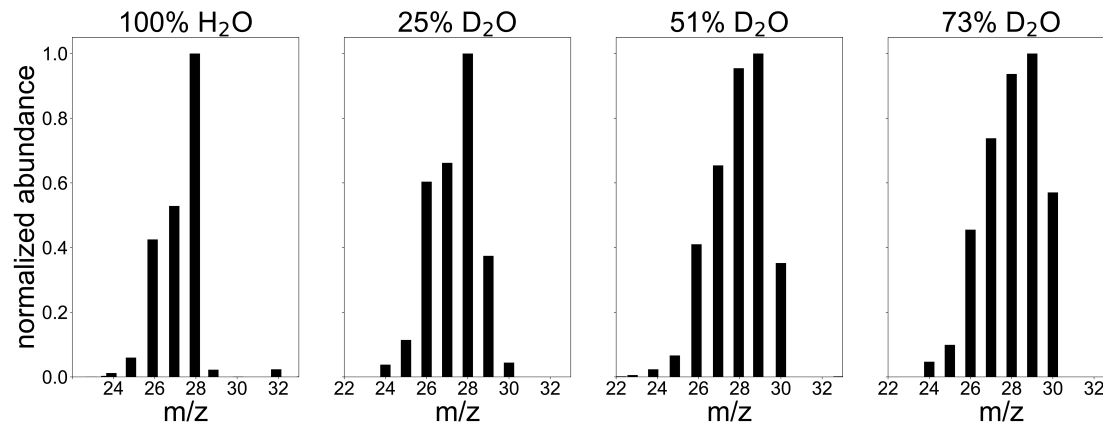


Figure B.3: Mass spectra of ethylene peaks of headspace of acetylene reduction assays in 100% H₂O, 25% D₂O, 51% D₂O, and 73% D₂O. Abundance normalized to peak of greatest abundance. Mass spectra generated by integrating under ethylene peak of extracted ion chromatograms of m/z = 23-32. As mole fraction of D₂O in buffer increases, greater abundance seen at m/z = 29 and m/z = 30, corresponding to increase in C₂H₃D and C₂H₂D₂ in the headspace.

B.4 Deconvolution of Overlapping Mass Spectra of Ethylene Isotopologues

Mass spectra of the headspace of acetylene reduction assays in deuterated solvent show abundance at $m/z = 28$ from C_2H_4 , $m/z = 29$ from C_2H_3D , and $m/z = 30$ from $C_2H_2D_2$. Quantifying the relative amounts of these species is not as straightforward as simply comparing the abundance at $m/z = 28$ vs. $m/z = 29$ vs. $m/z = 30$ because of the fragmentation that ethylene undergoes upon mass spectrometry analysis at 70 eV. The abundance in the mass spectrum at $m/z = 29$ is due to the molecular ion of C_2H_3D and also the fragmentation of $C_2H_2D_2$ in which it has lost one atomic mass unit (amu). Similarly, the abundance at $m/z = 28$ is due to the molecular ion of C_2H_4 , the fragments of C_2H_3D that have lost one amu, and the fragments of $C_2H_2D_2$ that have lost two amu. Therefore, these overlapping mass spectra need to be deconvoluted in order to quantify relative amounts of C_2H_4 , C_2H_3D , and $C_2H_2D_2$. The method used for this deconvolution is described here.

With each assay, a non-deuterated ethylene standard was used to measure the fragmentation of C_2H_4 and the other ethylene isotopologues were assumed to have the same fragmentation pattern, as has been assumed in previous reports [1]. All abundance values were obtained by integrating under the extracted ion chromatogram of each ion.

First, the abundance at each m/z value for the mass spectra of C_2H_4 was normalized to the molecular ion at $m/z = 28$ to generate the fraction of the abundance of the molecular ion at that particular m/z value. For example $F(27, C_2H_4)$ is equal to the abundance at $m/z = 27$ divided by the abundance at $m/z = 28$ of the same spectra:

$$F(28, C_2H_4) = \frac{A_{C_2H_4}(28)}{A_{C_2H_4}(28)} = 1$$

$$F(27, C_2H_4) = \frac{A_{C_2H_4}(27)}{A_{C_2H_4}(28)}$$

$$F(26, C_2H_4) = \frac{A_{C_2H_4}(26)}{A_{C_2H_4}(28)}$$

$$F(25, C_2H_4) = \frac{A_{C_2H_4}(25)}{A_{C_2H_4}(28)}$$

where $A_{C_2H_4}(m/z)$ is the observed abundance at that m/z value from the ethylene standard analyzed using the same method as the assay samples. For the deuterated ethylene isotopologues, $F(27, C_2H_4)$ is the probability that a molecule of ethylene will fragment with the loss of one H/D relative to the molecular ion. $F(26, C_2H_4)$ is the probability that the ethylene molecule will fragment by the loss of two H/Ds and $F(25, C_2H_4)$ is the probability that ethylene will fragment by losing 3 H/Ds.

Next, the abundance values from the mass spectra of the headspace samples of the acetylene reduction assays were deconvoluted by calculating the contribution at each m/z from each isotopologue (written as $C(m/z, C_2H_2L_2)$). To do this, each isotopologue was considered independently. For the dideuterated isotopologue, the molecular ion is $m/z = 30$ and the only contribution to the abundance at $m/z = 30$ is the dideuterated ethylene. The fragments of $C_2H_2D_2$ in which one H atom is lost will contribute to the abundance at $m/z = 29$. Because $C_2H_2D_2$ has 2 H atoms and 2 D atoms, the probability that it will lose one H atom (when it fragments by the loss of one H or D) is $1/2$. Therefore, the contribution from $C_2H_2D_2$ at $m/z = 29$ ($C(29, C_2H_2D_2)$) is $1/2$ multiplied by the probability of losing one H/D ($F(27, C_2H_4)$), thus $C(29, C_2H_2D_2) = A(30) \times \frac{1}{2}F(27, C_2H_4)$. This analysis was repeated for each m/z from the molecular ion ($m/z = 30$) to $m/z = 25$. Then this analysis was repeated for the singly-deuterated ethylene.

Contribution from $C_2H_2D_2$:

$$C(30, C_2H_2D_2) = A(30)$$

$$C(29, C_2H_2D_2) = A(30) \times \frac{1}{2}F(27, C_2H_4)$$

$$C(28, C_2H_2D_2) = A(30) \times \frac{1}{2}F(27, C_2H_4) + A(30) \times \frac{1}{6}F(26, C_2H_4)$$

$$C(27, C_2H_2D_2) = A(30) \times \frac{4}{6}F(26, C_2H_4)$$

$$C(26, C_2H_2D_2) = A(30) \times \frac{1}{6}F(26, C_2H_4) + A(30) \times \frac{1}{2}F(25, C_2H_4)$$

$$C(25, C_2H_2D_2) = A(30) \times \frac{1}{2}F(25, C_2H_4)$$

Contribution from C_2H_3D :

$$C(29, C_2H_3D) = A(29) - C(29, C_2H_2D_2)$$

$$C(28, C_2H_3D) = C(29, C_2H_3D) \times \frac{3}{4}F(27, C_2H_4)$$

$$C(27, C_2H_3D) = C(29, C_2H_3D) \times \frac{1}{4}F(27, C_2H_4) + C(29, C_2H_3D) \times \frac{1}{2}F(26, C_2H_4)$$

$$C(26, C_2H_3D) = C(29, C_2H_3D) \times \frac{1}{2}F(26, C_2H_4) + C(29, C_2H_3D) \times \frac{1}{4}F(25, C_2H_4)$$

$$C(25, C_2H_3D) = C(29, C_2H_3D) \times \frac{3}{4}F(25, C_2H_4)$$

Contribution from C_2H_4 :

$$C(28, C_2H_4) = A(28) - C(28, C_2H_2D_2) - C(28, C_2H_3D)$$

$$C(27, C_2H_4) = A(27) - C(27, C_2H_2D_2) - C(27, C_2H_3D)$$

$$C(26, C_2H_4) = A(26) - C(26, C_2H_2D_2) - C(26, C_2H_3D)$$

$$C(25, C_2H_4) = A(25) - C(25, C_2H_2D_2) - C(25, C_2H_3D)$$

The relative amounts of C_2H_4 , C_2H_3D , and $C_2H_2D_2$ were determined by comparing the molecular ion peak of the spectra of each isotopologue after subtracting the contribution from the fragments of the other isotopologues [$C(28, C_2H_4)$, $C(29, C_2H_3D)$, and $C(30, C_2H_2D_2)$, respectively]. The results are summarized in Table B.1.

Table B.1: Relative Amounts of Ethylene Isotopologue Products of Acetylene Reduction Assays Quantified by GC-MS

Deuterium Enrichment	C_2H_4	C_2H_3D	$C_2H_2D_2$
25%	$65 \pm 1\%$	$30.6 \pm 0.9\%$	$3.9 \pm 0.2\%$
51%	$28 \pm 2\%$	$52 \pm 2\%$	$20 \pm 1\%$
73%	$13 \pm 3\%$	$49 \pm 2\%$	$37 \pm 2\%$

B.5 FTIR Standard Curves of Deuterated Ethylenes

The FTIR spectra of the headspace of acetylene reduction assays contained sharp stretches in the 840 -1000 cm^{-1} region, corresponding to the wagging mode of the H-C-H or H-C-D moieties [2]. The peak heights of these stretches were used to quantify the relative amounts of ethylene isotopologue products from acetylene reduction assays. It is well reported that the molar absorptivity of the C_2H_4 stretch (949 cm^{-1}) and the $\text{C}_2\text{H}_2\text{D}_2$ stretch (843 cm^{-1}) are equivalent. However, there is some discrepancy as to whether the $\text{C}_2\text{H}_3\text{D}$ stretch (943 cm^{-1}) has a molar absorptivity that is half of that of C_2H_4 and $\text{C}_2\text{H}_2\text{D}_2$ or equivalent to these species. In quantifying the products of nitrogenase reduction of C_2D_2 , Han and Newton [3] report that the molar absorptivity of the $\text{C}_2\text{H}_3\text{D}$ peak is half of that of the C_2H_4 peak so they doubled the $\text{C}_2\text{H}_3\text{D}$ peak height for their analysis. In similar measurements, Benton et al. [4] and Fisher et al. [5] report that the molar absorptivity of the *trans*- $\text{C}_2\text{H}_2\text{D}_2$ peak is half of that of the C_2H_4 and *cis*- $\text{C}_2\text{H}_2\text{D}_2$ peaks, but they don't explicitly address the molar absorptivity of the peak from the singly deuterated species, $\text{C}_2\text{H}_3\text{D}$, at 943 cm^{-1} . Due to this uncertainty in the literature, we performed a standard curve with C_2H_4 and $\text{C}_2\text{H}_3\text{D}$ to determine their molar absorptivities: $\text{C}_2\text{H}_3\text{D}$ was quantitatively transferred to a 1 L Schlenk flask to a final pressure of 1 atm and a separate flask was purged with C_2H_4 for 10 minutes and vented to 1 atm. FTIR spectra were obtained using the same procedure that was used when analyzing the headspace of nitrogenase acetylene reduction assays except known quantities (50 – 100 μL) of 1 atm $\text{C}_2\text{H}_4/\text{C}_2\text{H}_3\text{D}$ were transferred to the sample chamber that had been degassed and backfilled with Argon. Then, FTIR spectra were obtained (128 scans, 1 cm^{-1} resolution). The peak heights of the C_2H_4 (949 cm^{-1}) and $\text{C}_2\text{H}_3\text{D}$ (943 cm^{-1}) stretches were plotted against the moles of these species in the sample chamber to obtain a standard curve. The absorbance from these stretches was calculated from the percent transmittance and this was plotted against the known amount of moles of the ethylene isotopologue in the FTIR gas cell (Figure B.4). Trendlines were generated in Excel and the slope was the molar absorptivity of the species. In agreement with the report by Han and Newton, the molar absorptivity of $\text{C}_2\text{H}_3\text{D}$ (0.0238 $\mu\text{M}^{-1} \text{cm}^{-1}$) was about half of that of C_2H_4 (0.0510 $\mu\text{M}^{-1} \text{cm}^{-1}$). We also simulated the molecular spectra of C_2H_4 , $\text{C}_2\text{H}_3\text{D}$, and $\text{C}_2\text{H}_2\text{D}_2$ using TheoReTS [6] and obtained similar values for the molar absorptivities relative to each other: 46.7 cm^{-1} for $\text{C}_2\text{H}_2\text{D}_2$, 24.3 cm^{-1} for $\text{C}_2\text{H}_3\text{D}$, and 41.7 cm^{-1} for C_2H_4 . To our knowledge, this is the only reported standard curve of C_2H_4 and $\text{C}_2\text{H}_3\text{D}$ by FTIR and is necessary for quantifying ethylene isotopologues by FTIR.

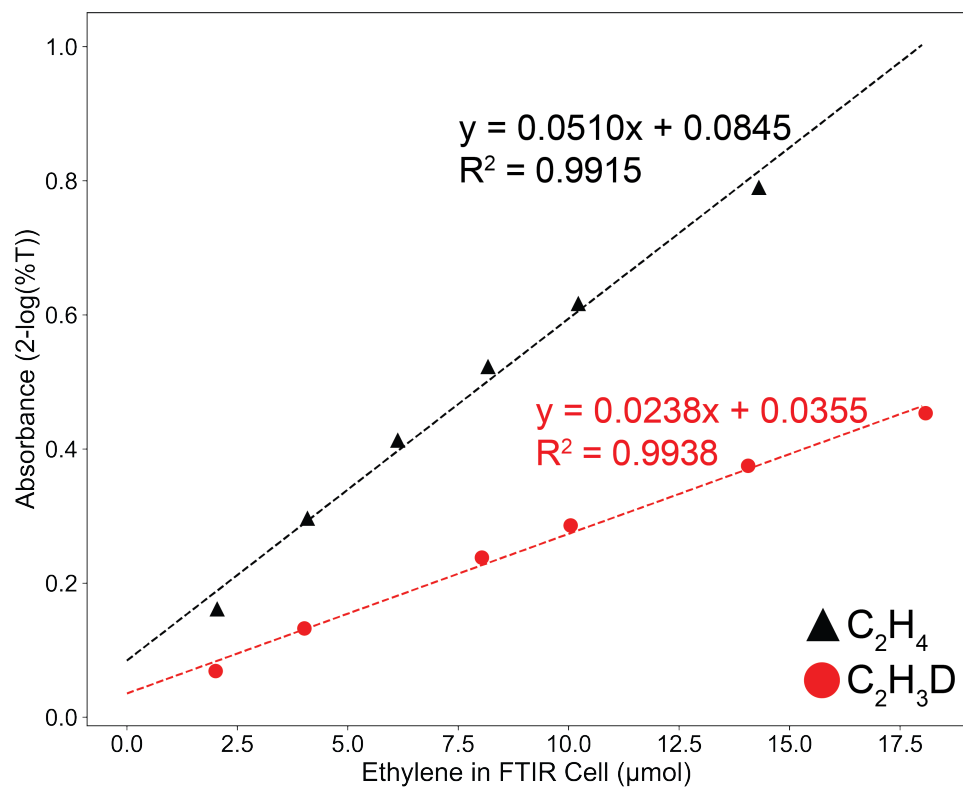


Figure B.4: FTIR standard curves of ethylene isotopologues C_2H_4 and $\text{C}_2\text{H}_3\text{D}$. Peak transmittance values of the C_2H_4 stretch at 949 cm^{-1} (black) and the $\text{C}_2\text{H}_3\text{D}$ stretch at 943 cm^{-1} (red) were converted to absorbance ($\text{Abs} = 2 - \log(\% \text{ Transmittance})$) and plotted against the amount of ethylene present in the FTIR gas cell (μmol). Linear least squares fit trendlines were fit to the data in Excel and the slope of the line was the molar absorptivity of the species.

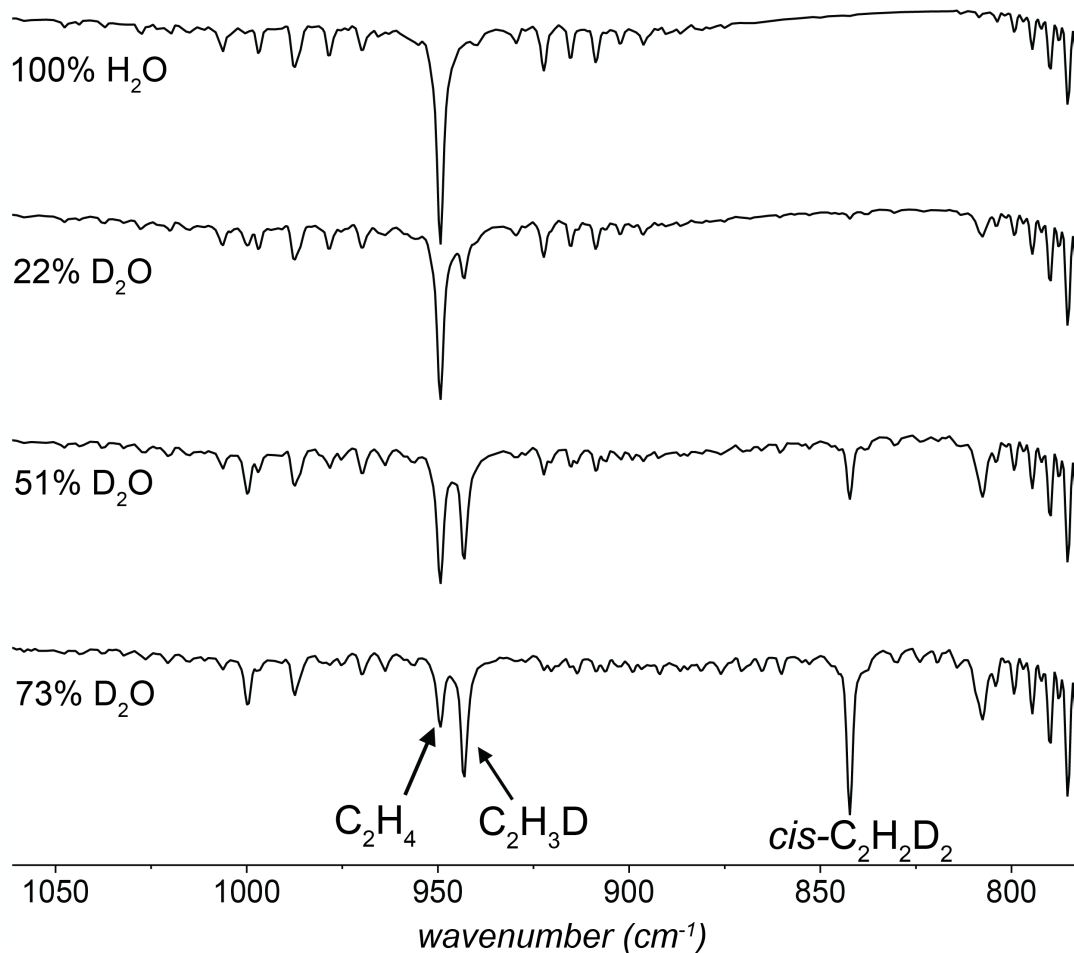
B.6 FTIR Spectra of Headspace of Acetylene Reduction Assays

Figure B.5: FTIR spectra of the headspace of acetylene reduction assays performed in varying mole fraction of deuterium in the solvent. In 100% H_2O , the only observed stretch is at 949 cm^{-1} due to the presence of C_2H_4 . Rotational stretches are observed on either side of the main C_2H_4 peak. In 22% D_2O , a peak emerges at 943 cm^{-1} due to $\text{C}_2\text{H}_3\text{D}$ in the headspace. At 51% D_2O , the $\text{C}_2\text{H}_3\text{D}$ peak at 943 cm^{-1} increases and a peak emerges at 843 cm^{-1} due to the presence of $\text{cis-C}_2\text{H}_2\text{D}_2$.

Table B.2: Relative Amounts of Ethylene Isotopologue Products of Acetylene Reduction Assays Quantified by FTIR

Deuterium Enrichment	C ₂ H ₄	C ₂ H ₃ D	C ₂ H ₂ D ₂
22%*	54.9%	41.7%	3.4%
51%	31 ± 1%	54 ± 1%	14 ± 2%
73%	16 ± 1%	53.0 ± 0.9%	30.9 ± 0.7%

* only one trial performed

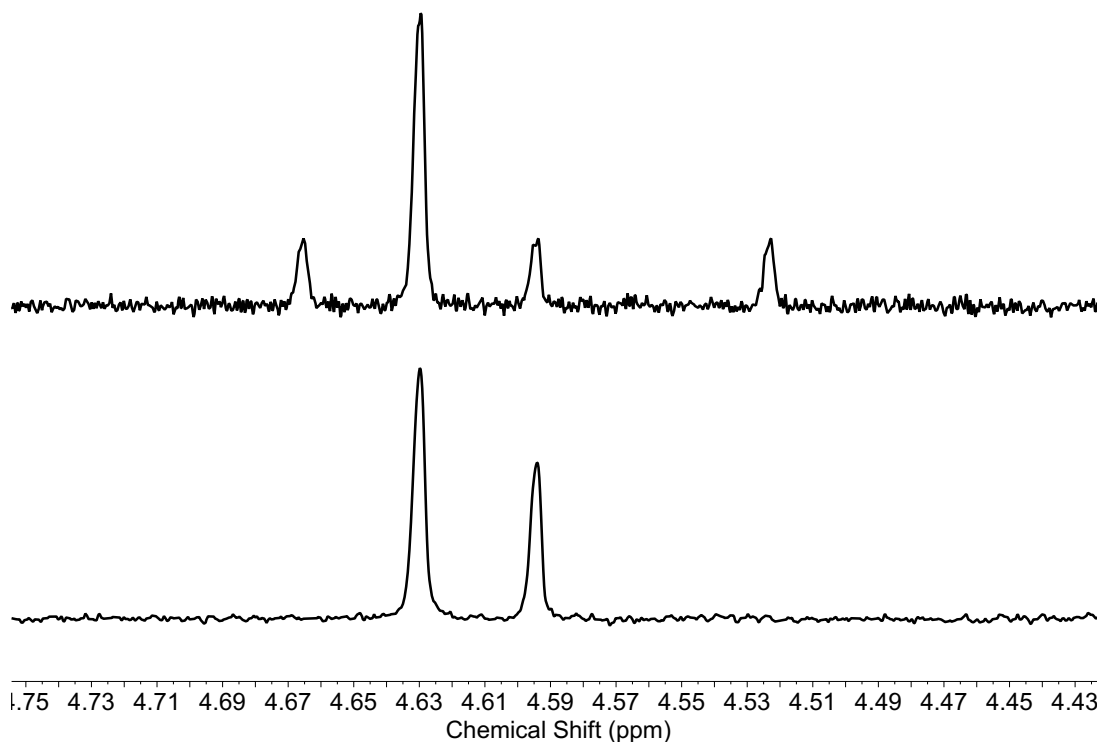
B.7 ^1H NMR Spectra of Headspace of Proton Reduction Assays

Figure B.6: H_2/HD region of ^1H NMR spectra from headspace of proton reduction assay. Without deuterium decoupling (top), HD signal is a 1:1:1 triplet. Deuterium decoupling (bottom) condenses triplet into single peak. NMR tube filled with 1 mL CDCl_3 and capped with PTFE septa. Headspace from proton reduction assay (3 mL) transferred to a NMR tube with bubbling through CDCl_3 . NMR performed on a Varian 600 MHz Spectrometer with 5 mm triple resonance inverse probe (parameters: 512 scans, 16 sec relaxation delay, pulse angle 90°C). ^1H NMR (CDCl_3 , 600 MHz) H_2 : δ ppm 4.63 (s, 2H); HD: δ ppm 4.59 (t, $J=48$ Hz, 1H)

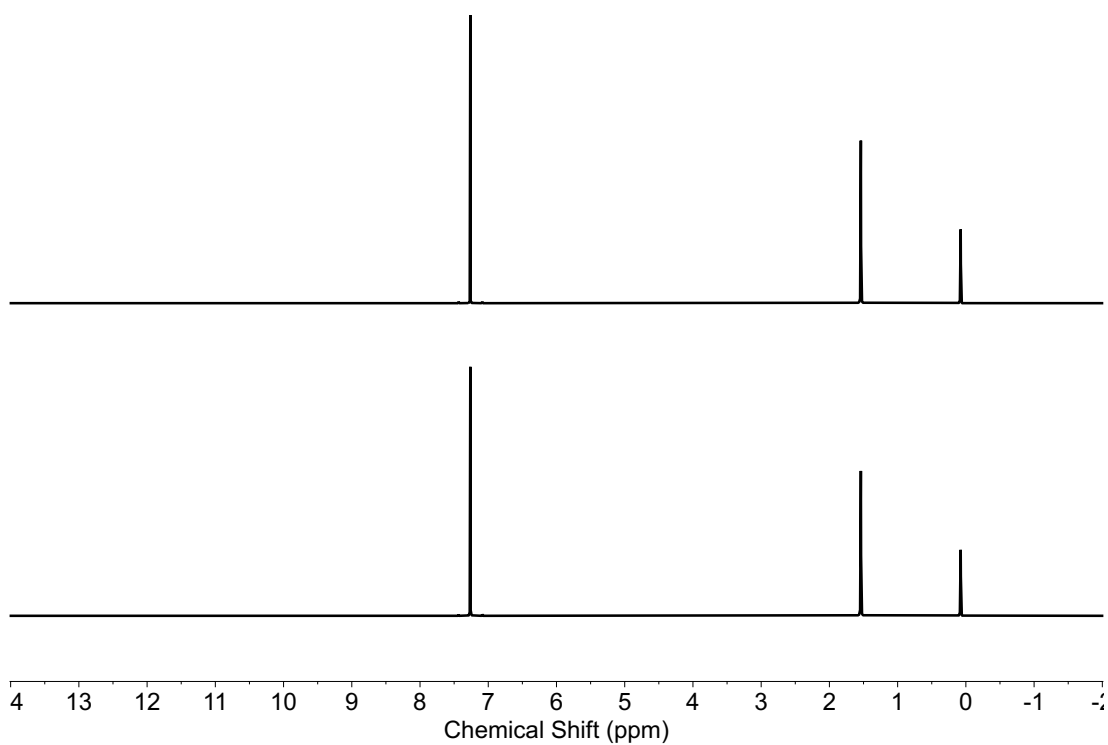


Figure B.7: Full ^1H NMR spectra from headspace of proton reduction assay. Close up of H_2 and HD region shown in Figure B.6 above. NMR tube filled with 1 mL CDCl_3 and capped with PTFE septa. Headspace from proton reduction assay (3 mL) transferred to a NMR tube with bubbling through CDCl_3 . NMR performed on a Varian 600 MHz Spectrometer with 5 mm triple resonance inverse probe (parameters: 512 scans, 16 sec relaxation delay, pulse angle 90°C).

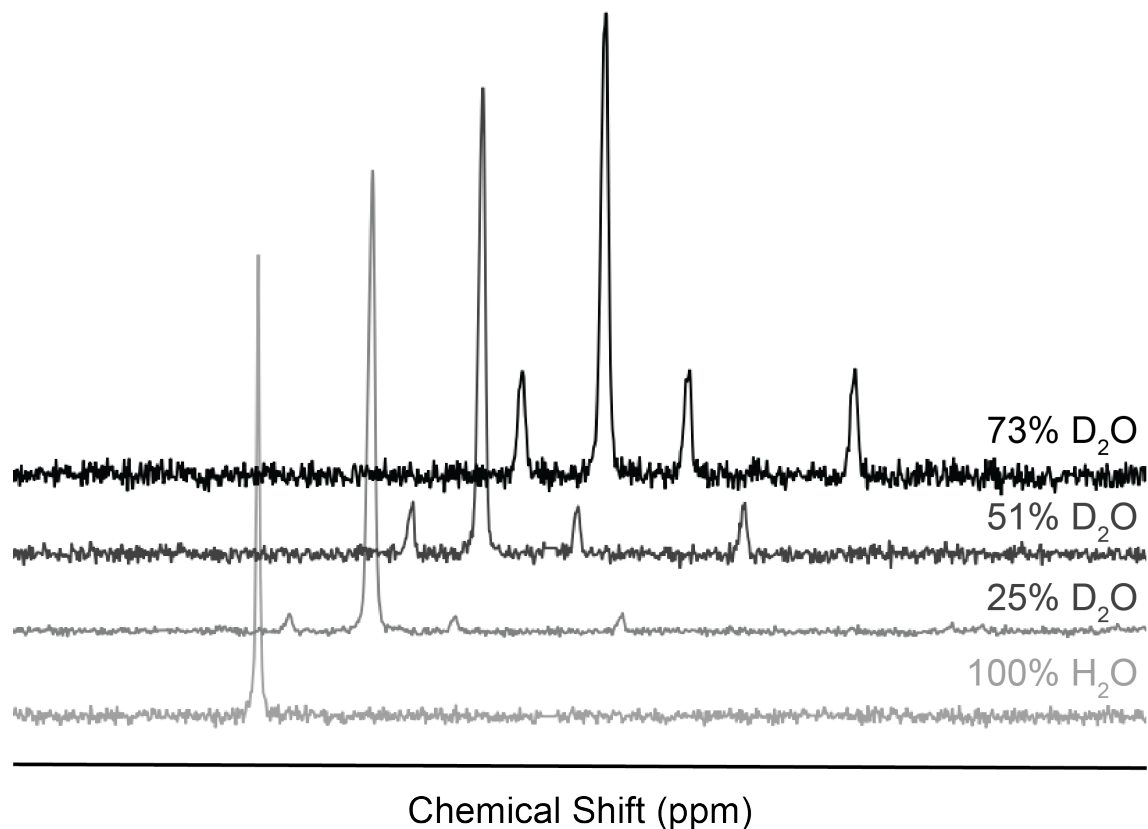


Figure B.8: H_2/HD region of ^1H NMR spectra from headspace of proton reduction assays in 100% H_2O , 25% D_2O , 51% D_2O , and 73% D_2O (bottom to top, grey to black) without deuterium decoupling. In original spectra peaks overlap and in this figure spectra are offset for clarity (see Figure B.6 for chemical shift of peaks). Peak intensity normalized to intensity of H_2 peak. H_2 is a singlet and HD signal is a 1:1:1 triplet. NMR tube filled with 1 mL CDCl_3 and capped with PTFE septa. Headspace from proton reduction assay (3 mL) transferred to a NMR tube with bubbling through CDCl_3 . NMR performed on a Varian 600 MHz Spectrometer with 5 mm triple resonance inverse probe (parameters: 512 scans, 16 sec relaxation delay, pulse angle 90°). ^1H NMR (CDCl_3 , 600 MHz) H_2 : δ ppm 4.63 (s, 2H); HD: δ ppm 4.59 (t, $J=48$ Hz, 1H)

B.8 Attempt to quantify H₂, HD, and D₂ by GC-MS

We first attempted to quantify the products of proton reduction assays (H₂, HD, and D₂) in H₂O/D₂O with GC-MS by quantifying the abundance of ions of $m/z = 2, 3,$ and $4,$ respectively. Modifications to the GC-MS system were made to optimize quantification of the hydrogen isotopologues including the installation of 5 Å molecular sieve column for sufficient separation of H₂ from background argon. The main challenge to our experimental set up was the interference from the carrier gas He, which has the same molecular weight as D₂. To address this, an external power supply was installed to allow for us to manually decrease the ionization energy to 21.5 eV (instead of 70 eV), which is below that of the carrier gas, He (24.5 eV), but above that of H₂ (15.4 eV). To improve the sensitivity, instead of scanning for all ions, we tuned the quadropole to only allow ions of $m/z = 2, 3,$ and 4 to reach the detector. Despite these optimizations, GC-MS was not suitable for our system because of the considerable mass bias among D₂, HD, and H₂. The system was an order of magnitude more sensitive to D₂ than H₂, which meant that the error in the standard curve of D₂ was a significant portion of the H₂ signal (Figure B.10). Regardless of this error, proton reduction assays were performed in 51% D₂O and the hydrogen isotopologues in the headspace were subject to analysis with our GC-MS system with the parameters described above. The results agreed with the quantification by ¹H NMR reported below; however, the precision was not satisfactory.

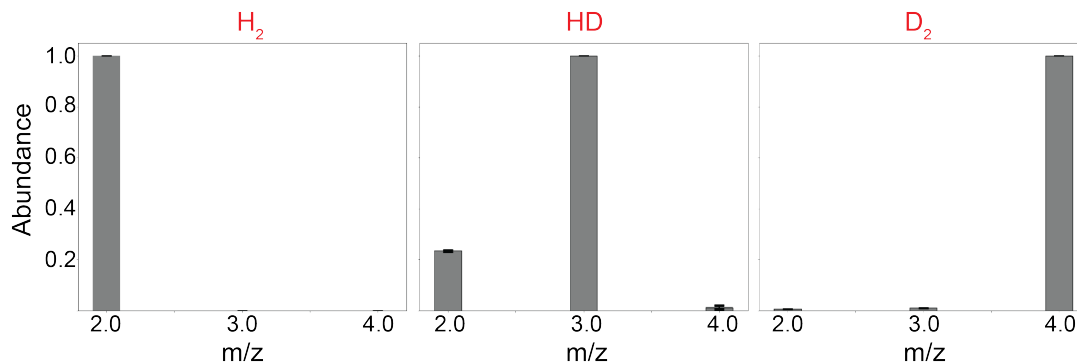


Figure B.9: Mass Spectra of H₂ (left), HD (middle), and D₂ (right) standards. Peak areas were obtained from the extracted ion chromatographs of $m/z = 2, 3, 4$ for H₂, HD, and D₂, respectively. In the mass spectra of HD, considerable abundance was observed at $m/z = 2$, which could be due to H₂ contamination or fragmentation of HD. In the mass spectra of D₂, abundance was observed at $m/z = 2$ and $m/z = 3$, which was insignificant in relation to the abundance at $m/z = 4$; however because of the mass bias among hydrogen isotopologues, correcting for this in the abundance at $m/z = 2$ in assay trials was a significant alteration. The normalized abundances shown in this figure were used to calculate the contribution from each hydrogen isotopologue to the abundance in the mass spectra (see Equations B.1 - B.6).

The following analysis was performed to quantify the relative amounts of H₂, HD, and D₂ from the peak areas of the extracted ion chromatographs of $m/z = 2, 3$, and 4 , respectively.

First the normalized abundance was calculated for H₂, HD, and D₂ standards by the following equations:

$$F(2, D_2) = \frac{A_{D_2}(2)}{A_{D_2}(4)}$$

$$F(3, D_2) = \frac{A_{D_2}(3)}{A_{D_2}(4)}$$

$$F(4, D_2) = \frac{A_{D_2}(4)}{A_{D_2}(4)} = 1$$

$$F(2, HD) = \frac{A_{HD}(2)}{A_{HD}(3)}$$

$$F(3, HD) = \frac{A_{HD}(3)}{A_{HD}(3)} = 1$$

where $A_{L_2}(m/z)$ is the abundance at m/z observed from the L_2 standard used to make the standard curve.

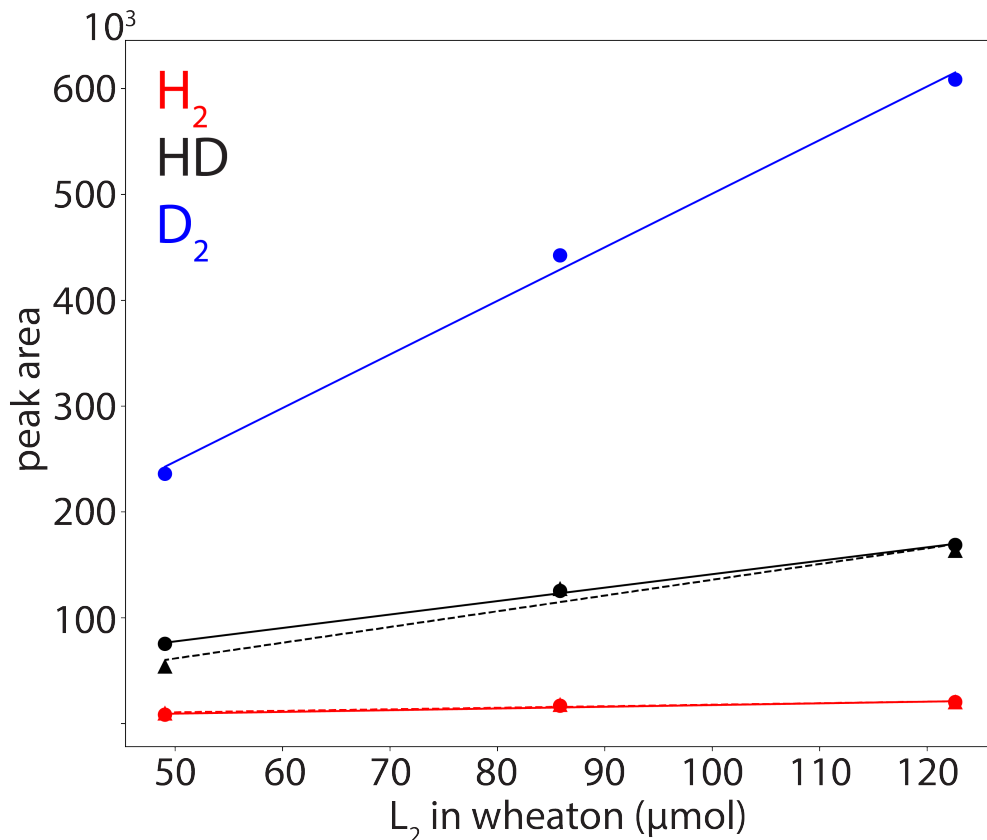


Figure B.10: Standard Curve of H₂ (red), HD (black), and D₂ (blue) quantified by GC-MS. Peak areas were obtained from the extracted ion chromatographs of $m/z = 2, 3, 4$ for H₂, HD, and D₂, respectively. Slope and intercept parameters for linear least squares fit lines to standard curves: $m_{H_2,trial1} = 161.7$, $b_{H_2,trial1} = 1309$, $m_{H_2,trial2} = 144.1$, $b_{H_2,trial2} = 3452$; $m_{HD,trial1} = 1270$, $b_{HD,trial1} = 14142$, $m_{HD,trial2} = 1486$, $b_{HD,trial2} = 12776$; $m_{D_2} = 5063$, $b_{D_2} = 5630$. Only one trial of D₂ standard curve was usable.

The contribution at a particular m/z value for a particular isotopologue (L_2) is written as $C(m/z, L_2)$ and is given by the following equations:

$$C(2, D_2) = A(4) \times F(2, D_2) \quad (B.1)$$

$$C(3, D_2) = A(4) \times F(3, D_2) \quad (B.2)$$

$$C(4, D_2) = A(4) \quad (B.3)$$

$$C(2, HD) = [A(3) - C(3, D_2)] \times F(2, HD) \quad (B.4)$$

$$C(3, HD) = A(3) - C(3, D_2) \quad (B.5)$$

$$C(4, HD) = 0$$

$$C(2, H_2) = A(2) - C(2, HD) - C(2, D_2) \quad (\text{B.6})$$

where $A(m/z)$ is the observed total abundance at that m/z value and $F(m/z, L_2)$ is the normalized abundance at that m/z value from the mass spectra of the L_2 standard used to prepare the standard curve.

The error was propagated using the following equations:

$$\frac{\sigma_{F(2,D_2)}}{F(2, D_2)} = \sqrt{\left(\frac{\sigma_{A_{D_2(2)}}}{A_{D_2(2)}}\right)^2 + \left(\frac{\sigma_{A_{D_2(4)}}}{A_{D_2(4)}}\right)^2}$$

$$\sigma_{F(2,D_2)} = F(2, D_2) \times \sqrt{\left(\frac{\sigma_{A_{D_2(2)}}}{A_{D_2(2)}}\right)^2 + \left(\frac{\sigma_{A_{D_2(4)}}}{A_{D_2(4)}}\right)^2}$$

$$\frac{\sigma_{F(3,D_2)}}{F(3, D_2)} = \sqrt{\left(\frac{\sigma_{A_{D_2(3)}}}{A_{D_2(3)}}\right)^2 + \left(\frac{\sigma_{A_{D_2(4)}}}{A_{D_2(4)}}\right)^2}$$

$$\sigma_{F(3,D_2)} = F(3, D_2) \times \sqrt{\left(\frac{\sigma_{A_{D_2(3)}}}{A_{D_2(3)}}\right)^2 + \left(\frac{\sigma_{A_{D_2(4)}}}{A_{D_2(4)}}\right)^2}$$

$$\frac{\sigma_{F(2,HD)}}{F(2, HD)} = \sqrt{\left(\frac{\sigma_{A_{HD(2)}}}{A_{HD(2)}}\right)^2 + \left(\frac{\sigma_{A_{HD(3)}}}{A_{HD(3)}}\right)^2}$$

$$\sigma_{F(2,HD)} = F(2, HD) \times \sqrt{\left(\frac{\sigma_{A_{HD(2)}}}{A_{HD(2)}}\right)^2 + \left(\frac{\sigma_{A_{HD(3)}}}{A_{HD(3)}}\right)^2}$$

$$\frac{\sigma_{C(2,D_2)}}{C(2, D_2)} = \sqrt{\left(\frac{\sigma_{A(4)}}{A(4)}\right)^2 + \left(\frac{\sigma_{F(2,D_2)}}{F(2, D_2)}\right)^2}$$

$$\sigma_{C(2,D_2)} = C(2, D_2) \times \sqrt{\left(\frac{\sigma_{A(4)}}{A(4)}\right)^2 + \left(\frac{\sigma_{F(2,D_2)}}{F(2, D_2)}\right)^2}$$

$$\frac{\sigma_{C(3,D_2)}}{C(3, D_2)} = \sqrt{\left(\frac{\sigma_{A(4)}}{A(4)}\right)^2 + \left(\frac{\sigma_{F(3,D_2)}}{F(3, D_2)}\right)^2}$$

$$\sigma_{C(3,D_2)} = C(3, D_2) \times \sqrt{\left(\frac{\sigma_{A(4)}}{A(4)}\right)^2 + \left(\frac{\sigma_{F(3,D_2)}}{F(3, D_2)}\right)^2}$$

$$\sigma_{C(3,D_2)} = \sigma_{A(4)}$$

$$\frac{\sigma_{C(2,HD)}}{C(2,HD)} = \sqrt{\left(\frac{\sigma_{A(3)}^2 + \sigma_{C(3,D_2)}^2}{(A(3) - C(3, D_2))^2}\right)^2 + \left(\frac{\sigma_{F(2,HD)}}{F(2,HD)}\right)^2}$$

$$\sigma_{C(2,HD)} = C(2,HD) \times \sqrt{\left(\frac{\sigma_{A(3)}^2 + \sigma_{C(3,D_2)}^2}{(A(3) - C(3, D_2))^2}\right)^2 + \left(\frac{\sigma_{F(2,HD)}}{F(2,HD)}\right)^2}$$

$$\sigma_{C(3,HD)} = \sqrt{\sigma_{A(3)}^2 + \sigma_{C(3,D_2)}^2}$$

$$\sigma_{C(2,H_2)} = \sqrt{\sigma_{A(2)}^2 + \sigma_{C(2,HD)}^2 + \sigma_{C(2,D_2)}^2}$$

The following equations were used to calculate the moles of L_2 produced from the abundance contributions in the mass spec. The slope (m_{L_2}) was generated from a regression line of the standard curve (2 trials).

$$N_{H_2} = \frac{C(2, H_2)}{m_{H_2}}$$

$$\sigma_{N_{H_2}} = N_{H_2} \times \sqrt{\left(\frac{\sigma_{C(2,H_2)}}{C(2, H_2)}\right)^2 + \left(\frac{\sigma_{m_{H_2}}}{m_{H_2}}\right)^2}$$

$$N_{HD} = \frac{C(3, HD)}{m_{HD}}$$

$$\sigma_{N_{HD}} = N_{HD} \times \sqrt{\left(\frac{\sigma_{C(3,HD)}}{C(3, HD)}\right)^2 + \left(\frac{\sigma_{m_{HD}}}{m_{HD}}\right)^2}$$

$$N_{D_2} = \frac{C(4, D_2)}{m_{D_2}}$$

$$\sigma_{N_{D_2}} = N_{D_2} \times \sqrt{\left(\frac{\sigma_{C(4,D_2)}}{C(4, D_2)}\right)^2 + \left(\frac{\sigma_{m_{D_2}}}{m_{D_2}}\right)^2}$$

Proton reduction assays with nitrogenase were performed either under 100% Argon or with replacement of 1 mL of the headspace with 1 mL of N_2 . Three separate samples (50 μ L) of the headspace were injected into the GC-MS for analysis. The peak areas of the extracted ion chromatograms of $m/z = 2, 3,$ and 4 were analyzed using the formulas

Table B.3: GC-MS Quantification of Hydrogen Isotopologues Produced in Proton Reduction Assays of Nitrogenase

Sample	Injection	H ₂ (μmol)	HD (μmol)	D ₂ (μmol)	H ₂ (rel)	HD (rel)	D ₂ (rel)
Expt 2	1	12.1 ± 3	13.1 ± 5	1.20 ± 0.2	6.1	6.6	1
	2	25.8 ± 5	12.5 ± 5	1.70 ± 0.1	15.2	7.4	1
	3	24.2 ± 5	12.1 ± 5	1.72 ± 0.1	14.0	7.0	1
Expt 3	1	27.8 ± 6	17.4 ± 7	2.5 ± 0.2	11.0	6.9	1
	2	37.4 ± 7	16.4 ± 7	2.2 ± 0.2	17.0	7.5	1
	3	36.3 ± 7	15.8 ± 7	2.1 ± 0.2	17.2	7.5	1
Expt 4	1	8.0 ± 2	5.7 ± 2	0.97 ± 0.1	8.2	5.9	1
	2	12.5 ± 3	6.4 ± 3	1.14 ± 0.1	10.9	5.6	1
	3	11.6 ± 2	6.5 ± 3	0.94 ± 0.1	12.3	6.9	1
Expt 5	1	8.4 ± 2	5.3 ± 2	0.62 ± 0.05	13.6	8.5	1
	2	11.7 ± 2	6.2 ± 3	0.85 ± 0.07	13.7	7.2	1
	3	11.3 ± 2	6.0 ± 3	0.77 ± 0.06	14.7	7.9	1

* Experiments 2 & 3 were performed under 100% Argon and Experiments 4 & 5 were performed with replacement of 1 mL of the headspace with N₂.

described above and the results are summarized in Table B.3. Experiments 2 and 3 were performed under Argon and Experiments 4 and 5 were performed after replacement of 1 mL of the Argon headspace with 1 mL of N₂. Upon inspection, it appears that the H₂ quantities in the first injection of each of the experiments are significantly lower than that of the other 2 injections of the same vial, so these values are possibly outliers. The error in the quantities of H₂, HD, and D₂ (propogated using the equations described above) were significant; however, the mean values obtained are consistent with the values determined by ¹H NMR (see main text, Figure 4.4 and Table B.4). As expected, less L₂ was produced in assays with 1 mL of N₂ in the headspace; however the precision in the data was not good enough to observe a difference in the relative amount of products between assays under 100% Argon and assays with 1 mL of N₂ in the headspace.

Note: We also attempted to replace the He carrier gas with Argon; however, this produced chromatograms that were not usable. Additionally, we tried to separate H₂, HD, and D₂ by GC by cooling the column to liquid nitrogen temperature; however we were not able to

reach a low enough temperature to separate the species.

B.9 Derivation of Isotope Effect Model Curves

The reduction of acetylene to ethylene and protons to H₂ involves the incorporation of 2 H/D atoms into the product. With each H/D addition, there is a probability, p , that a hydrogen atom is added and a probability, q , that a deuterium atom is added. The probability that a hydrogen is added is a function of the rate of this transfer and the mole fraction of hydrogen in the solution [7]:

$$p = \frac{k_H f_H}{k_H f_H + k_D f_D}$$

where k_H and k_D are the rates of hydrogen and deuterium addition, respectively, and f_H and f_D are the mole fractions of hydrogen and deuterium in the solvent, respectively. The isotope effect (IE) is defined as $\frac{k_H}{k_D}$ and the expression for p can be rewritten as:

$$p = \frac{IE f_H}{IE f_H + f_D}$$

where f_H and f_D are the fraction of hydrogen and deuterium in the solvent, respectively. It follows that the probability of adding a deuterium (instead of a hydrogen) can be written as:

$$q = 1 - p = \frac{f_D}{IE f_H + f_D}$$

To generate H₂ and C₂H₄, two hydrogens are added. For HD and C₂H₃D, one hydrogen and one deuterium are added; and for D₂ and C₂H₂D₂, two deuteriums are added. Making the assumption that p and q are the same for the first and second proton addition, the mole fraction of dihydrogen and ethylene isotopologue products can be written as the product of the appropriate probabilities of adding H vs. D:

$$X_{C_2H_4} = X_{H_2} = p^2 = \frac{IE^2 f_H^2}{(IE f_H + f_D)^2} \quad (B.7)$$

$$X_{C_2H_3D} = X_{HD} = 2pq = \frac{2IE f_D f_H}{(IE f_H + f_D)^2} \quad (B.8)$$

$$X_{C_2H_2D_2} = X_{D_2} = q^2 = \frac{f_D^2}{(IE f_H + f_D)^2} \quad (B.9)$$

For the results of the proton reduction assays, only the ratio of H₂ to HD could be obtained so the isotope effect was calculated by the following equation:

$$\frac{X_{H_2}}{X_{HD}} = \frac{IE^2 f_H^2}{(IE f_H + f_D)^2} \cdot \frac{(IE f_H + f_D)^2}{2IE f_D f_H} = \frac{IE f_H}{2f_D} \quad (B.10)$$

In order to explicitly calculate the isotope effect from the relative amounts of isotopologue products, equations 1-4 were solved for the isotope effect[8]:

$$IE_{C_2H_4} = \frac{f_D \sqrt{X_{C_2H_4}}}{f_H - f_H \sqrt{X_{C_2H_4}}} \quad (\text{B.11})$$

$$IE_{C_2H_3D} = \frac{\sqrt{-f_D^2 f_H^2 (2X_{C_2H_3D} - 1) - X_{C_2H_3D} f_D f_H + f_D f_H}}{f_H^2 X_{C_2H_3D}} \quad (\text{B.12})$$

$$IE_{C_2H_2D_2} = \frac{f_D \left(\frac{1}{\sqrt{X_{C_2H_2D_2}}} - 1 \right)}{f_H} \quad (\text{B.13})$$

$$IE_{H_2/HD} = \frac{2f_D}{f_H} \cdot \frac{X_{H_2}}{X_{HD}} \quad (\text{B.14})$$

B.10 Least Square Fit of Acetylene and Proton Reduction Assay Results

A least squares fit was performed on the acetylene reduction data across all levels of deuterium enrichment for each ethylene isotopologue (Figure B.11). The relative amount of each ethylene isotopologue (percentage of total ethylene produced) was plotted against the mole fraction of deuterium in the solvent. Then, the `scipy.optimize.curve_fit` function was used in Jupyter notebooks to perform a non-linear least squares fit of the data to Equations 4.1-4.3. The isotope effects obtained from these fits are 1.28 ± 0.04 , 1.4 ± 0.1 , and 1.59 ± 0.05 for C_2H_4 , C_2H_3D , and $C_2H_2D_2$, respectively. Least squares fit of Equation 4.6 to mole fraction of total deuterium added during acetylene reduction assays resulted in an isotope effect of 1.40 ± 0.05 (Figure B.12).

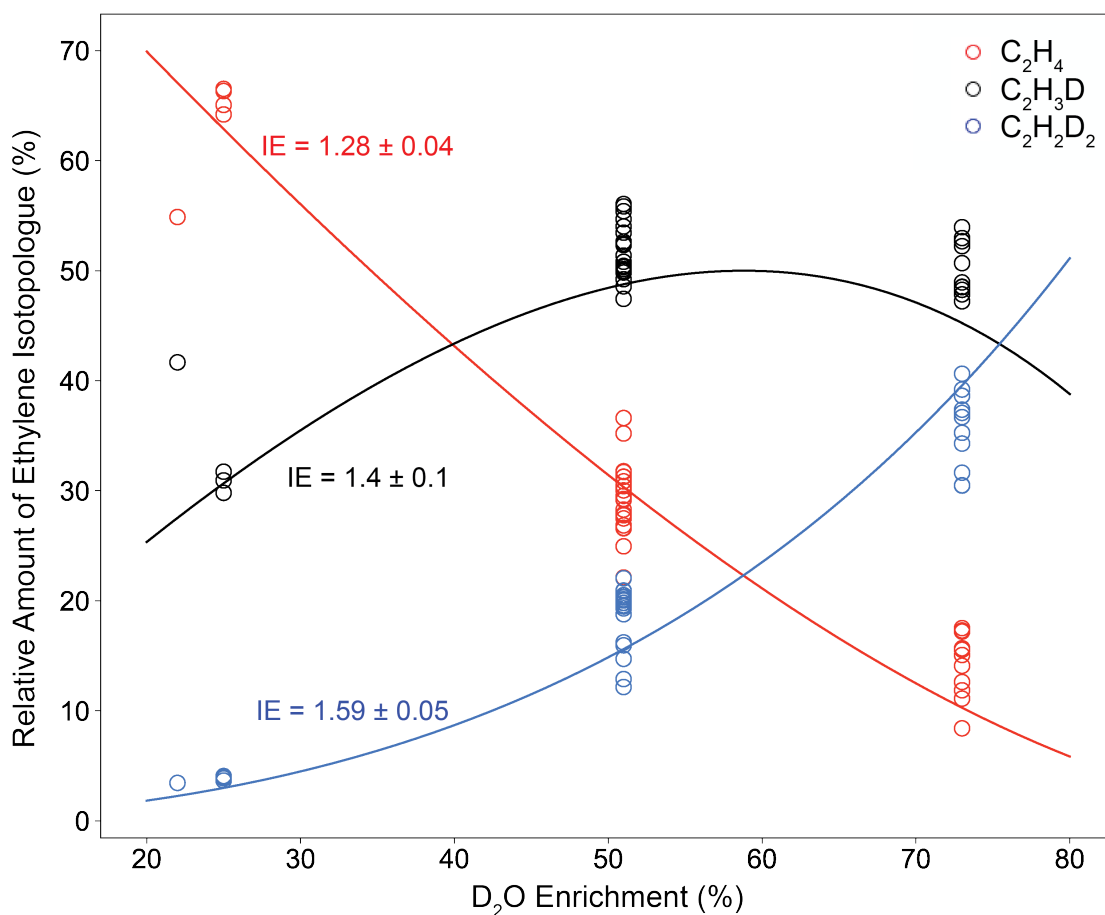


Figure B.11: Least squares fits (solid lines) of Equations 4.1-4.3 to experimental acetylene reduction assay results (points) to calculate isotope effect of acetylene reduction. Relative amounts of C_2H_4 (red), C_2H_3D (black), and $C_2H_2D_2$ (blue) plotted against the percentage of deuterium enrichment in the buffer. Plots and least squares fit (`scipy.optimize.curve_fit`) generated in Jupyter Notebooks. Isotope effects obtained from least squares fits were 1.28 ± 0.04 , 1.4 ± 0.1 , and 1.59 ± 0.04 for C_2H_4 , C_2H_2D , and $C_2H_2D_2$, respectively.

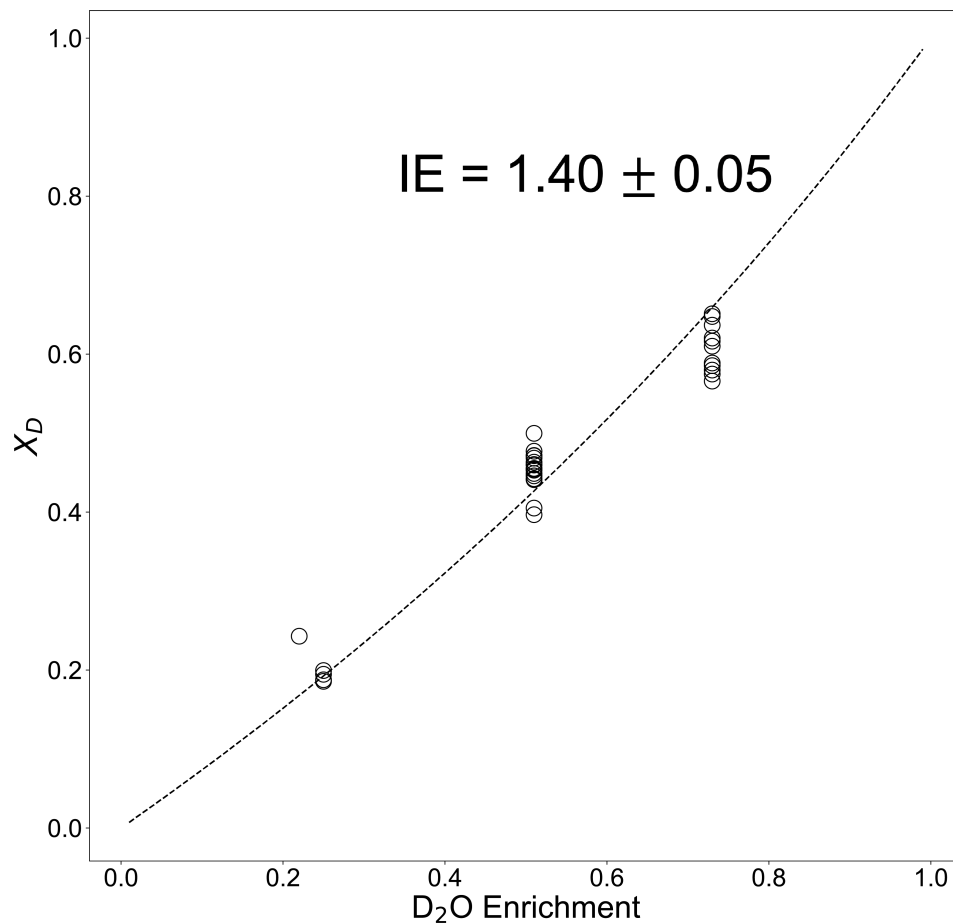


Figure B.12: Least squares fit (solid lines) of Equation 4.6 to mole fraction of deuterium added during acetylene reduction assays (open circles). Mole fraction D added calculated from observed mole fractions of C_2H_3D , and $C_2H_2D_2$ by Equation 4.4 and plotted against the percentage of deuterium enrichment in the buffer. Plots and least squares fit (`scipy.optimize.curve_fit`) generated in Jupyter Notebooks. Isotope effect obtained from least squares fit was 1.40 ± 0.05

The results of the proton reduction assay were fit to Equation 4.7 (Figure B.13) using the same method as described above (Figure B.13). The isotope effect value obtained from this fit was 4.2 ± 0.1 .

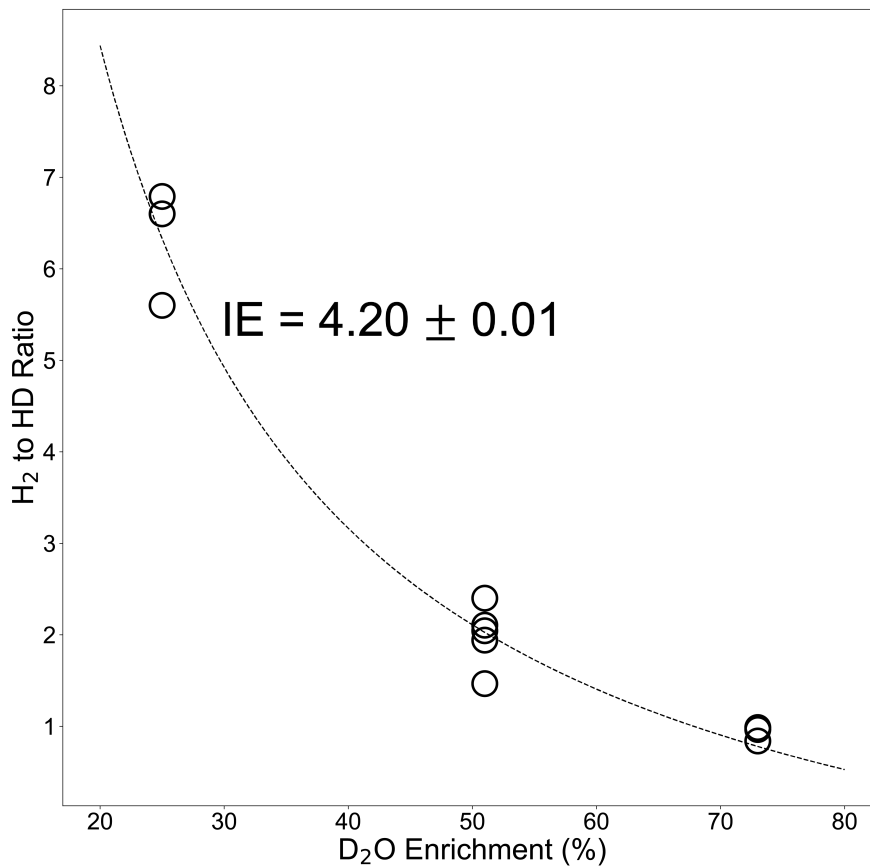


Figure B.13: Least squares fit of experimental proton reduction assay results to Equation 4.7. Ratio of H₂ to HD plotted against the percentage of deuterium enrichment in the buffer. Experimental data are black circles and least squares fit is dotted black line. Plots and least squares fit (`scipy.optimize.curve_fit`) generated in Jupyter Notebooks. Isotope effect obtained from least squares fit was 4.20 ± 0.01 .

B.11 Estimation of Fractionation Factor of H₂ Production by Nitrogenase

The level of incorporation of heavy isotopes into enzyme products are also of interest in the field of geochemistry and these results are termed *fractionation factors* instead of isotope effects. The fractionation of a heavy isotope such as deuterium is related to the ratio of the amount of deuterium in the product (in parts per million) to the natural abundance of deuterium in a standard water sample. Mechanistic conclusions are rarely made from these fractionation factors and instead, they provide clues as to the microbial sources of important chemicals such as NH₃ and CH₄ in the environment [9–13]. Upon inspection of the definitions of isotope effect and fractionation factor, in the case of solvent isotope effect experiments where protons are sourced from the solvent as in reduction by nitrogenase, the fractionation factor is the reciprocal of the isotope effect. In this work, we calculate isotope effects of nitrogenase reduction assays; however, the results can also easily be expressed as fractionation factors and are relevant to studies of geological nitrogen fixation. In reports measuring deuterium fractionation during dihydrogen production by cyanobacteria [14] or purified hydrogenases [10] significant depletion of deuterium was also observed. When we convert our isotope effect values to fractionation factors (Table B.4) our results are comparable to these studies on hydrogenases, which could indicate that deuterium depletion is a common feature of H₂ production. In fact, these levels of deuterium fractionation are similar to that of H₂ production by the electrolysis of water [14]. Additionally, the large isotope effect we see for nitrogenase H₂ production is consistent with a large isotope effect reported for methane production by nitrogenase [9]. The fractionation factor (α) is defined as the ratio of deuterium to hydrogen in the products divided by the ratio of deuterium to hydrogen in the solvent:

$$\alpha_{H_2\text{evolution}} = \frac{R_{H_2}}{R_{H_2O}} \quad (\text{B.15})$$

where R_{H_2} is the ratio of D to H in the L_2 products and R_{H_2O} is the ratio of D to H in the solvent (L is the nomenclature for either H or D). In order to calculate the D to H ratio of the L_2 , we need to know the relative amount of D_2 produced, which we weren't able to quantify by ¹H NMR. However, we can calculate an estimate of the relative amounts of H₂, HD and D₂ using the isotope effect that we calculated from Equation 4.7, by inserting the calculated isotope effect into Equations 4.1-4.3. These calculations were performed with our proton reduction data and the results are shown in Table B.4. The fractionation factor was estimated to be 0.24 ± 0.03 , 0.25 ± 0.05 , and 0.20 ± 0.02 from assays performed in 25% D₂O, 51% D₂O, and 73% D₂O, respectively. All of the values are within error of each other.

Table B.4: Calculating Fractionation Factor of Proton Reduction

sample	H2/HD	IE	calc_X _{D₂}	calc_X _{HD}	calc_X _{H₂}	R_H ₂	α
25% D₂O trial 1	6.79078	4.52719	0.00470	0.12775	0.86754	0.07352	0.22089
25% D₂O trial 2	5.60047	3.73365	0.00672	0.15049	0.84280	0.08915	0.26783
25% D₂O trial 3	6.60053	4.40035	0.00496	0.13092	0.86412	0.07564	0.22725
average	6.33059	4.22040	0.00546	0.13639	0.85815	0.07944	0.23866
stdev	0.63942	0.42628	0.00110	0.01231	0.01341	0.00848	0.02547

51% D₂O trial 1	2.10538	4.38263	0.03683	0.31016	0.65301	0.23714	0.22784
51% D₂O trial 2	2.04449	4.25587	0.03861	0.31578	0.64561	0.24421	0.23463
51% D₂O trial 3	1.94212	4.04278	0.04192	0.32564	0.63244	0.25708	0.24700
51% D₂O trial 4	2.40080	4.99758	0.02971	0.28531	0.68498	0.20796	0.19981
51% D₂O trial 5	1.46677	3.05328	0.06463	0.37919	0.55618	0.34039	0.32704
average	1.99191	4.14643	0.04234	0.32322	0.63444	0.25736	0.24726
stdev	0.33951	0.70675	0.01324	0.03465	0.04783	0.04979	0.04784

73% D₂O trial 1	0.98700	5.28333	0.11306	0.44637	0.44057	0.50585	0.18927
73% D₂O trial 2	0.96533	5.16738	0.11643	0.44958	0.43399	0.51720	0.19352
73% D₂O trial 3	0.83962	4.49446	0.13931	0.46786	0.39283	0.59464	0.22250
average	0.93065	4.98172	0.12293	0.45460	0.42246	0.53923	0.20176
stdev	0.07957	0.42595	0.01428	0.01159	0.02587	0.04832	0.01808

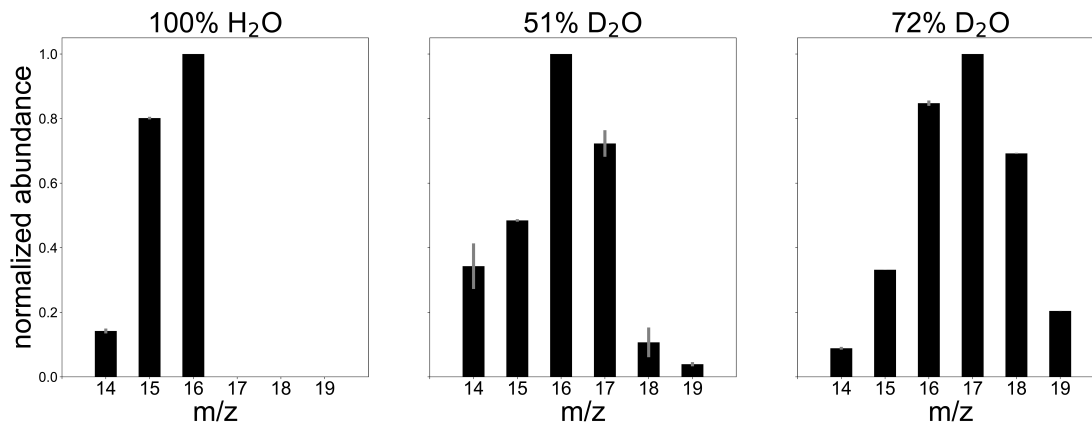
B.12 Mass Spectra of Methane Peak of Headspace of NaCN Reduction Assays

Figure B.14: Mass spectra of methane peaks of headspace of NaCN reduction assays in 100% H₂O, 51% D₂O, and 73% D₂O. Abundance normalized to peak of greatest abundance. Mass spectra generated by integrating under methane peak of extracted ion chromatograms of m/z = 14-20. Error bars (grey) are standard deviation from 2 trials. As mole fraction of D₂O in buffer increases, greater abundance seen at m/z = 17, m/z = 18, m/z = 19, and m/z = 20, corresponding to increase in CH₃D, CH₂D₂, CHD₃, and CD₄ in the headspace.

B.13 Possible Pathways for Formation of Methane Isotopologues from Cyanide by Nitrogenase

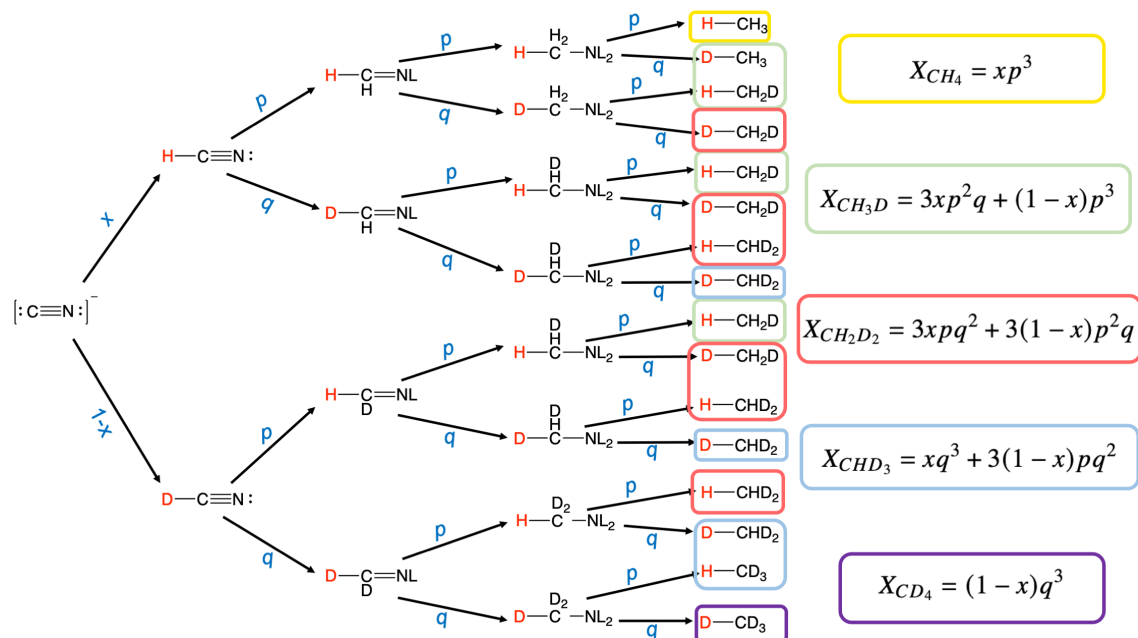


Figure B.15: Schematic of formation of methane isotopologues by nitrogenase in mixed H₂O/D₂O buffers. The probability that the substrate is HCN is given by x and $1 - x$ is the probability that the substrate is DCN. The probability that an H is added is p and the probability that a D is added is q . This schematic of all possible pathways toward methane formation led to the derivation of Equations 4.8-4.12 (shown on right). The probability that a H or D is added (p and q , respectively) as a function of the isotope effect and the mole fraction of H vs. D in the solvent is reported in Appendix Section B.9.

References

- (1) Yang, Z. Y.; Khadka, N.; Lukoyanov, D.; Hoffman, B. M.; Dean, D. R.; Seefeldt, L. C. *PNAS USA* **2013**, *110*, 16327–16332.
- (2) Lin-Vien, D.; Fateley, W. G.; Davis, L. C. *App. Environ. Microbiol.* **1989**, *55*, 354–359.
- (3) Han, J.; Newton, W. E. *Biochemistry* **2004**, *43*, 2947–2956.
- (4) Benton, P. M.; Christiansen, J.; Dean, D. R.; Seefeldt, L. C. *J. Am. Chem. Soc.* **2001**, *123*, 1822–1827.
- (5) Fisher, K.; Dilworth, M. J.; Kim, C. H.; Newton, W. E. *Biochemistry* **2000**, *39*, 10855–10865.
- (6) Viglaska, D.; Rey, M.; Delahaye, T.; Nikitin, A. V. *J. Quant. Spectrosc. Radiat. Transf.* **2019**, *230*, 142–154.
- (7) Spencer, R. W.; Daniels, L.; Fulton, G.; Orme-Johnson, W. H. *Biochemistry* **1980**, *19*, 3678–3683.
- (8) Khushvakov, J.; Nussbaum, R.; Cadoux, C.; Duan, J.; Stripp, S. T.; Milton, R. D. *Angew. Chem. Int. Ed.* **2021**, *60*, 10001–10006.
- (9) Luxem, K. E.; Leavitt, W. D.; Zhang, X. *Appl. Environ. Microbiol.* **2020**, *86*, 00849–20.
- (10) Yang, H.; Gandhi, H.; Cornish, A. J.; Moran, J. J.; Kreuzer, H. W.; Ostrom, N. E.; Hegg, E. L. *Rapid Communications in Mass Spectrometry* **2016**, *30*, 285–292.
- (11) Löffler, M.; Kümmel, S.; Vogt, C.; Richnow, H. H. *Front. Microbiol.* **2019**, *10*.
- (12) Yang, H.; Gandhi, H.; Shi, L.; Kreuzer, H. W.; Ostrom, N. E.; Hegg, E. L. *Rapid Commun. Mass Spectrom.* **2012**, *26*, 61–68.
- (13) Zhang, X.; McRose, D. L.; Darnajoux, R.; Bellenger, J. P.; Morel, F. M.; Kraepiel, A. M. *Biogeochemistry* **2016**, *127*, 189–198.
- (14) Luo, Y.-H.; Sternberg, L.; Suda, S.; Kumazawa, S.; Mitsui, A. *Plant Cell Physiol.* **1991**, *32*, 897–900.